UNIVERSITÀ DEGLI STUDI DI PARMA

IISER THIRUVANANTHAPURAM

DOTTORATO DI RICERCA IN

SCIENZE CHIMICHE

Metal-Organic Frameworks as Remedy for Water Pollution – Sensing and Removal

Coordinatore:
Prof. Alessia Bacchi

PhD student:
Dott. Asha Pankajakshan

Tutore:
Prof. Federica Bianchi
Co-Tutore:
Prof. Paolo Pelagatti
Dr. Sukhendu Mandal

Anni 2017/2020

Dedicated to my parents, soul mate and to my baby

പറക്കാൻ ചിറകു തന്നവർക്കും, കൂടെ പറക്കുന്ന കൂട്ടുകാരനും.....

Preface

Metal-Organic Frameworks (MOFs) consists of metal ions or metal clusters linked with organic ligands by coordination bonds. MOFs possess various properties like high surface area, tunable porosity, excellent thermal and mechanical stability. Therefore, these materials have countless applications in fields like catalysis, sensing, adsorption, etc.

In this thesis, the use of several MOFs for water sensing and adsorptive removal of toxic chemicals from water is explored. In the first chapter, the synthesis, properties, and applications of MOFs were discussed. The second chapter illustrates the application of a zinc MOF with nitrogen binding sites for the sensitive and selective sensing of mercury ions was explained. In the third chapter, we have shown that the fragment of benzene tricarboxylic acid in a Ba-based MOF was replaced by boronic isophthalic acid *in situ* to obtain a series of MOFs. The modified MOFs were used for cis-diol adsorption in an aqueous medium. In the fourth chapter, the usage of a zinc MOF as solid-phase microextraction (SPME) coating for the extraction of polycyclic aromatic compounds (PAHs) is explained. The fifth chapter illuminates the thiol functionalised zirconium MOF template for the synthesis of palladium nanoparticles in the narrow size range and its use as a catalyst for hexavalent chromium reduction in an aqueous medium.

Chapter 1: In this chapter, a brief introduction to metal-organic frameworks (MOFs), their properties and the possible applications in various fields of research were given.

In the following four chapters, the use of water-stable MOFs for the remediation of some critical chemical pollutants is discussed.

Chapter 2: In chapter 2, a water-stable MOF was synthesised and used for the sensing of Hg (II) ions in water. The MOF exhibits good quenching constant (1.011×10^9 M^{-1}) and shows selective sensing of the order of picomolar concentration in the aqueous medium. The MOF dispersion has no interference from similar mono- and di-valent metal ions and hence could be considered as very selective towards mercury. The Hg (II) ions interacts with the -N = N- group belonging to one of the ligands leads to the quenching of fluorescence. Water samples from natural sources are also used for the analysis and the Zn-MOF shown promising results. Finally, the MOF crystals could be grown over an aluminium thin film to use it as a solid-state sensor.

Chapter 3: In this chapter, a family of boronic acid suspended MOFs with comparable structures with a parent Ba-MOF structure was constructed by an MLFC (metal-ligand-fragment coassembly) approach. The boronic acid groups in the MOF scaffold were utilised for the binding of cis-diols from aqueous solutions keeping in mind the affinity of the cis-diols for boronic acid moieties. The presence of boronic acid groups in the MOFs were analysed quantitatively by the experiments of XPS and ^{11}B NMR. The direct relation of percentage incorporation to the feed is investigated. The cis-diol binding experiments were carried out using the parent Ba-MOF and the boronic acid analogues and the results are compared and quantified. (1:1)-B MOF with the highest amount of boronic acid moiety shows better adsorption results. The cis-diol adsorption was in the order galactose > glucose > mannose > xylose. The trend in cis-diol binding fundamentally based on the amount of furanose isomer of cis-diol in the aqueous medium. The pseudo-second-order kinetics explains the adsorption better, and it follows Langmuir adsorption isotherm.

Chapter 4: In this chapter, a zinc-based MOF (PUM-210, where PUM stands for Parma University Materials) is used as a coating for SPME (solid-phase microextraction). The MOF coated fiber was analysed for its extraction capability towards the 16 polycyclic aromatic hydrocarbons (PAHs). The mixed-ligand MOF PUM-210 is found to be a promising candidate as the coating for SPME. The MOF has high porosity, good thermal stability, and excellent selectivity towards PAHs. The extraction ability depends on a number of factors like hydrophobicity of PAHs, π-π interactions between the ligands and the PAHs and so on. The optimisation method using various desirability functions is followed for the simultaneous determination of the PAHs at nanogram levels. The efficiency of adsorption with the MOF coated fiber was reproducible and each fiber could be used for over 200 analyses without any changes in extraction capability.

Chapter 5: In this chapter, a stable zirconium MOF (UiO-66-SH-10) is designed and synthesised by following an MLFC method using terephthalic acid and the modulator 2-mercaptobenzoic acid. The thiol-functionalised modulator not only helps in creating various defect sites in the framework but also introduces the free thiol functionality throughout the scaffold. Thiol groups act as a guide and support for the palladium embedment and subsequent reduction to nanoparticles. Palladium nanoparticles are formed with uniform shape and size. The Pd@UiO-66-SH-10 was utilised for the

hexavalent chromium reduction with high efficiency and recyclability in the water medium.

Summary

Chapter 1

Introduction to Metal-Organic Frameworks (MOFs)

Abstract

Metal-Organic-Frameworks or MOFs are a novel class of inorganic-organic hybrid materials made up of metal ions or metal clusters linked by various organic linkers. This chapter deals with the synthesis, properties, and applications of MOFs in diverse fields. MOFs possess high surface area, tunable porosity, high thermal and mechanical stability. They found applications in numerous sectors like as coating materials, for drug delivery, gas separation, storage, sensing, and catalysis. The sources of environmental pollution in general and water contamination, in particular, is addressed by explaining the possible pollutants. The different steps in ensuring the purity of water are sensing and monitoring the concentration of a toxin and their removal when present in an alarming amount. MOFs are widely used in various steps, during the decontamination of water.

1.1 General Introduction

Metal-Organic Frameworks or MOFs are inorganic-organic hybrid materials made up of metal ions or metal clusters and organic linkers. According to IUPAC recommendations 2013, MOFs are coordination networks with organic ligands containing potential voids.[1] The field of MOFs emerged as an area of research during the 1990s and flourished in ways of property studies and diversity of applications. These crystalline materials are well known for their vast surface area (up to ~7000 m^2/g) and peculiar porosity. The surface area, along with the extraordinary variability of the structural components and the aesthetic beauty of the architectures place MOFs at the epitome of material chemistry.[2] MOFs find applications in multiple fields such as purification of water,[3] sensing of toxic chemicals,[4] adsorptive removal of contaminants[5] and even in the delivery of drugs into specific active sites.[6] There are a handful of methods for the MOF synthesis, namely solvothermal - which is the most widely used strategy, hydrothermal, mechanical, sonochemical and microwave synthesis.[7] The inability to predict and control the results is considered as one of the drawbacks of the conventional way of synthesis of MOFs.[8] In this scenario, the post-synthetic modification (PSM) of the frameworks opened an innovative pathway to obtain desirable scaffolds.[9]

1.1.1 Structure

Asymmetric units are the cells of the MOF scaffold, which repeated in 2 or 3 dimensions to create the polymeric structure. In contrast, secondary building units (SBUs) are molecular complexes or cluster entities when connected with the polytopic ligands extended into porous networks.[10] It is remarkable to note that of all the MOFs reported and deposited in the Cambridge Structural Database so far; the majority is made up of carboxylic acid-based struts.[11]

A brief list of some common SBUs used to build MOF structures is shown in figure 1.1. The first reported MOF with a permanent porosity is MOF-5 made up of the metallic Zn_4O SBU connected with the terephthalic acid linker.[12] By changing the length and functionality of the dicarboxylic linker, several isoreticular (IR) MOFs with similar SBU are obtained. Usage of long linkers does not always lead to enhanced porosity; it is determined by the interpenetration as well. When a cavity is sufficiently large enough, the growth of an interpenetrated framework is favoured. The interpenetration is constructive from an energetic point of view. It also stabilizes the system.[13] The extent of interpenetration is determined by several factors like the type of solvent, reaction temperature and the use of templates.[14–16]

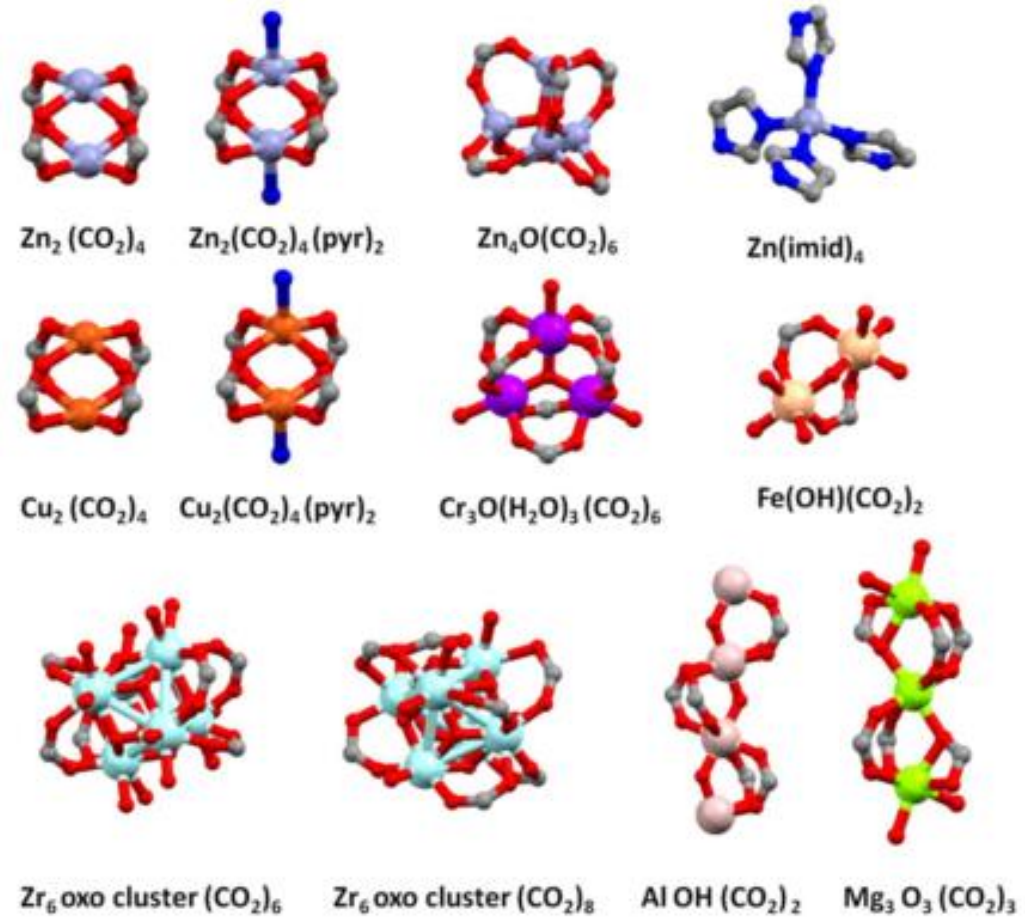

Figure 1.1. *Common SBUs in MOFs.*

Another useful method to control the structure of the product formed is post-synthetic modification (PSM). As the name itself indicates, it is the modification of the structure after the synthesis of a MOF. In this way, new functionality and metal centres could be introduced into the as-synthesized MOF scaffold.[17] The absolute magic of this technique lies in the fact that the developed frameworks are mostly unattainable through de-novo synthesis.[18]

1.1.2 Properties

Being a material with inorganic and organic counterparts, MOFs possess several properties that make them unique among functional materials like metal complexes, metal nanoclusters, and metal nanoparticles. MOFs have a high surface area, pore-volume, excellent mechanical, thermal and moisture stability. Moreover, the tunable pore size and the possibility of PSM makes these materials suitable candidates for applications in various fields.

1.1.2.1 Luminescence

The opportunity to use different metal ions right from alkali metals to lanthanides and a variety of organic linkers from carboxylic acids to azides, the resulting scaffolds of MOFs can show interesting luminescence properties. The excitation of the MOF followed by emission of photons leads to the luminescence process. When the emission takes place from the lowest singlet excited state (S_1) to the ground state (S_0), the process is termed as fluorescence which has a lifetime of 1-100 nanoseconds. Whereas, when the excited molecule undergoes intersystem crossing from the singlet to the triplet state and emits from the lowest triplet excited state (T_1) to S_0, it is said to be phosphorescence (with a lifetime $\geq 1\mu s$) (Fig. 1.2). Since MOFs are complex systems with several possible components like metal ions, ligands, guest molecules, and solvent molecules, they exhibit many photoluminescence processes. Some of the mechanisms are ligand-to-ligand charge transfer (LLCT), ligand-to-metal charge transfer (LMCT), metal-to-ligand charge transfer (MLCT), and

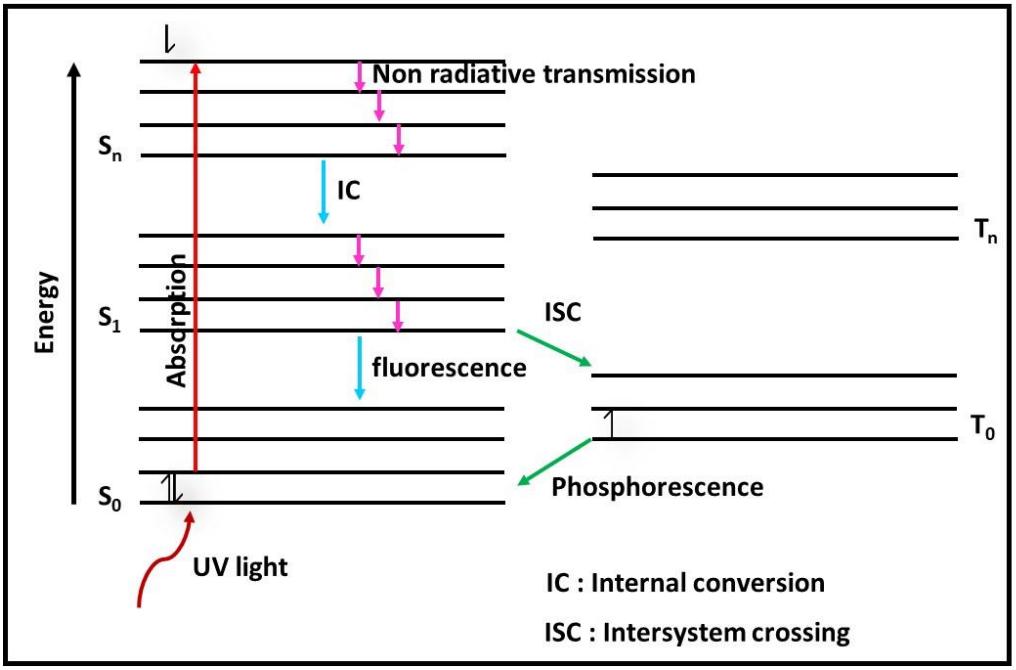

Figure 1.2. *Schematic representation of a Jablonski diagram illustrating the electronic states of a molecule and the corresponding transitions between these states.*

metal-to-metal charge transfer (MMCT), as well as processes that involve guest molecules in the MOF pores, such as guest-centered emission, guest-sensitization, excimer, and exciplex formation.[19] Reports on MOFs based luminescence are extensive. Recently Z. Liu *et al.* have reported about the green luminescence of a terbium MOF which is induced by the efficient antenna effect of the ligands present in it. [20]

1.1.2.2 Surface area and pore volume

MOFs are in the frontiers of research mainly due to their high internal surface area and tunable pore size, which is utilized in several applications like catalysis, energy storage systems, and drug delivery. The most straightforward strategy to obtain high surface area MOFs is to use elongated ligands in a robust topology. Usually, the removal of guest molecules and solvents by the activation methods leads to the increased available surface area. Another technique is to reduce the dimension of the MOFs from micro to nanoscale. This considerably improves the surface area of

the resultant framework.[21] The world record holder among MOFs for the largest pore volume and highest surface area is held by DU-60 synthesized by S. Kaskel *et al*.[22] It possesses a pore volume and surface area of 5.02 cm^3/g and 7839 m^2/g, respectively surpassing NU-110 by the research group of J. T. Hupp.[23]

1.1.2.3 Stability

Framework stability or robustness is one of the factors which determine the usefulness of MOF as a functional material. The factors affecting the stability are the nature of metal ions and linkers, synthetic conditions, hydrophobicity of the pore surface, the strength of the coordination bonds in the scaffold, etc. Pearson's HSAB principle helps in predicting the stability of the resultant MOFs. Hard bases like carboxylic acids bind strongly with the hard acid metal ions Ti^{4+}, $Zr^{4+,}$ and Al^{3+}. The Zeolitic Imidazolate Frameworks (ZIFs) formed by the Zn^{2+} ions and imidazole linkers is the perfect example to study the importance of the principle.[24] The overall stability increases with the connectivity of the metal nodes and ligands, the robustness of the linkers and the presence of hydrophobic groups in the scaffold.[25] UiO-66 being the first of the series of zirconium MOFs, are well known to be stable towards moisture even in the acidic conditions.[26]

1.1.2.4 Conductivity

The electrical conductivity of MOFs is a hot topic of study since it has the advantages of both the inorganic and organic counterparts. Conductive MOFs find applications in a multitude of fields like solar cells, gas sensors, and bipolar transparent conductors. Several mechanisms, like the overlap between ligand π* and metal d-π orbitals, metal to metal direct electron transfer and the π-π orbital overlap in the framework, give rise to electrical conductivity in MOFs.[27] The addition of conducting guest molecules is yet another method for the same. 7,7,8,8-tetracyanoquinodimethane (TCNQ), tetracyanoethylene (TCNE), N, N' -dicyanoquinonediimine (DCNQI) are some of the examples of the guest molecules that could be suspended in the framework to improve the conductivity.

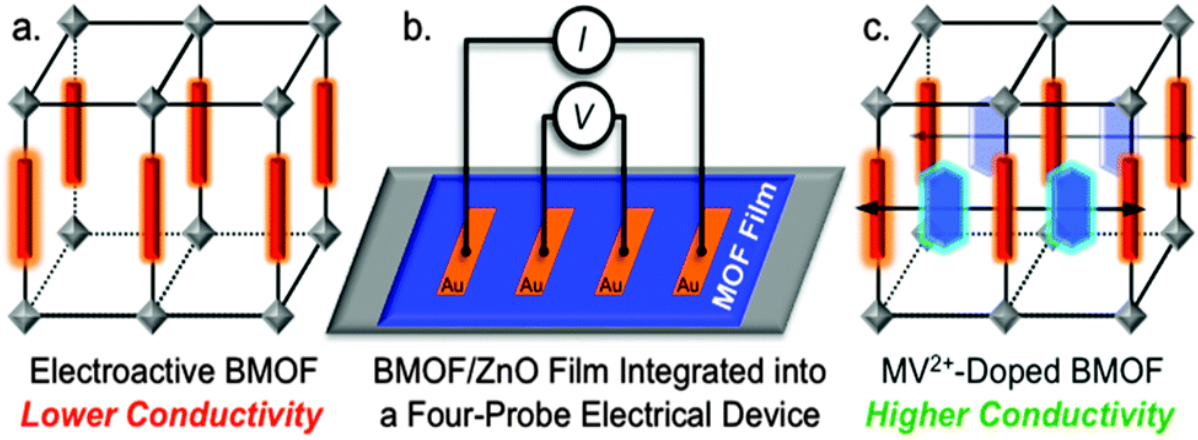

Figure 1.3. *graphical representations showing (a) an electroactive MOF with redox-active ligands, (b) a four-probe electrical device composed of the ZnO-coated surface with electroactive MOF film grown selectively over it, and (c) π-acidic guests intercalated between the redox-active ligands showing a better electron delocalization through the resulting π-D/A stacks and higher conductivity. Reproduced from ref. 19, Copyright 2016 Royal Society of Chemistry.*

S. Saha et al. investigated and proved by incorporating guest π-systems that can promote long-range electron delocalization by forming extended π-stacks with the redox-active ligands, the conductivity of MOFs could be fine-tuned (Fig.1.3). [28]

1.1.2.5 Magnetism

Magnetic MOFs are gaining increased attention due to the possibility of using a wide variety of metals for their formation and the ability to exhibit different ways of magnetism. Using small linkers for avoiding the porosity and thereby increasing the chance of metal super exchange by reducing the distance between them is a way of incorporating magnetism in the MOFs with suitable metal ions. Yet another scheme with a mixture of short and long ligands may form a magnetic MOF with a strong magnetic interaction between metal centers in one or two dimensions with low-temperature ordering. Spin-crossover phenomena in some metal ions also give rise to magnetism, in which there is no restriction about the length of the linkers or porosity. All it requires is a suitable ligand environment for the metal ions to

change between high-spin (HS) and low-spin (LS) under external stimuli like temperature, magnetic field, electric field, etc.[29]

1.1.3 Applications

MOFs with superior properties find applications in various areas of life such as decontamination of environment, sensing of toxic analytes, catalysis, the formation of conductive and magnetic materials, nanomotors for drug delivery, as templates for nanoparticle synthesis, etc. The easiness of preparation, low cost of synthesis and stability make them the favourite among several other competitors like zeolites and coordination complexes. Few of the most common applications are discussed below:

1.1.3.1 Adsorption

MOFs provide unique systems with stability, extraordinary surface area and pore volume, adjustable pore sizes, and tunable framework–adsorbate interaction by ligand functionalization and choice of metal.[30]The tunability of the pores is the highlight in this regard which aids to synthesize MOFs with desirable functional groups that have an affinity towards several analytes. The interaction between the adsorbents and adsorbates vary from simple hydrogen bonding to chemical bonding. The use of metal-organic framework nanocomposites for the selective capture and release of glycoproteins is reported by Z. Gu and co-workers. The boronic acid groups in the MOF form cyclic esters with the hydroxyl groups of glycoproteins at pH 7, which get dissociates at a slightly higher pH of 9.[31] Even gases could be adsorbed for storage and transportation with suitable MOFs. The significance of the aromatic ligands in the scaffold to bind the H_2 molecule is explained by the research team of M. Schröder.[32] The open metal sites and micropores are other factors which affect the gas uptake capacity of a MOF.[30]

Pollutants that are very much diluted could be concentrated to a detectable level by adsorbing to a suitable adsorbent and examined with various analyzing techniques such as gas-chromatography mass spectrometry (GC-MS). Solid-phase microextraction (SPME) is a sample preparation technique that uses appropriate adsorbent materials coated on the SPME fiber for the collection of samples in minute quantities.[33] The significant advantage of SPME is the handiness which helps in the collection of samples even from very remote sources like polar glaciers (Fig.1.4). Among the coating materials for SPME like polydimethylsiloxane (PDMS), divinylbenzene (DVB) and carboxen, MOFs are an apt choice.[34],[35]

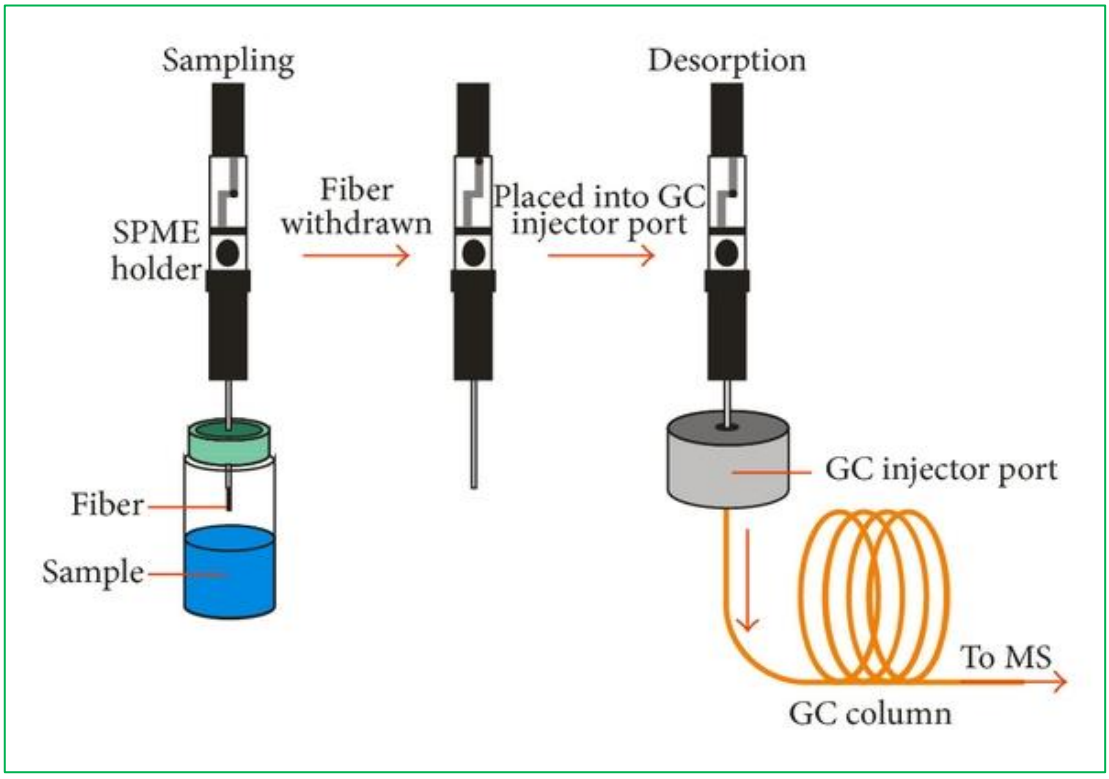

Figure 1.4. *The graphical representation is showing the working of SPME equipment. Reprinted with permission from ref.*[36]*. Copyright 2018 Wiley.*

1.1.3.2 Sensing

Sensing the presence of a contaminant is the primary step for its removal. Sensing also helps in keeping the concentrations of various analytes in the system of interest like atmosphere, water sources and even in the human and animal body at the permissible level. Accurate monitoring helps in keeping the amount of analytes within the allowed limit, thereby to avoid the possible consequences. Luminescence is so far the best property to be monitored for the sensing studies involving MOF species. It can either be a "turn-on" or "turn-off" strategy, where the earlier one is considered advantageous over the other. In the "turn-on" mechanism, the response can be triggered by restricting the non-radiative relaxations in MOFs either by a) incorporation of rigid functional groups, or b) by exciplex/excimer formation with the incoming guest molecules.[4]

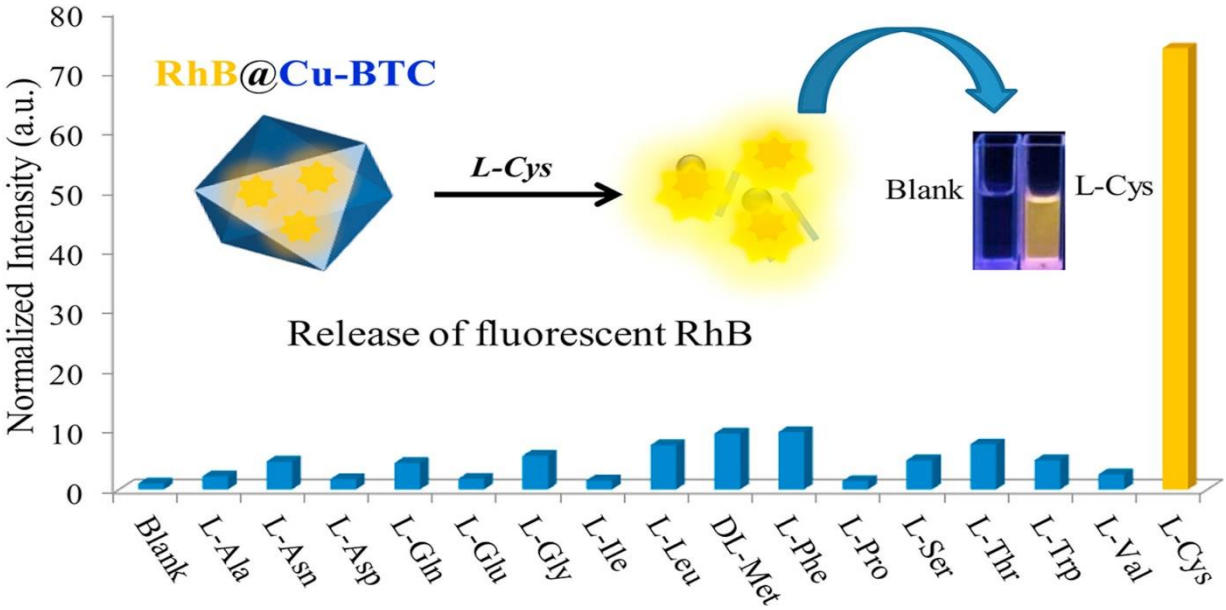

Figure 1.5. *The rhodamine B (RhB) incorporated MOF RhB@Cu-BTC acts as a 'turn-on' sensor for the amino acid L-Cysteine (L-Cys). In the presence of the thiol group of L-Cys, RhB is released from the MOF giving the fluorescence. Reprinted with permission from ref.*[37] *Copyright 2018 Elsevier.*

Turn-off or quenching is caused mainly due to the competitive absorption by the analytes of interest. There are some MOFs used as electrochemical sensing surface modifiers because of their high surface area and pore volume, good absorbability, and high catalytic activity.[38] Because of the low electrical conductivity and micron size, there is a limited number of MOF examples. The key to achieving efficient electrochemical signals is to prepare MOFs with high redox activity and electrical conductivity while preserving their unique pore structure.[39]

1.1.3.3 Catalysis

A catalyst is a substance that speeds up a particular reaction by reducing the activation energy of the process and also without being consumed in the process. MOFs with their high surface area and tunable pore structure is the right candidate as a catalyst for various chemical processes. Since MOFs are stable solids, they usually act as a heterogeneous (surface) catalyst where adsorption plays a prominent role. The metal ions or clusters are the main catalytic centers in the MOF scaffolds. In a report by J. Ye *et al.*, an amine-functionalized iron-based MOF is used as a photocatalyst for the reduction of hexavalent chromium ion (Cr (VI)) to Cr (III). The direct excitation of Fe_3-μ_3-oxo clusters along with the excitation and transfer of an electron by the amine functionality is the catalytic mechanism for the reduction.[40] Y-Z. Zheng *et al.* explained the importance of redox-active metal centers in MOFs for oxidation reactions with a mixed valent cobalt MOF for the selective oxidation of cyclohexene on the allylic position without affecting the adjacent double bond.[41]

1.1.3.4 Drug delivery

The transport of a specific drug to a particular site and release without affecting the surrounding area is vital in the clinical and biomedical areas of research. Various novel materials like nanomotors are studied for this function among which MOFs have their advantages because of the freedom of selecting the biocompatible metals and ligands for their synthesis, tunable pore structure, and high surface area. Biologically important gases like

nitrous oxide (NO) could be stored and released with ease in response to the moisture.[42] Most MOFs follow the approach of degradation of the framework and release of the loaded drugs at a specific site. The major drawback of this is the need for a suitable MOF with non-toxic metal, linker and pore volume. Hence another approach is developed, which uses linkers having drug activity to build the MOF. In this way, the problem with porosity and linker toxicity could overcome with suitably selecting the metal ion.[43]

1.1.3.5 Supercapacitance

Due to the depletion in fossil fuels and increased concern about the current rate of emission of pollutants, the scientific community all over the world is in search of efficient materials for energy storage/conversion. Supercapacitors as suitable energy storage materials for portable electronic devices has advantages like high recyclability, power output, and long cycling ability.[44] Several MOFs are developed as well-performing electrodes for improving the energy density of the supercapacitors. For example, Y. Yao *et al*. synthesized a self-supported hierarchical Co-MOF as a positive electrode for supercapacitor with ultrahigh areal capacitance and excellent rate performance.[45]

1.1.3.6 Miscellaneous applications

MOFs have plenty of other applications in various fields of life. These materials can act as templates for the synthesis of functional materials like nanoparticles, nanoclusters and quantum dote.[46,47] The formation of the desired product, followed by the destruction of the MOF framework, usually by combustion releases the functional material for the targeted use. Another use of MOFs is as composites with other active materials. The use of the nylon-MOF composite for the degradation of the chemical warfare agent simulant shows the significance of this class of materials.[48]

1.2 Environmental pollution

Contamination of the physical and biological components of the atmosphere adversely affect the ecosystem. Natural processes such as volcano eruption, forest fires along with man-made activities such as excessive use of fossil fuels, pesticides, and stubble burning also contribute towards the pollution of air, water, and soil. These contaminants reach the ultimate consumer-man in a way or another. Therefore, it is necessary to know the various sources of pollution and search for remedies.

1.2.1 Water pollution

Water-the elixir of life is polluted like never before. Any pollutants from air or soil find its final journey towards the water sources due to rain. The common water sources like wells, ponds, rivers, oceans along with groundwater sources are getting impure day by day. The major contributors are industrial effluents like heavy metal ions, agricultural chemicals like pesticides and insecticides, and various atmospheric particulates washed out with rain.

1.2.1.1 Heavy metal ions

The most common heavy metal contaminants are chromium, cadmium, arsenic, mercury, nickel, and lead. The accumulation of these metals in the human body interrupts the enzyme function and even lead to gene mutation. The primary sources are mining areas and industries dealing with these chemicals. Sensing and monitoring the normal levels of these metals and the removal of the same at the alarming state requires novel efficient sensors and adsorbents.

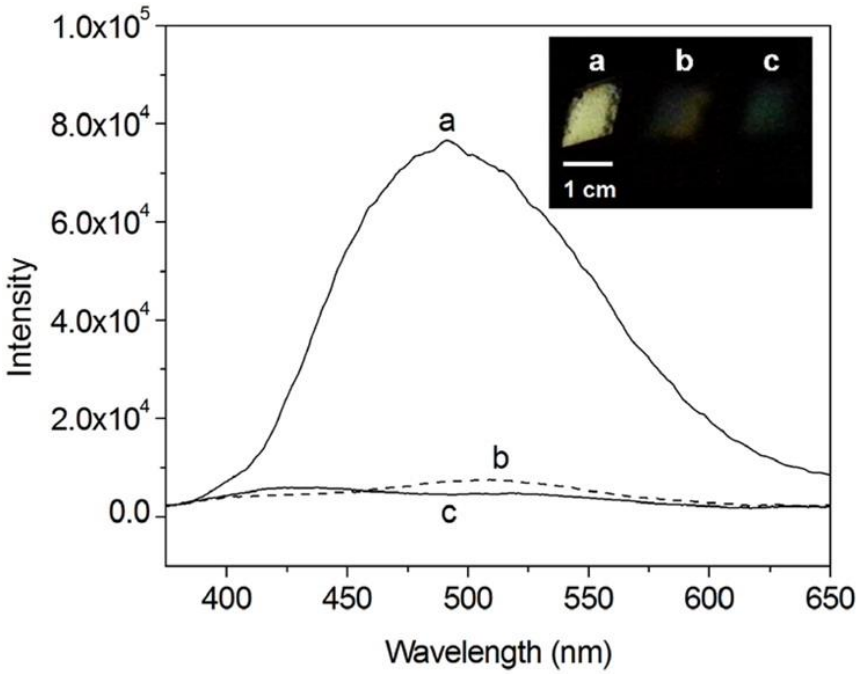

Figure 1.6. *Room-temperature solid-state emission spectra (λ_{ex} = 355 nm) of the MOF (Zr-DMBD) samples: (a) as-made sample; (b) after exposed to an aqueous solution of $HgCl_2$; (c) after treatment with the vapor of Hg(0). The inset shows the samples a−c under 365 nm UV radiation. Reprinted with permission from ref.40. Copyright 2013 American Chemical Society.*

Numerous MOF sensors and adsorbents are reported in the literature for the detection and removal of these metals (Fig. 1.6).[20,49,50] M. J. Manos and co-workers developed an 8-connected zirconium MOF for the adsorptive removal of Cr(VI) ions.[51] Likewise, the electrochemical detection of heavy metal ions by the glass electrode modified using lanthanide MOF is reported recently by Q. Guodong *et. al.*[52]

1.2.1.2 Insecticides and pesticides

Agricultural runoff is another primary source of pollution. It contaminates the air, soil and ultimately all water sources leading to a phenomenon called eutrophication. Organophosphate compounds are the villain in this, which triggers the sudden algal bloom in the water body

followed by the consumption of most of the dissolved oxygen in the water, leading to the death of fishes. Once it enters the human body interrupts the functioning of neurotransmitter acetylcholinesterase, leading to paralysis and even death. Zirconium MOFs are at the forefront for the removal or degradation of the organophosphate compounds. J. Wang and co-workers developed a smart material (Fe_3O_4@SiO_2@UiO-67) which simultaneously detects and removes the organophosphorus pesticide glyphosate. [53]

1.2.1.3 Chemical warfare agents (CWAs)

CWAs, as the name indicates, are toxic chemicals used during wartime which causes several casualties within no time. According to the mode of the effect, they are classified as blistering agents, choking agents, blood agents, and toxins.[54] Removal/degradation of the same from the environment is essential because of the health effects it poses. Like in the previous section, zirconium MOFs are suitable materials for CWA removal as well. As the laboratory use of CWAs is restricted due to their extreme toxicity, CWA simulants- the model compounds that resemble the structure of CWAs but with less toxicity- are used in most of the researches.[55] In recent work, UiO-66 was used for the solvent assisted degradation of dimethyl 4-nitrophenyl phosphate (DMNP), which is a simulant of the chemical warfare agent (CWA) sarin (GB).[56]

1.2.1.4 Nitroaromatics

Nitroaromatics is an essential class of chemicals that are released to the environment only by human activities. Nitroaromatic compounds are listed on the U.S. Environmental Protection Agency's list of priority pollutants for environmental remediation and are a threat to human health. They are widely used in the synthesis of dyes, polymers, explosives, and their excessive release causes soil and groundwater pollution.[57] Among several methods for remediation, adsorption is found to be the best which is reported by a wide variety of

materials like graphene, clay, and zeolites. The study by H. -C Zhou *et al.* addresses the selective detection and removal of the nitroaromatics using two Zr MOFs. [58] Likewise, a rare lithium MOF is used for the detection of nitroaromatics by a colour change and luminescence quenching.[59]

1.3 Objectives of the thesis

In this quickly growing world, our environment, including the earth, water, and air, are contaminated to such an extent that life of all is under threat. Even space is not free from pollution. Human activities are the major contributor to this situation. Hence, we have the responsibility to control the sources of pollution, monitor and reduce the effects of the present trash. The prime objective of the thesis is the remediation of pollutants, especially from the water sources. As the freshwater sources are limited and diminishing day by day, as droughts hitting several countries, keeping the water bodies safe and secure is essential. Identifying the presence and supervising the contaminant level and their removal is the three significant steps to be followed in the water decontamination. Innumerable novel materials are designed, built and utilized for this purpose and drawbacks of a material call for the need of a superior one. MOFs are always the scientist's favourite because of its structural uniqueness, ease of synthesis and the exceptional properties. MOFs are used in both the sensing and removal of contaminants in water. Luminescence is the property exploited the most for the sensing purpose, due to the inherent luminescence property exhibited by most of the MOFs. Adsorption plays a prominent role in the removal of pollutants due to the high surface area, tunable pore structure and the presence of some free functional groups.

In the five chapters followed, water-stable MOFs have been used for the remediation of some chemical pollutants. The second chapter consists of two parts, part A deals with the adsorptive removal of chemical warfare agents, and part B is that of the herbicide glyphosate.

Zirconium MOFs-NU-1000 and UiO-67 have been used for both studies. The third chapter includes the selective and sensitive detection of the heavy metal mercury by a novel zinc MOF. The work has been extended to study real water samples collected from stream, river, and sea. The fourth chapter comprises of the sample collection of 16 nitroaromatics from the area of study using an SPME (solid-phase microextraction) fiber coated with a zinc MOF and the subsequent release study monitored by GC-MS.

The adsorptive removal of cis-diols by the boronic acid decorated MOFs is the highlight of the fifth chapter. A new method of metal-ligand-fragment coassembly (MLFC) is introduced here. MLFC is a method of using a ligand and its fragment for the synthesis of a MOF to create coordinative unsaturation on the metal ion or metal cluster. These open, active sites act as defects which enhances the surface area of the MOF and helps in the applications like adsorption. The sixth and final chapter consists of the development of a defective zirconium MOF by using the MLFC method followed by the incorporation of palladium nanoparticles (Nps). The palladium nanoparticles act as an excellent catalyst for the use of hexavalent chromium reduction. MOF acts as a template where the thiol groups in the modulator help the palladium nanoparticles to attach to the framework firmly. Therefore, the stability of the Nps against the possible aggregation and removal is enhanced. All the chapters deal with the exploitation of MOFs for the sensing, or removal of toxic chemicals from water.

Chapter 2

Ultrasensitive Detection of Hg (II) Ions in Aqueous Medium Using a Zn-based MOF

Abstract

The toxic mercury ions are expelled to the water sources by many industries. According to the united states environmental protection agency (US EPA), 10 nM is the highest permissible level of mercury ion in drinking water. Therefore, sensing and monitoring its concentration in water is essential. We have developed a Zn-based water-stable sensor for the selective sensing of Hg (II) ions. The aqueous dispersion of the MOF exhibit quenching of fluorescence with the addition of Hg(II) ions. The promising selectivity and sensitivity are due to the specific pore size, suitable interaction site and water stability of the structure. On binding the Hg (II) ion into the ligand-based –N = N- groups in the pores, the electronic structure of the compound changes, which affects the fluorescence intensity. The specific size of the rectangular pores in the structure is suitable for larger Hg (II) to interact selectively.

2.1 Introduction

Mercury is a primary contaminant of the environment which is expelled from various industries.[60]The mercury in its ionic form is changed to the neurotoxic methylmercury by bacterial action. The vital human body organs are prone to mercury poisoning even at a very low quantity.[61]According to the US EPA (United States Environmental Protection Agency) the highest permissible amount of Hg (II) in drinking water is standardized to be 10 nM.Considering the deadly poisonous nature and its sources, the concentration of Hg(II) ions has to be strictly monitored. The various methods available for its tracking are chromatography,[62] spectrofluorimetry[63]and atomic absorption spectroscopy[64]. The expensive and time-consuming nature made the use of these sophisticated methods limited. Researchers are in continuous search for cost effective and easy ways of sensing and removing Hg(II) from the water bodies.[65],[66] The importance of fluorescence based techniques are their simplicity and cost effectiveness.[67],[68]Luminescent metal-organic frameworks (MOFs) are promising candidates due to their extraordinary stability, commendable surface area and easy availability.[69] The nature of MOF primaryly depends on the constituents like metal ions, ligands and guest molecules and the various interactions present between them.[70] By the strategic selection of the building blocks the luminescence nature of the MOFs could be fine tuned.[71] Various MOF scaffolds are known for their ability to selectively detect guest species like solvent molecules,[72] pharmaceuticals,[73] anions,[74]and cations.[75] On the other hand, compared to the number of reports based on the self-assembled materials (SAMs),[76] nanoparticles (NPs)[77] and dye bound optical sensors, the MOF based Hg(II) sensors are relatively few.[78]

The poor dispersion capability of several MOFs in the aqueous medium is a hindrance in the study of luminescent MOFs for the Hg(II) sensing. Moreover poor water stability and possible interference of other mono- and di valent metal ions are some other difficulties.

Also, most luminescent MOFs do not have an acceptable lower detection limit preferably less than 10 nM, which is the maximum permissible level of Hg (II) ion in drinking water (US EPA).

The higher binding ability of Hg(II) to the N atoms and the larger ionic radius compared to are the factors we have exploited for our work. Keeping this idea in mind, we have constructed a water-stable Zn-based MOF with freestanding azo (- N = N-) groups which shows a selective and sensitive affinity towards Hg(II) ions in the aqueous medium even in the presence of other interfering metal ions.

2.2 Results and Discussion

A Zn-based coordination polymer {[Zn(4,4'-AP)(5-AIA)] DMF}$_n$, (1) [4,4' AP = 4,4'-azopyridine, 5-AIA = 5-amino isophthalic acid and DMF = N, N'-dimethyl formamide] is synthesized for the selective and sensitive analysis of the poisonous Hg(II) ions in the aqueous medium. The Hg(II) ion with soft acidic nature interacts well with the nitrogen moieties which are soft bases; so, by incorporating nitrogen-containing ligands like 4,4'-AP and 5-AIA, the MOF scaffold could be made as a selective trap for mercury ions.[79],[80] The Zn-MOF is highly water stability and can selectively attract mercury ions in the picomolar (femtogram) limit even in the presence of mono and divalent interfering metal ions. According to our knowledge, the Zn-MOF serves as a rare example for the sensing of Hg (II) ions in the aqueous medium up to picomolar (femtogram) limit with excellent binding constant (Table 2.1).

Table 2.1. *A comparative chart of the limit of detection of different sensors for* Hg^{2+}

Sl. No.	***Type of sensor***	***Detection limit (M)***		K_{SV} (M^{-1})	***References***
1	Zn-based MOF(Compound 1)	9.9×10^{-12}		1.011×10^{9}	This work
2	Coumarin based probe	0.12×10^{-6}		NA	[65]
3	Gold nanorods embedded in a functionalized silicate sol-gel matrix	0.317×10^{-6}		NA	[68]
4	SAMs(Self-assembled materials)	1×10^{-12}		4.3×10^{6}	[76]
5	Bodipy capped Au NP	5.7×10^{-8}		NA	[77]
6	UiO-66@Butyne	10.9×10^{-9}		NA	[81]
7	Bis-pyridobenzene	1×10^{-6}		NA	[82]
8	Zn-based MOF	1.8×10^{-6}		3737 in water	[79]
		6.9×10^{-6}		63618 in acetonitrile	
6	Porphyrinic MOFs	6×10^{-9}		6.4×10^{5}	[83]
7	Zn-based MOF	Hg^{2+}	6.16×10^{-8}	NA	[84]
		MeHgI	1.75×10^{-7}		
8	Cd-based MOF	2×10^{-9}		4.3×10^{3}	[85]
9	Zn and Cd based MOFs	4.2×10^{-8}		4550	[80]
10	Nanofibrous membrane with Au nanoclusters	NA		NA	[86]
11	Rhodamine-based optical sensor	NA		3.71×10^{6}	[87]
12	Mixed polymeric micelles	4×10^{-8}		NA	[88]
13	Conjugated Polymers and Label-Free Oligonucleotides	4.2×10^{-8}		NA	[89]

The compound **1**(Zn-MOF) crystallizes in the $P2_1/c$ space group (SXRD, single-crystal X-ray diffraction) (Tables 2.2 & 2.3). The Zn ion has a distorted tetrahedral geometry binding to oxygen atoms of 5-AIP and nitrogen atoms of AP and 5-AIP ligands, respectively. Each of the 5-AIP moieties connects three Zn centers to form two-dimensional sheet-like structure along the *bc* plane (Fig. 2.1). The tetrahedral zinc centers have an angle between them of ~ 136 °, comparable to the Si – O – Si angle in the water stable ZIF (zeolitic imidazolate framework) structure. This particular structural arrangement may provide stability in an aqueous media like ZIF or zeolite structure. The two-dimensional sheets are connected by the 4,4'-AP ligand pillars of approximately 13 Å distance. As a result, one-dimensional, rectangular-shaped channels of dimension 8.25 × 13.02 $Å^2$ (without considering van der Waals radii) are formed. The one-dimensional channel is occupied by the disordered DMF molecules (Fig. 2.1).

Table 2.2. *Crystallographic parameters for compound* ***1****.*

Parameters	*{[Zn (4,4'-AP) (5-AIA)].DMF}$_n$, 1*
Empirical formula	*C16 H9 N4 O5 Zn*
Formula weight	*402.64*
Crystal System	*Monoclinic*
Space Group	*$P2_1/c$*
a(Å)	*14.9503(8)*
b(Å)	*7.7048(5)*
c(Å)	*16.0447(8)*
α(°)	*90*
β(°)	*107.581(3)*
γ(°)	*90*
Volume(Å^3)	*1761.85(17)*
Z	*4*
Calculated density (g/cm^3)	*1.518*
θ range (°)	*1.429 to 28.365*
Absorption coefficient (mm^{-1})	*1.428*
Reflections collected	*16490*
Unique reflections	*4400*
Goodness-of-fit	*1.070*
Number of parameters	*238*
Final R indices [I>2sigma(I)]	*R1 = 0.0452, wR2 = 0.1276*
R indices (all data)	*R1 = 0.0677, wR2 = 0.1494*
Largest diff. peak and hole e Å^{-3}	*0.919 and -0.735*

***Table 2.3**. Selected bond lengths & bond angles of compound **1**.*

Bonds	***Bond Length (Å)***
Zn (1) - O(1)	*1.941(3)*
Zn(1) - O(3)	*1.990(3)*
Zn(1) - N(1)	*2.043(4)*
Zn(1) - N(2)	*2.064(4)*
Bond angles	***Bond Angle (°)***
O(1) - Zn(1) - O(3)	*101.21(14)*
O(1) - Zn(1) - N(1)	*102.44(18)*
O(3) - Zn(1) - N(1)	*125.06(18)*
O(1) - Zn(1) - N(2)	*113.25(16)*
O(3) - Zn(1) - N(2)	*106.55(15)*
N(1) - Zn(1) - N(2)	*108.20(18)*
O(1) - Zn(1) - C(2)	*130.16(15)*
O(1) - Zn(1) - O(3)	*101.21(14)*
O(1) - Zn(1) - N(1)	*102.44(18)*
O(3) - Zn(1) - N(1)	*125.06(18)*
O(1) - Zn(1) - N(2)	*113.25(16)*
O(3) - Zn(1) - N(2)	*106.55(15)*
N(1) - Zn(1) - N(2)	*108.20(18)*
O(1) - Zn(1) - C(2)	*130.16(15)*
O(1) - Zn(1) - O(3)	*101.21(14)*

The crystalline phase purity of the powdered MOF sample is investigated and proved by the PXRD (powder-X ray diffraction) experiment (Fig. 2.2). Moreover, the PXRD patterns of compound **1** were analysed after soaking it in water, and some organic solvents (Fig. 2.2). The structural stability of the MOF was proved by obtaining matching PXRD patterns with the simulated one. The supernatant collected after a 24 hour MOF soaking is studied by ICP-AES(Inductively Coupled Plasma-Atomic Emission Spectroscopy) and the absence of any elements further proved the rigidity of compound 1 in water. The characteristics peaks for aromatic ligands is identified in the IR (infrared) spectrum of compound **1**(Fig. 2.3a). The

TGA (thermogravimetric analysis) spectrum revealed a primary weight loss up to 80 °C, corresponding to the loss of DMF molecules from the pores. The compound 1 has stability up to 115 °C, and it starts degrading on further heating (Fig. 2.3b). The fluorescence emission is collected for compound **1**, and the ligands 4,4'-azopyridine and 5-amino isophthalic acid (5-AIA) as their aqueous dispersions. The blue emission peak at 405 nm, when excited at 300 nm of the compound 1, corresponds to the 5-AIA ligand-centered electronic transitions (Figs. 2.3c &d). Also, the quantum yield (QY) of compound **1** is calculated as 11 % (see ESI). For analysing the selectivity, experiments with various mono and divalent interfering cations (Li^+, Na^+, K^+, Mg^{2+}, Ca^{2+}, Sr^{2+}, Ba^{2+}, Mn^{2+}, Ag^+, Fe^{2+}, Co^{2+}, Ni^{2+}, Cu^{2+}, Zn^{2+} and Cd^{2+}) are carried out which illustrate that the Hg (II)-induced fluorescence quenching was unaffected by other metal ions(Fig. 2.4a & b). Hence compound 1 can be considered as a selective sensor for Hg(II) ions in the aqueous medium. The control experiments were carried out with the ligand 5-AIA dispersion in water, and no visual colour change was observed after Hg(II) ions addition (Fig. 2.4c).

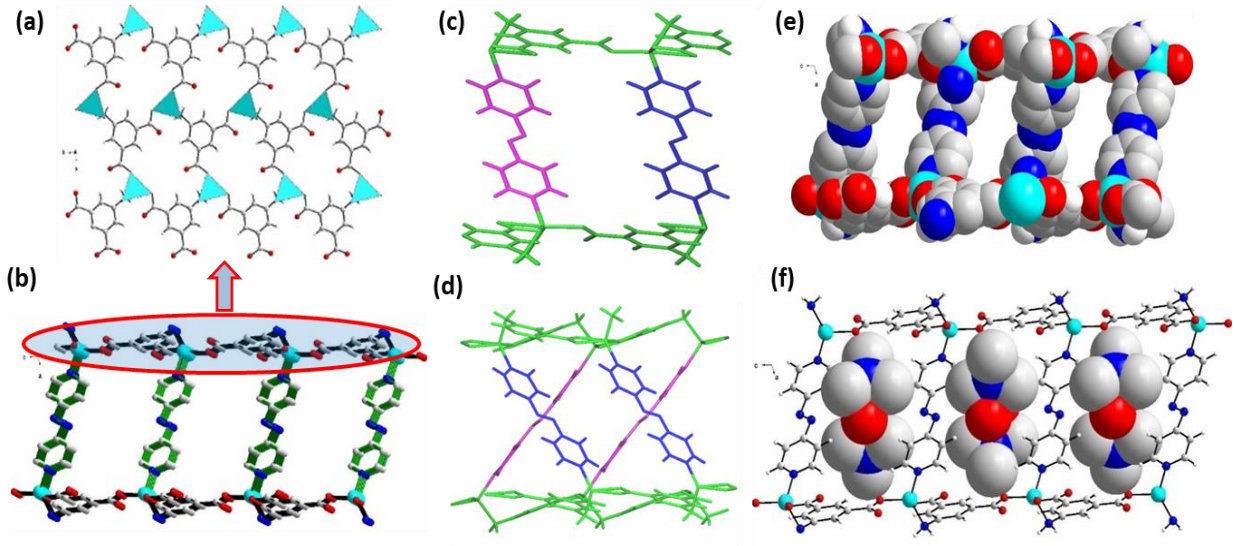

Figure 2.1. *The two-dimensional layered structure along the bc plane, (b) the three-dimensional structure of compound 1, where the two-dimensional layers are connected with*

4, 4'-azopyridine ligands, (c)& (d) showing the criss-cross arrangement of 4, 4'-azopyridine spacers, (e) space-filling model and (f) distorted DMF molecules in the pores of compound ***1.***

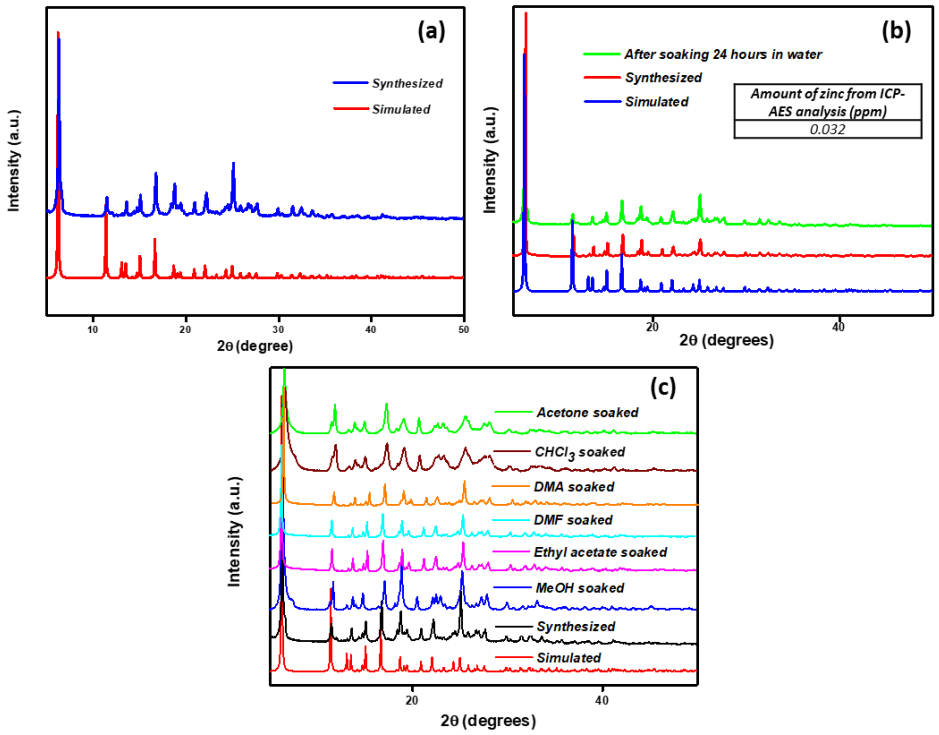

Figure 2.2. *The PXRD patterns of the synthesized MOF(a) showing the purity, (b) after soaking study in water (The ICP-AES analysis data is given as table) & (c) after soaking in different solvents for 24 h.*

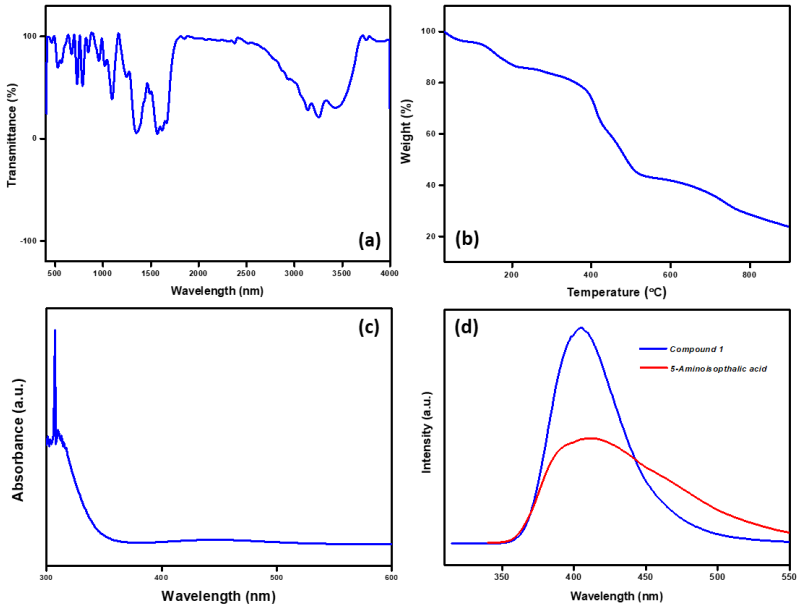

Figure 2.3. *(a) The infrared, (b) TGA, (c)UV & (d) photoluminescence spectra of compound* ***1****.*

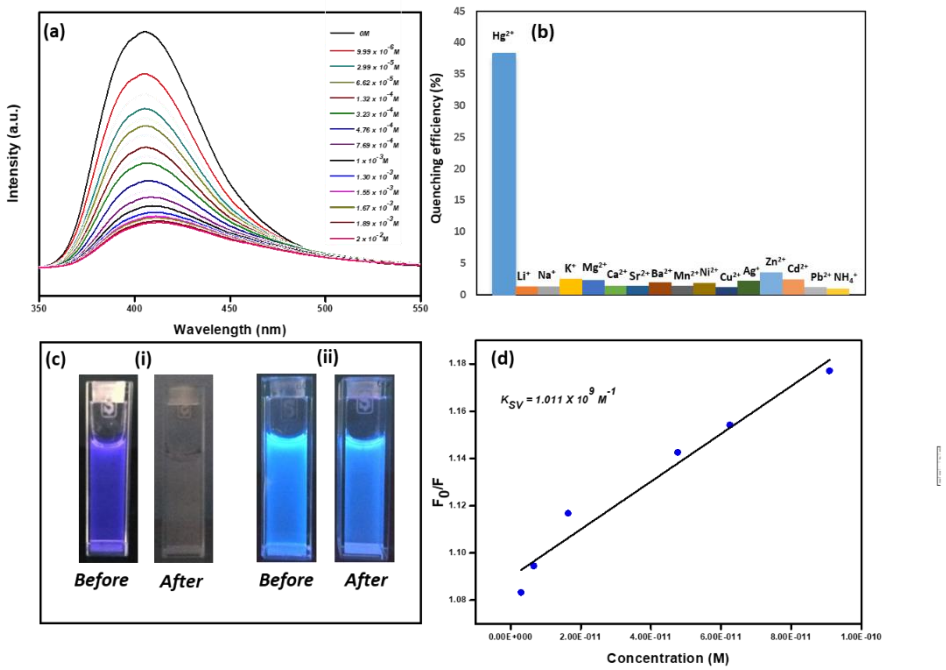

Figure 2.4. *(a) The graph illustrates the fluorescence quenching on the addition of Hg (II) ion, (b) the fluorescence quenching in percentage for selected metal ions in the aqueous medium at room temperature, (c) The colour change of (i) compound* ***1*** *and (ii) 5-Amino isophthalic acid ligand after adding Hg(II) under UV light and (d) the Stern-Volmer plot is showing the linear relation between quenching and the concentration of Hg (II) ion.*

This confirmed the importance of the Zn MOF scaffold with 5-AIA and AP in the selective sensing of Hg (II) ion. The mechanism of quenching is derived by the steady-state and time-resolved emission studies. The Stern-Volmer (SV) plot is used for analyzing the relative change in the fluorescence intensity as a function of the concentration of the Hg (II) ion, and SV constant is estimated to be 1.011×10^{9} M^{-1} (Fig. 2.4d).

The SV constant is the highest among those reported for Hg (II) ion detection using any MOF/coordination polymer-based sensors, nanomaterials or self-assembled

materials, according to our knowledge (Table 2.1). Moreover, there occurred a shift in the absorbance peak for compound **1** 330 nm on the addition of $Hg^{2+,}$ and it points to the formation of a ground-state complex between the fluorophore and Hg(II) (Fig. 2.5a). There is no peak at 330 nm in the excitation spectra of the compound **1** after adding Hg (II) ion, and it displays the nonemissive nature of the ground state complex which in turn suggests the presence of a static interaction (Fig. 2.5b). When a temperature-dependent quenching study is performed at a higher temperature, the K_{sv} value decreased. As the temperature increases the ground state interaction between compound **1** and Hg (II) ion gets disturbed, leading to lower K_{sv} value (Fig. 2.5c). Before and after the Hg (II) addition, the lifetimes obtained was comparable, which proves the static mechanism (Fig. 2.5d and Table 3.4). The lower detection limit of Hg (II) ions (9.9×10^{-12} M or 0.27 femtogram) obtained is the lowest reported value for a coordination compound till date (Fig. 2.6a and Table 2.1). Also, the LOD is lower than the maximum permitted level of Hg(II) ion in drinking water (10 nM) advised by US EPA. The excellent selectivity for Hg^{2+} is probably ascribed to a combination of many factors, such as right aperture size of the frameworks, appropriate radius, soft Lewis acidic nature of Hg^{2+} ion and the suitable soft basic sites in the structure.

As it is already stated, compound **1** has Zn centers connected to 5-AIA ligands forming the layered architecture. The $–NH_2$ group of 5-AIA is coordinated with the Zn ion. The 4, 4'-AP pillared the layered architecture to form the three-dimensional structure of MOF with the one-dimensional rectangular channels. Because of this skeleton of the one-dimensional channel, Hg (II) ions can access the channel quickly. The pyridine N atoms bonded with metal center while the –N = N – group is freestanding donors for metal ions. Mercury ion has a good affinity towards the N atoms. Hence, the binding of Hg (II) ions with the free-standing –N = N- group of 4,4'-AP disturbs the electron delocalization of the MOF, which subsequently changes

the fluorescence intensity. Our hypothesis is supported by the data from FTIR and XPS experiments of compound **1** with and without Hg(II). There is a small shift in the peaks in the FTIR spectrum corresponding to the stretching frequency of C-N bond, after the Hg (II) addition which supported this claim as well (Fig. 2.6b). The N 1s XPS core spectrum of the MOF exhibited a broad peak at around ~ 400 eV that can be deconvoluted to the three peaks at ~ 399.10 eV, ~ 402.36 eV and ~ 403.57 eV, assigned to the N atoms from pyridine group, azo group and coordinated $–NH_2$ group respectively.

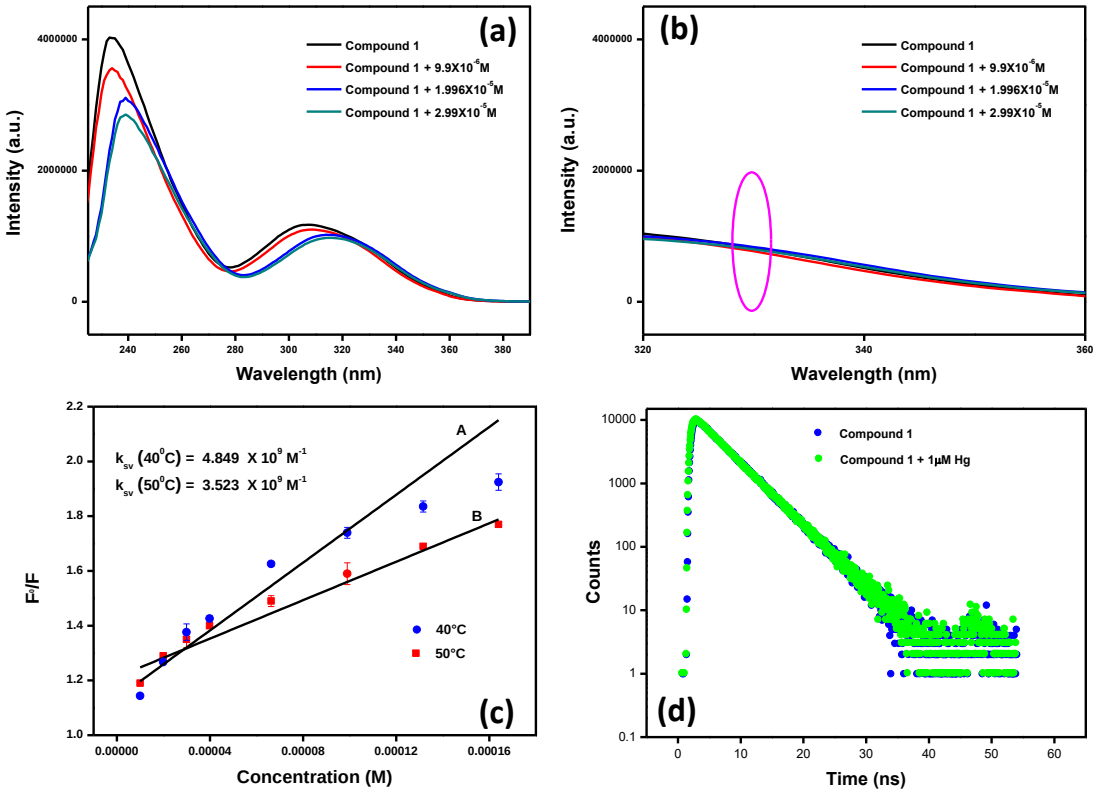

Figure 2.5. *(a) The excitation spectrum of compound **1** before and after the addition of Hg(II) ion, (b)the zoomed region 320-380 nm is showing the absence of a new peak at 330nm, (c) the temperature-dependent quenching study is showing the lowering of k_{sv} value as the temperature increases and (d) the lifetime decay plot of compound **1** before and after adding Hg(II) ion (n=3).*

Table 2.4. *The fluorescence lifetime of compound 1 before and after the addition of* Hg^{2+}.

	Zn-CP	Zn-CP + Hg^{2+}
X^2	0.994	0.989
Average lifetime, τ(ns)	4.421	4.398

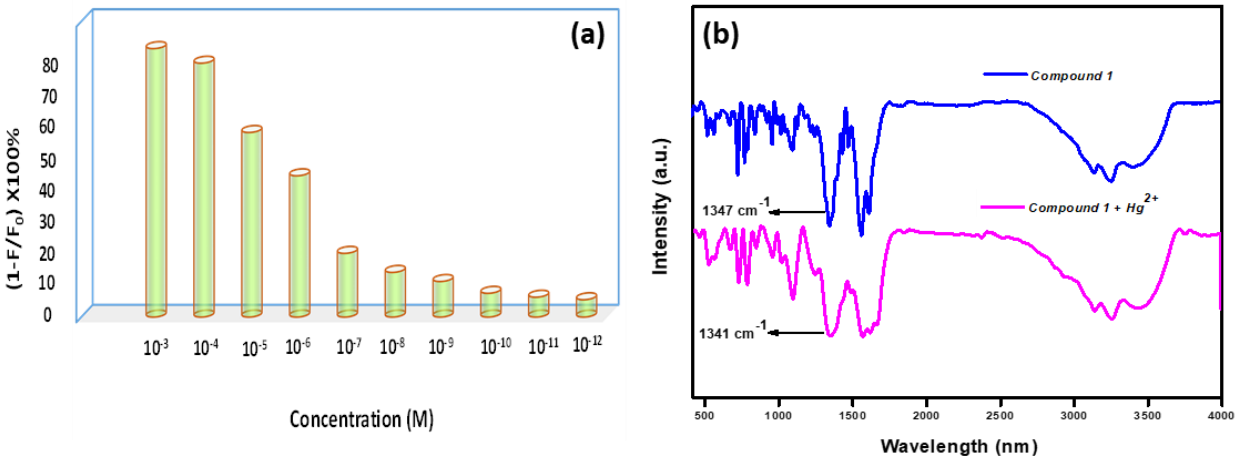

Figure 2.6. *(a) The percentage of quenching of fluorescence by adding Hg(II) ion solutions of different concentrations and (b) the IR spectra of compound* ***1*** *(a) before and (b) after the quenching studies. The highlighted area contains the shifted peaks. The C-N stretching bond has shifted from 1347cm*$^{-1}$ *to 1341 cm*$^{-1}$ *showing the interaction of Hg (II)to the azo group.*

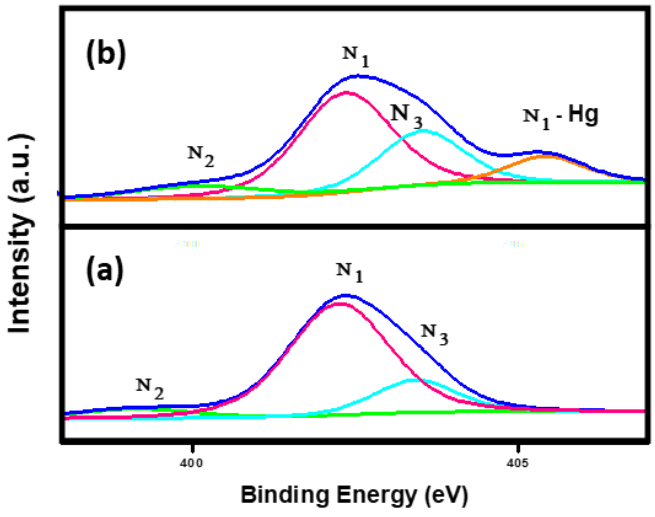

Figure 2.7. *XPS plots of compound **1** (a) before and (b) after binding with Hg (II) ion. N_1, N_2, and N_3 represent the nitrogen of azo, pyridine and amino group nitrogens*

.

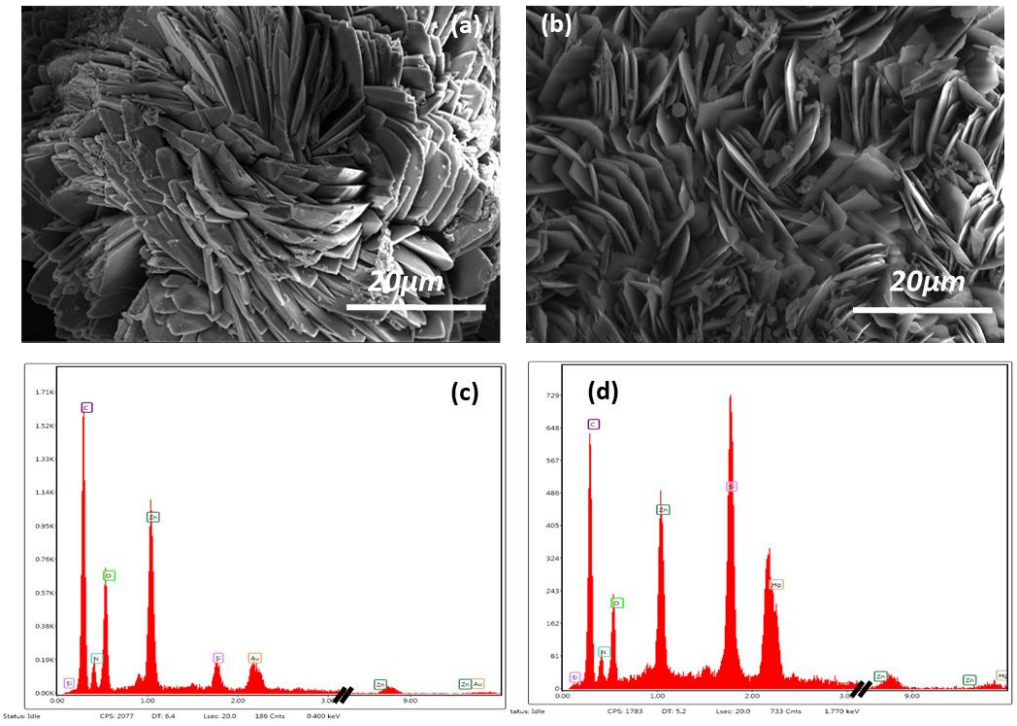

Figure 2.8. *The scanning electron microscopic image of the compound **1** showing the flower-like morphology and smooth surface (a) before and (b)after the quenching studies, the SEM-EDAX spectrum of compound **1** (c) before and (d) after the quenching study.*

All the above-said peaks got slightly red-shifted, and a new peak formed at ~ 405.53 eV, after the addition of Hg^{2+} ion. This indicates the interaction between the azo group nitrogen in compound **1** with the Hg(II) ion. The N atoms of the $–NH_2$ group and pyridine group are bonded with the metal, and the azo group is free. So Hg(II) can only interact with the freestanding –N = N – group and leads to the electron density loss at the azo group center which in turn raises its binding energy (Fig. 2.7).[90],[80] It is also to be noted that, the size of the one-dimensional channel between –N = N – groups of the 4, 4'-AP molecules is perfectly suitable for the large Hg (II) ions than

other metal ions. Various characterization studies investigate the binding of Hg (II) ion to compound 1 after the quenching experiment.

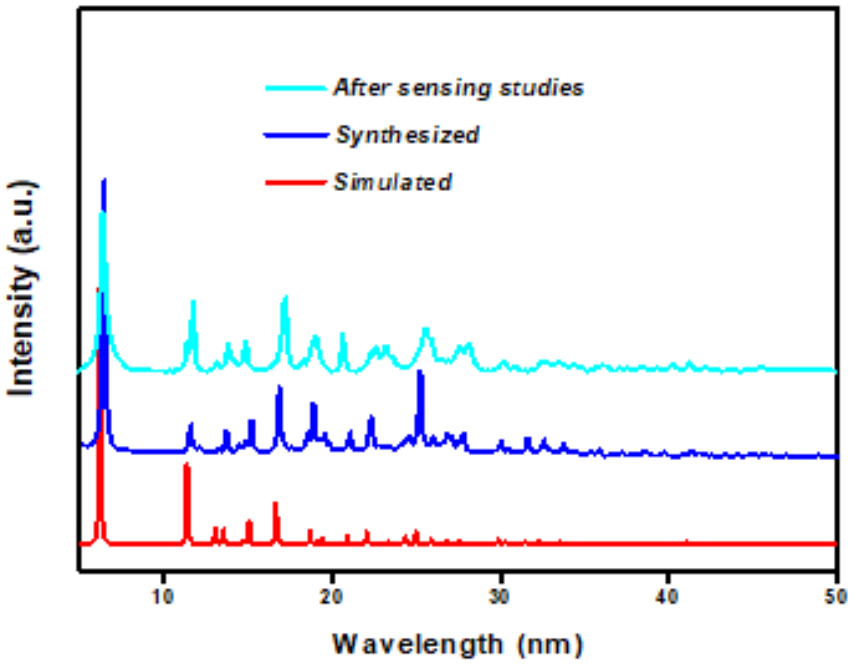

Figure 2.9. *PXRD pattern of compound 1 before and after Hg (II) ion sensing in the aqueous medium.*

The SEM (scanning electron microscope) image after the quenching studies shows no change in morphology (Figs. 2.8a & b). The SEM-EDX spectra illustrate the presence of mercury in the MOF sample after the quenching(Figs. 3.8c & d). The stability of the MOF is proved by collecting the PXRD spectrum after the quenching experiment (Fig. 2.9).

For the real water sample analysis, water is collected from four different sources such as seawater, river water, tap water, and drinking water and are tested for the possible presence of mercury by ICP-AES. It was found that except seawater which has a negligible amount of mercury in it, there is no presence of mercury in the other water samples (Table 2.4). The standard addition method was followed for the sensing study. Surprisingly in three of the water samples, we could detect the mercury ions with more or less similar sensitivity compared to the standard MOF dispersions prepared in distilled water. Mercury, up to 16.7

%, could be detected even in the seawater (Table 2.5). These results show that compound **1** can have notable accuracy and reproducibility to detect Hg (II) ion in natural water samples, which implies the utility of the present probe in studying the environmental samples.

Towards real application, a solid-state sensor with compound **1** is made. The single crystals of compound **1** were carefully grown over an aluminium foil and are used for the detection of Hg (II) in the aqueous medium (Fig.2.10). The solid sensor shows sensitivity to the micromolar level. The quenching efficiency of the solid-state sensor was not much compared to the aqueous dispersion mainly due to the inhomogeneity of the single crystals grown.

Table 2.4. *The ICP-AES data of compound **1** after soaking in different natural water (n=3).*

Sl. No.	Sample	Amount of mercury (mg/L)
1	Drinking water	Nil
2	Tap water	Nil
3	Tream water	Nil
4	Sea water	$0.011 \pm 0.002 \times 10^{-3}$

Table 2.5. *Natural water sample analysis (n=3).*

Water samples[a]	Added concentration of Hg^{2+} (μM)	Detected concentration of Hg^{2+} (μM) [b]	Relative standard deviation(%) [c]
Sea Water[d]	50	8.33 ± 0.35	4.26
	100	13.92 ± 0.65	4.69
River Water	50	49.88 ± 1.18	2.37
	100	99.75 ± 0.34	0.34
Tap Water	50	48.79 ± 0.09	0.18
	100	97.44 ± 0.92	0.94
Drinking Water	50	52.16 ± 2.50	3.76
	100	105.54 ± 4.67	4.08

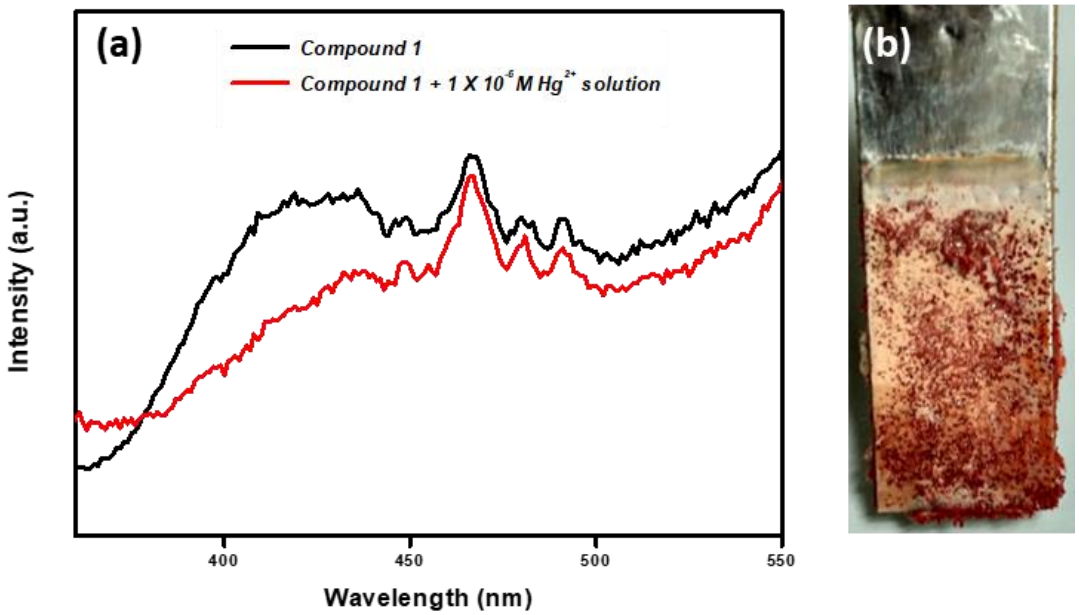

Figure 2.10. *(a) The emission spectrum of the crystals of compound **1** formed on Al foil before (black line) and after (red line) dipping in Hg^{2+} ion solution of concentration 1×10^{-6}M (b) the photograph of crystals of compound **1** grown on aluminium foil.*

2.3 Conclusions

A Zn-based MOF (compound **1)** was synthesized for the selective and sensitive detection of Hg (II) ions in the aqueous medium. The compound **1** is water-stable and has a LOD of picomolar (femtogram) concentration of Hg (II) ion with a very high quenching constant (1.011×10^9 M^{-1}). It can selectively and sensitively detect Hg (II) ions without the interference of other co-existing metal ions in the aqueous medium. The selective interaction of the Hg (II) ion with the –N = N- groups of 4, 4'-AP in the one-dimensional rectangular channel of compound **1** disturbs the electronic structure of the scaffold which in turn lead to the fluorescence quenching. Natural water samples from various sources are analyzed, which revealed that compound **1** is a promising probe for the Hg (II) ions sensing and hence could be used to study environmental water samples. The compound **1** could be made into a solid-state sensor by growing the MOF crystals over the Al foil.

2.4 Experimental section

2.4.1 Materials

The reagents used were all commercially available and are used as provided without further purification. [$Zn(NO_3)_2 \cdot 6H_2O$], 4,4'-Azopyridine (4,4'-AP) and 5-Aminoisopthalic acid (5-AIA) and all the metal salts were purchased from Sigma-Aldrich.

2.4.2 Methods of Characterization and Instrumentations

Instrumentations

Powder X-ray diffraction spectra were collected using an X'pert PRO (PANalytics) powder diffractometer equipped with CuKα radiation (1.5405 Å). The elemental analysis (C, H, and N) was carried out on a vario MICRO cube elemental analyzer. The FT-IR spectrum was recorded from KBr pellets in the range of 4000-400 cm^{-1}, using an FT-IR prestige-21 (Shimadzu) spectrometer. The TGA was performed on an SDT Q600 (Shimadzu) analyzer in flowing nitrogen with a heating rate of 10 ºC per minute. UV-Vis spectra were collected at room temperature in the solid-state set up on a UV-3800 SHIMADZU UV-Vis-NIR spectrophotometer. The fluorescence spectra were obtained using the Fluoromax fluorimeter. FEI NOVA NANOSEM 450 scanning electron microscope (SEM) with acceleration voltage 15 kV was used to determine particle size and morphology and to collect EDX spectra. Lifetime measurements were performed in an IBH picosecond time-correlated single-photon counting (TCSPC) system. The pulse width of the excitation (λ_{exc}=375 nm) source is determined to be < 100ps. The fluorescence decay profiles were de-convoluted using IBH data station software version 2.1, and fitted with exponential decay, minimizing the $\chi 2$ values. XPS measurements have been done using the omicron instrument, and the data is solved using the casa XPS software. The ICP-AES measurement was carried out from SAIF, IIT Bombay. The instrument model is Arcos simultaneous ICP spectrometer.

Single-crystal diffraction and Characterizations

Crystallographic data collection and refinement

The single-crystal diffraction data is collected using a Bruker AXS Smart Apex CCD diffractometer at 298 K. The X-ray generator was operated at 50 kV and 35 mA using a MoKα (λ = 0.71073 Å) radiation. The data were analyzed using SAINTPLUS[91], and an empirical absorption correction was applied using the SADABS program[92] The crystal structure was determined by direct methods using SHELXS 2014 and refined using SHELXL 2014 present in the SHELXTL V6.14[93] package. All the non-hydrogen atoms were located from the difference Fourier map and refined anisotropically. All hydrogen atoms were fixed using HFIX. Full-matrix least-squares structure refinement against F^2 was carried out using the WINGX[94] package of programs. The crystallographic information file is deposited with CCDC number 1831742.

Synthesis of [Zn (4,4'-AP) (5-AIA) DMF]$_n$ (Compound 1).

Compound **1** was synthesized with solvothermal conditions at 100 °C. The reagents $Zn(NO_3)_2 \cdot 6H_2O$ (0.025 g, 0.1 mmol), 4,4'-AP (0.018 g, 0.1 mmol) and 5-AIA (0.019 g, 0.1 mmol) were mixed and dissolved in a glass vial in 10 mL DMF by sonication and was kept at 100 ℃ for 20 hours. After it is cooled to room temperature, the dark brown block crystals of compound 1 were isolated and washed with DMF and dried in air. Crystals were activated at 70 ˚C in a vacuum before the sensing studies. (Yield = 68 %) Anal.calc. for C_{13} H_9 $N_{1.50}$ $O_{4.5}$ Zn: C - 48.25 %; H -2.8 %; N - 6.49 %; Found: C - 48.12 %; H - 3.2 %; N - 6.82 %.

ICP-AES analysis

One milligram of the MOF is added to a 5 mL mercury ion solution (10^{-6} M concentration) in a glass vial. The vial was sonicated for 30 minutes and kept undisturbed for 24 hours. The solution is centrifuged, and the supernatant was collected. The supernatant was diluted to five times its volume and was analyzed by ICP-AES.

Quantum Yield Measurement

The relative quantum yield was calculated for compound 1 with 0.1 M quinine sulfate (φ_r = 0.546) as the reference. The optical density of both the reference and the compound was made to a value close to 0.1 by keeping the slit width equal to one. The emission spectra were also noted for both at the same slit width by exciting at 310 nm. The quantum yield of the compound was measured relative to the reference by using the following equation

$$\varphi_s = \varphi_r \left(\frac{OD_r}{OD_s}\right)\left(\frac{I_s}{I_r}\right)\left(\frac{n_s^2}{n_r^2}\right)$$

where, φ_r and φ_s are quantum yields of sample and reference respectively, OD is the optical density, I is the area under the curve for the emission spectra, and n is the refractive index of the medium.

Chapter 3

Water Stable Boronic Acid Grafted Ba-based MOFs for the Selective Adsorption of Cis-Diols

Abstract

Boronic acid groups suspended MOFs are a novel class of adsorbents for cis-diols due to the high affinity between them. This work explains, the use of Metal-ligand-fragment-coassembly (MLFC) method for the synthesis of a series of barium-based water-stable MOFs with suspended free boronic acid moieties in the scaffold. The enhancement in the boronic acid inclusion as the feed amount of boronic acid moiety increases is investigated by the ^{11}B NMR (nuclear magnetic resonance) and XPS (X-ray photoelectron spectroscopy) analysis. The studies reveal the importance of the furanose isomeric form of cis-diols in the aqueous medium in determining the adsorption efficiency. Galactose, with its 7% molecules in the furanose isomeric form, interact well with the boronic acid fragments and is the favourable adsorbate. All the constructed MOFs were identified as good adsorbates for isolating cis-diols from their aqueous solutions.

3.1 Introduction

Several biologically important class of molecules like carbohydrates, glucosides, glycoproteins and so on has cis-diols as the main component in their structure.[95] They serve various functions in biological systems, like the human and animal body, and hence are essential for the life existence.[96],[97] A successful analysis of cis-diol containing molecules demands their isolation and separation due to their low abundance.[98] A wide variety of sophisticated techniques like high-performance liquid chromatography (HPLC),[99] gas chromatography (GC)[100] and capillary zone electrophoresis (CZE) is already present for the quantitative analysis of cis-diols,[101]. Still, the isolation methods are essential before a competitive strategy. Adsorption is a highly efficient concentration technique for cis-diols where the adsorbents play a cardinal role.[102] Even though a hand full of adsorbents are already in use, the boronic acid-based adsorbents stand out because of their selective binding ability to cis-diols.[103],[104] The boronic acid fragments could either be attached toa membrane surface or suspended in it for a photochemical or electrochemical response.[105],[106] The boronic acid groups are known for their affinity to interact with cis-diols in an alkaline medium forming an ester[107]; therefore adsorbents with boronic acid moieties are in the limelight in the field of cis-diols enrichment and separation.[108],[109]

Polymeric materials like Metal-organic frameworks (MOFs)[110] are known for their application in the adsorption and removal of several analyte molecules from various solvent systems.[31],[111] Synthesizing a MOF with a ligand with desired functional groups, and its structural fragment is termed as Metal-ligand-fragment-coassembly (MLFC). It is an excellent way of introducing mesopores into the MOFs. The significant advantage of MLFC over the post-synthetic modification (PSM) is its ability to reduce the chance of clogging the pores.[112],[113] In this way, a high-performance functional material could be constructed by

grafting a desirable functional group into the MOF, which has a distinct affinity for a substrate.[114]

3.2 Results and discussion

The solvothermal synthesis of a new Ba-based MOF with 1,3,5-benzene tricarboxylic acid (BTC) ligand (**1-B**) and a group of six boronic acid suspended MOFs with analogous structures of **1-B** was carried out. All the analogues of **1-B** are synthesized by following the MLFC approach by adding calculated amounts of the structural fragment of BTC, 5-boronoisopthalic acid (BIA) (Scheme 3.1). The MLFC is an innovative scheme which helps in making modified MOFs by the co-assembly of a ligand and its structural fragment. As a result, defective MOFs could be formed which are superior in some properties like surface area, porosity, and reactivity compared to the parent MOF.[115],[116] Here, some of the BTC moieties in the MOF scaffold get replaced by the fragment 5-which, in turn, introduces the free boronic acid groups into the framework. The boronic acid incorporated MOFs are named **(1:6)-B** to **(1:1)-B,** in which the feed ratio of BIA to BTC varies from 1:6 to 1:1. All the MOFs (**(1:6)-B** to **(1:1)-B)** along with the parent framework **1-B** are tested for their ability to adsorb various cis-diols in the aqueous medium in an alkaline atmosphere.

Scheme 3.1*. Scheme showing the synthesis of Ba-MOFs with and without modulator and the affinity of MLFC guided MOFs towards cis-diols.*

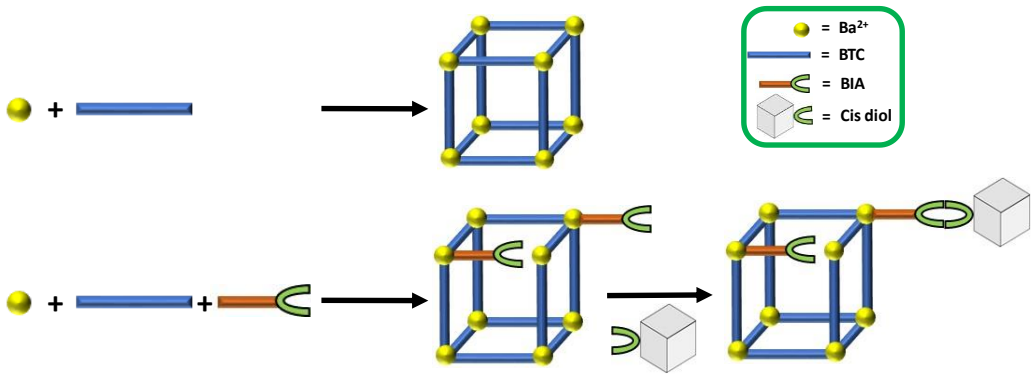

Table 3.1. *Crystal data and structure refinement details for* ***1-B***

Identification code	*1-B*
Empirical formula	$C_9H_9Ba_{1.50}O_{11}$
Formula weight	*499.17*
Crystal System	*Monoclinic*
Space Group	$P2_1/c$
a(Å)	*12.5705(9)*
b(Å)	*15.9756(11)*
c(Å)	*6.8196(5)*
α(°)	*90*
β(°)	*91.042(3)*
γ(°)	*90*
Volume (Å³)	*1369.29(17)*
Z	*4*
Calculated density (g/cm³)	*2.421*
θ range (°)	*1.620 to 28.353*
Absorption coefficient (mm⁻¹)	*4.365*
Reflections collected	*13062*
Unique reflections	*3413*
Goodness-of-fit	*1.109*
Number of parameters	*191*
Final R indices [I>2sigma(I)]	$R_1 = 0.0228, wR_2 = 0.0616$
R indices (all data)	$R_1 = 0.0253, wR_2 = 0.0638$
Largest diff. peak and hole e Å⁻³	*1.173 and -1.140*

Table 3.2. *Selected bond lengths & bond angles of compound* ***1-B***

Bond	***Bond Length (Å)***
Ba (1) - O(1)	*2.851(2)*
Ba (1) - O(3)	*2.776(2)*
Ba(1) - O(4)	*2.725(2)*
Ba(1) - O(5)	*2.822(2)*
Ba(1) - O(6)	*2.653(2)*
Ba(1) - O(8)	*2.764(2)*
Ba(1) - O(9)	*2.868(2)*
Ba(1) - O(10)	*2.850(3)*
Ba(2) - O(1)	*2.968(2)*
Ba(2) - O(2)	*2.812(2)*
Ba(2) - O(3)	*2.974(2)*
Ba(2) - O(5)	*3.017(2)*
Ba(2) - O(7)	*2.750(2)*

Bond	***Bond Angle (°)***
O(1)-Ba(1)-O(3)	*66.62(6)*
O(1)-Ba(1)-O(4)	*131.11(7)*
O(1)-Ba(1)-O(5)	*69.68(7)*
O(1)-Ba(1)-O(6)	*75.33(7)*
O(1)-Ba(1)-O(8)	*135.69(6)*
O(1)-Ba(1)-O(9)	*65.66(6)*
O(1)-Ba(1)-O(10)	*121.63(7)*
O(3)-Ba(1)-O(4)	*155.92(6)*
O(3)-Ba(1)-O(6)	*125.06(7)*
O(3)-Ba(1)-O(8)	*80.43(6)*
O(5)-Ba(1)-O(3)	*64.07(7)*
O(5)-Ba(1)-O(4)	*103.86(6)*
O(5)-Ba(1)-O(6)	*134.81(7)*
O(5)-Ba(1)-O(8)	*69.57(7)*
O(6)-Ba(1)-O(4)	*78.58(7)*
O(6)-Ba(1)-O(8)	*148.72(7)*
O(8)-Ba(1)-O(4)	*75.71(6)*
O(9)-Ba(1)-O(3)	*122.46(6)*
O(9)-Ba(1)-O(4)	*66.68(6)*
O(9)-Ba(1)-O(5)	*70.61(6)*
O(9)-Ba(1)-O(6)	*69.38(6)*
O(9)-Ba(1)-O(8)	*114.92(6)*
O(10)-Ba(1)-O(3)	*86.05(7)*
O(10)-Ba(1)-O(4)	*93.97(7)*
O(10)-Ba(1)-O(5)	*141.60(7)*
O(10)-Ba(1)-O(8)	*82.70(7)*
O(10)-Ba(1)-O(9)	*147.45(7)*

3.2.1 Structural Description of 1-B

Single crystal X-ray diffraction studies revealed that **1-B** crystallizes in the $P2_1/c$ (monoclinic) space group (Tables 3.1 & 3.2). The asymmetric unit comprises two Ba^{2+} ions in different coordination geometries, a BTC ligand, two coordinated water molecules, and a guest water molecule (Fig. 3.1a). The trinuclear barium SBUs consists of a deca-coordinated barium ion connected to the octa-coordinated, symmetrically equivalent barium atoms on

each side (Fig. 3.1b). The end connected barium atoms (Ba (1)) bind to three BTC ligands and two water molecules. The Ba-O (carboxylate) bond lengths are between 2.653(2) and 3.017(2) Å. The obtained bond lengths are similar to the alkaline earth metal-oxygen (carboxylate) bonds already reported.[117],[118] These trimeric Ba-units are linked through carboxylate moieties to form the three-dimensional framework (Fig. 3.1d).

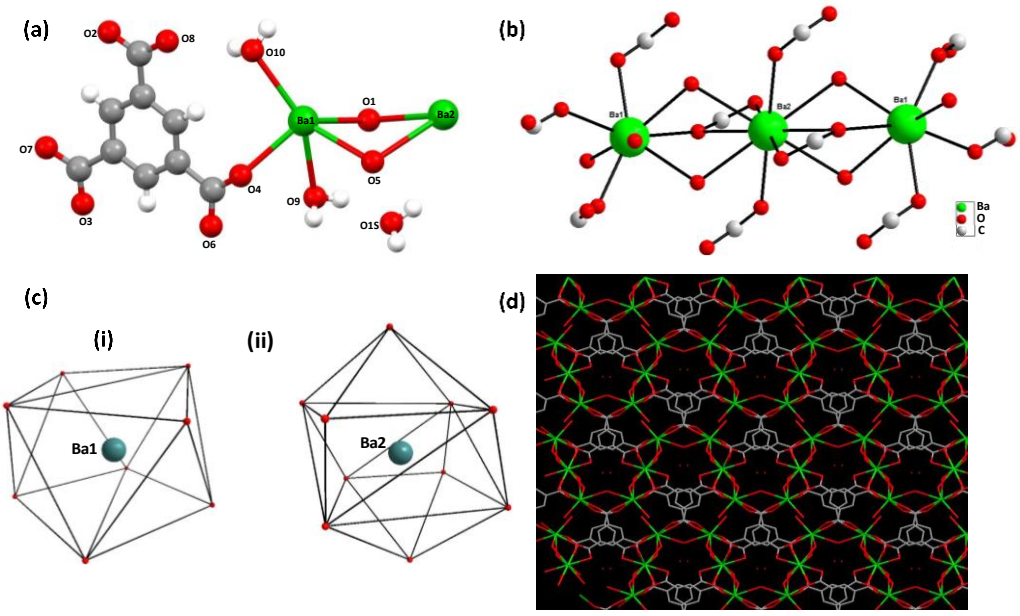

Figure 3.1. *(a)The asymmetric unit and (b) secondary building unit of* ***1-B****. (c) (i) and (ii) represent the Ba (1) trigonal bicapped prism and Ba (2) bicapped square antiprismatic geometries, respectively. (d) the three-dimensional framework structure of* ***1-B****.*

3.2.2 Structural Description of the MOFs (1:1)-B to (1:6)-B

The series of six boronic acid MOFs was formed by adding calculated amounts of BIA during the synthesis of **1-B**. We anticipated the replacement of a part of linker BTC by the BIA ligands with a similar structure as that of **1-B**. The PXRD spectra of the boronic acid incorporated MOFs (**(1:1)-B to (1:6)-B**) are in agreement with the PXRD pattern obtained from the single-crystal data of the parent MOF **1-B**, indicating the purity of all the compounds.

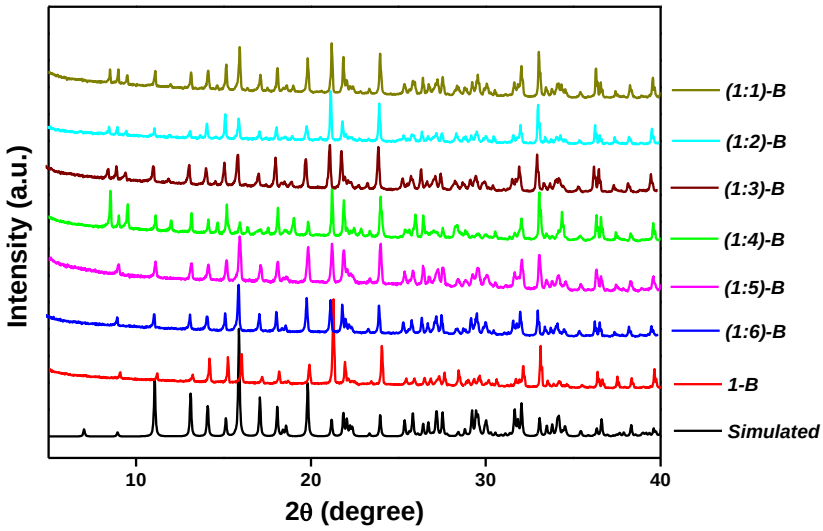

Figure 3.2. *(a) PXRD pattern of all the as-synthesized MOFs.*

This additional evidence revealed that the MOFs prepared by the addition of calculated amounts of BIA has the same structure as the parent MOF 1-B (Fig.3.2). TGA spectra reveal that all the MOFs have high thermal stability (Fig. 3.3).

3.2.3 Incorporation of the boronic acid group

The presence of suspended boronic acid groups in the MOFs, **(1:6)-B** to **(1:1)-B** was proved and quantitatively calculated using the ^{11}B-NMR studies. The NMR peaks at -17.3 ppm and -20.4 ppm corresponds to the boron atoms of BIA and the reference compound $NaBF_4$, respectively. The amount of BIA added during the MOF synthesis (which is known) is taken as the theoretical data and is compared to that of the incorporated amount calculated from the area under the NMR peaks.

By comparing the theoretical and experimental data, it was found that the incorporated BIA increases proportional to the feed amount and it reaches the highest possible coordination by maintaining the structural rigidity (Figs. 3.4 & 3.5). There was a maximum uptake of BIA of 73.76 % in **(1:1)-B**, corresponding to 0.0612 mmol of BIA per gram of the MOF. Any more

attempt to enhance the feed of BIA during the synthesis results in the formation of an unknown structure, as evidenced by the PXRD spectra (Fig. 3.6).

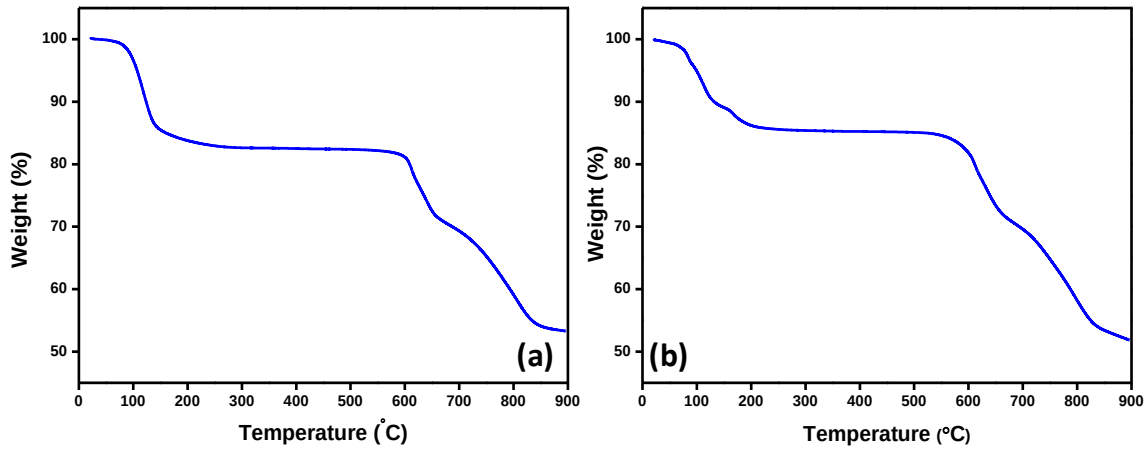

Figure 3.3. *The TGA graphs of (a) 1-B & (b) (1:1)-B.*

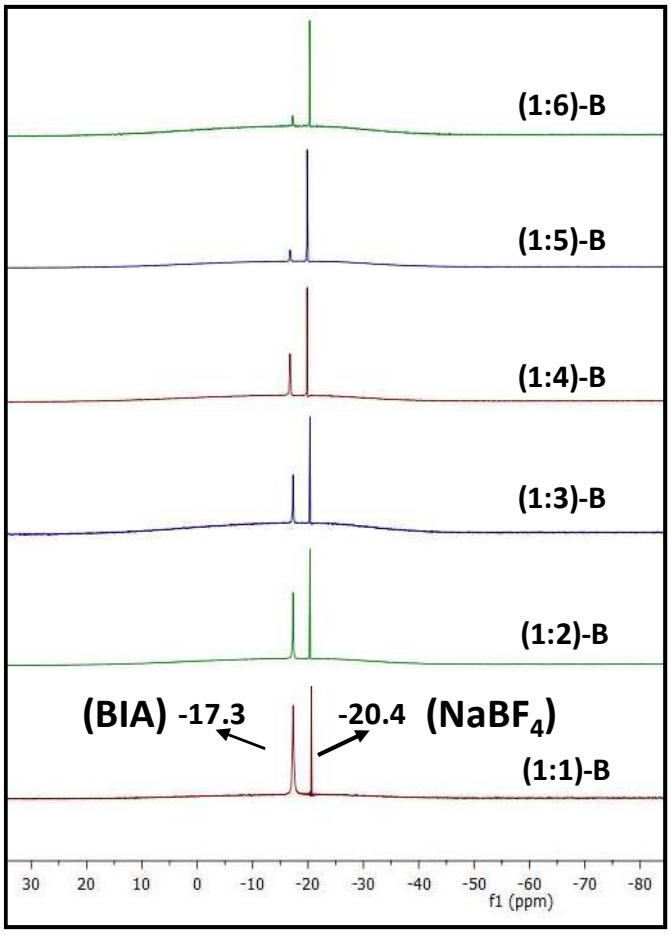

Figure 3.4. *^{11}B NMR spectrum of all the MOFs.*

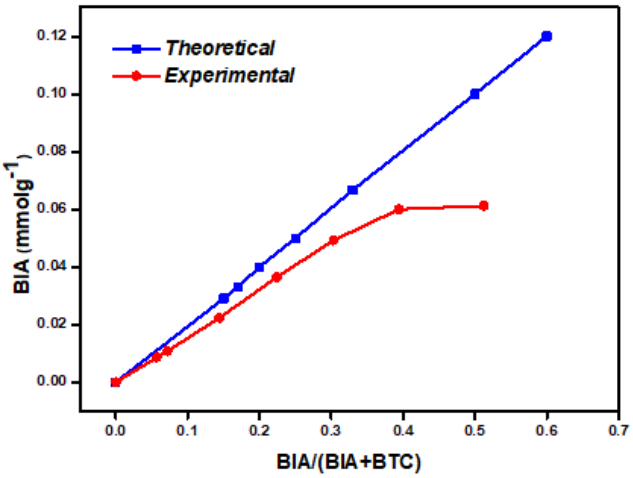

Figure 3.5. *Theoretical and experimental quantitative graph of BIA molecules suspension in the MOF structures.*

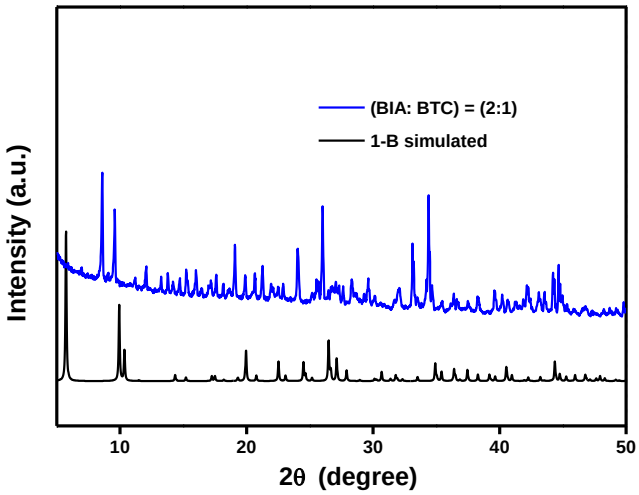

Figure 3.6. *The PXRD pattern shows the formation of an unknown structure when the amount of BIA in the feed increases beyond 1:1.*

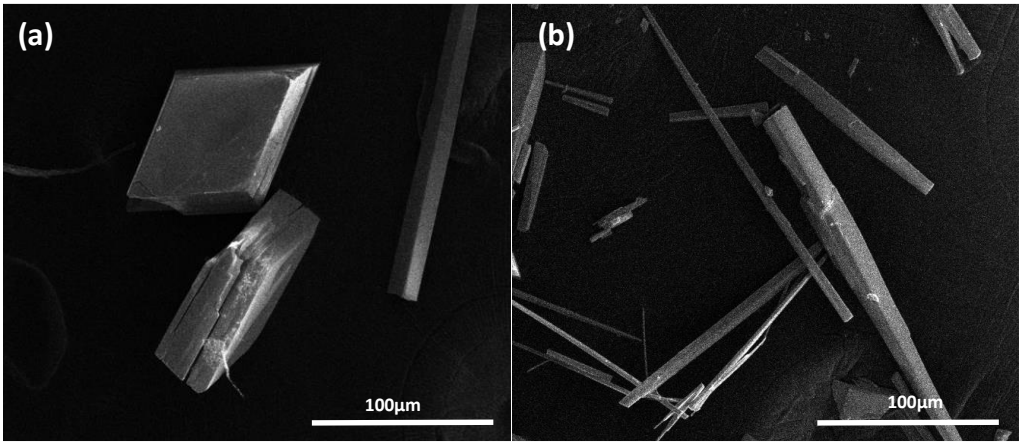

Figure 3.7. *SEM images of (a) 1-B and (b) (1:1)-B.*

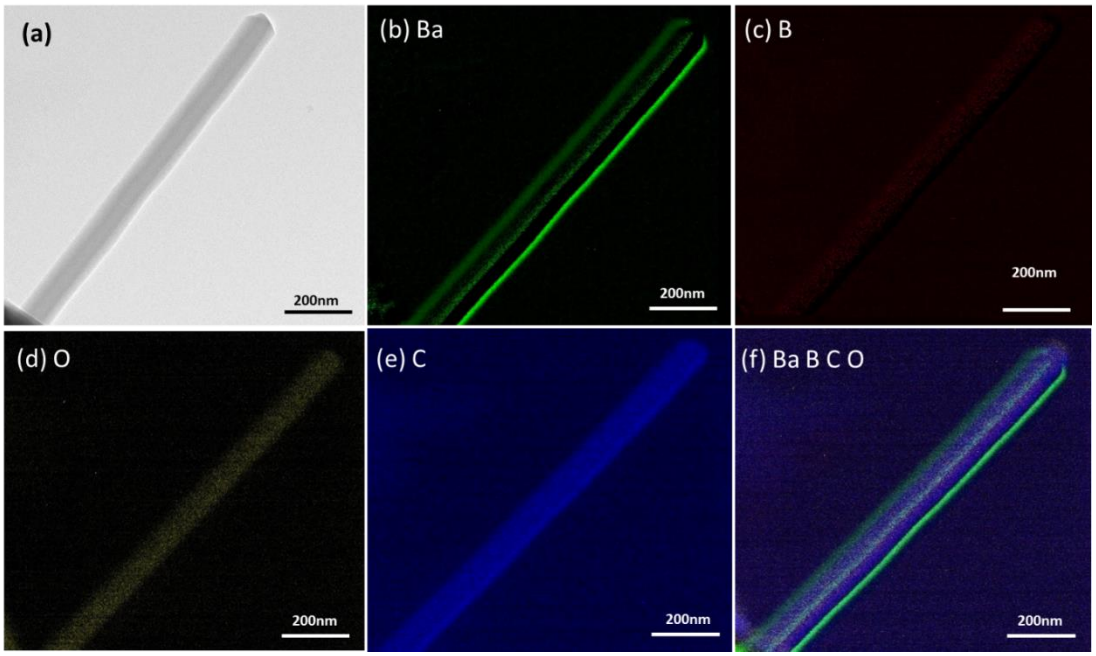

Figure 3.8. *(a)The TEM image, TEM-EDX spectrums of the elements (b) barium, (c) boron, (d) oxygen, (e) carbon and the (f) overlap EDX image collected from (1:1)-B.*

Scanning electron microscopic images reveal that the 1-**B** MOF has a perfect diamond shape with a very smooth surface (Fig. 3.7). The cross-section of the diamond shows its layered structure and the possibility of having cleavage and layer shearing. All the BIA suspended MOFs (**(1:1)-B** to **(1:6)-B**) have rode-like structure that is assumed to be formed by the breakage of diamond crystal. The elemental mapping of TEM-EDX (transmission electron microscopy-energy dispersive x-ray analysis) of the BIA incorporated MOF shows a uniform distribution of the elements barium, boron, carbon, and oxygen throughout the crystal (Fig. 3.8). The XPS analysis as well illustrates the incorporation of boronic acid (Fig. 3.9). The B 1s peak in the XPS survey spectrum proves the presence of BIA in **(1:1)-B**. The figure 3.9d displays the change in the intensity of peaks corresponding to C-O, C-B, C-C/C=C, and O-C=O bonds in the frameworks. As the feed ratio of BIA to BTC enhances from (1:6) to (1:1), the intensity of the C-B bond peak at 283.89 eV upsurges.

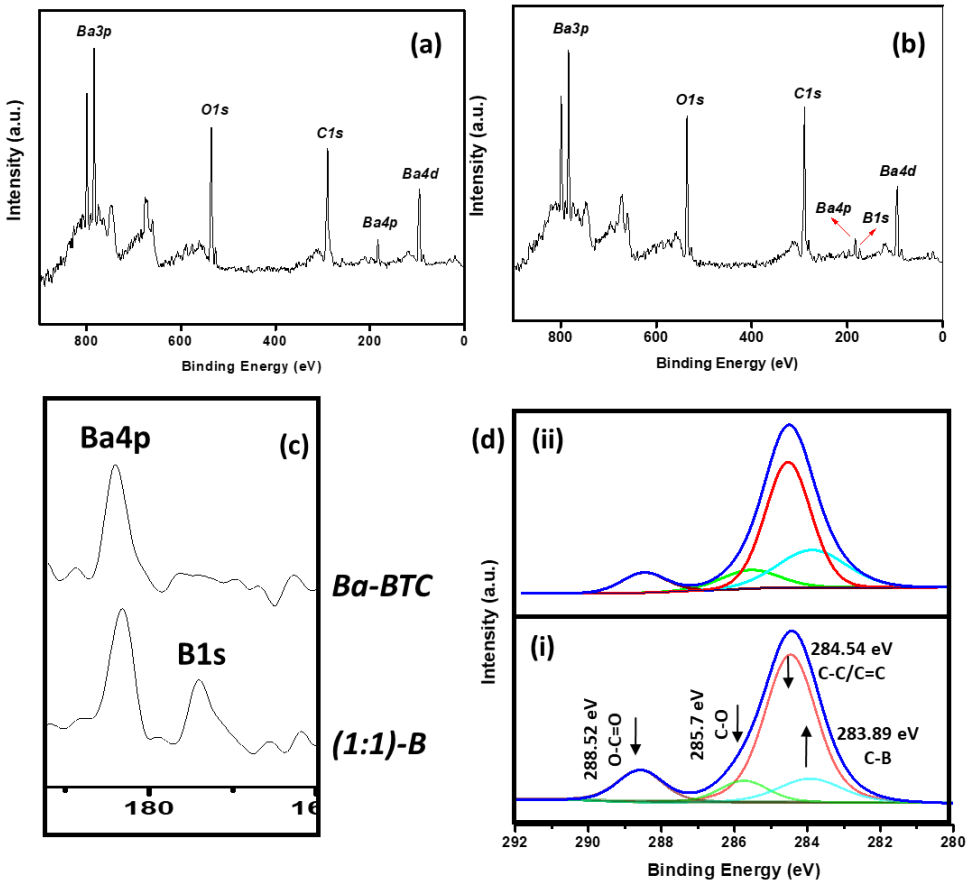

Figure 3.9.*XPS survey spectra of (a)**1-B** and (b) **(1:1)-B**, (c) the zoomed region of the elemental XPS spectra showing the presence of boron, the d (i) & (ii) are the deconvoluted C1s peaks of **(1:6)-B** and **(1:1)-B**.*

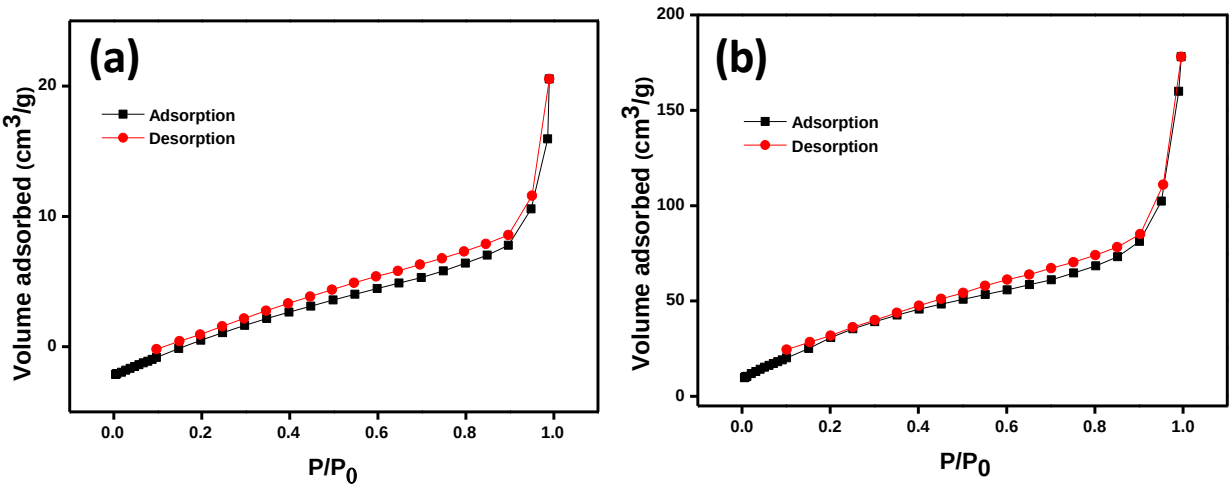

Figure 3.10. *The N_2 adsorption spectra of (a) **1-B**& (b) **(1:1)-B**.*

Moreover, the decrease in the intensities of peaks of O-C=O, C-O, and C-C/C=C bonds designate the corresponding decline in the amount of BTC. This proved that BIA was installed in the MOF frameworks. The N_2 adsorption-desorption isotherm was collected for all the MOFs, and the surface area was found to be increased gradually with the enhancement of boronic acid in the structure (Fig. 3.10 and Table 3.3). This may be due to the formation of coordinatively unsaturated metal sites in the MOF structure from missing linker defects.[119]

Table 3.3. *The BET surface area values of all the MOFs.*

MOF	***Surface area (m^2/g)***
(0 : 1)-B (parent MOF)	*27*
(1 : 6)-B	*32*
(1 : 5)-B	*48*
(1 : 4)-B	*70*
(1 : 3)-B	*96*
(1 : 2)-B	*128*
(1: 1) B	*142*

3.2.4 Carbohydrate Adsorption studies

The replacement of some of the tricarboxylic BTC linker molecules, with the dicarboxylic BIA molecules helps in the formation of defective sites in the MOF scaffold. Hence the suspension of BIA molecules not only introduces new boronic acid moieties in the framework but also helps in enhancing the surface area of the resultant scaffold by creating defect sites.[120],[121] The pH range of 6-9 is used for the adsorption study: ANOVA did not show the presence of significant differences between the responses achieved at pH 8 and 9 ($p>0.05$), so pH 8 was considered as the optimum (Fig. 3.11). The PXRD spectra after soaking each MOF in the water of different pH values is checked for the structural stability (Fig. 3.12a). The adsorption data collected using the activated MOFs with suspended BIA was compared with that obtained using the parent compound, **1-B** and to one another. The efficiency of

adsorption was found to be better for the **(1:1)-B** MOF as expected as it has the highest amount of BIA among all BIA instilled MOFs. Moreover, the adsorption efficiency of the cis-diols follows the order, galactose > glucose > mannose > xylose. The desorption of the adsorbed cis-diols on the MOF was not accomplished because of the instability of all the MOFs in acidic conditions.

The IR spectrum of the **(1:1)-B** was collected before and after the adsorption of galactose and is compared with that of the pure galactose molecule. The appearance of the new peak near 2950 cm^{-1} in the galactose adsorbed MOF shows the presence of C-H bonds of the galactose molecules (Fig. 3.12b).

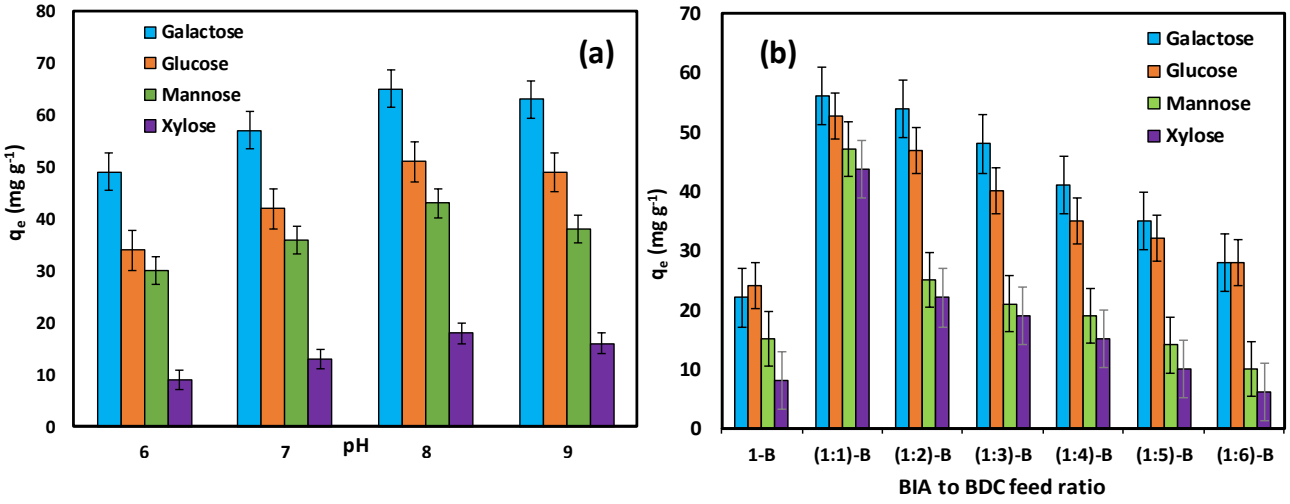

Figure 3.11. *(a)The adsorption efficiency of (1:1)-B at different pH values of cis-diol solutions; (b) The adsorption efficiency of all the MOFs at pH 8 (n=3).*

3.2.5 Adsorption kinetics and equilibrium studies

The data acquired from the adsorption experiments with the MOF **(1:1)-B** is used for the adsorption kinetics and equilibrium studies (Fig. 3.11b) since **(1:1)-B** is superior in adsorbing most of the investigated cis-diols in comparison to the other MOFs. The batch adsorption

experiments gave valuable data regarding both the cis-diol diffusion and the possible interaction with the boronic acid moieties.

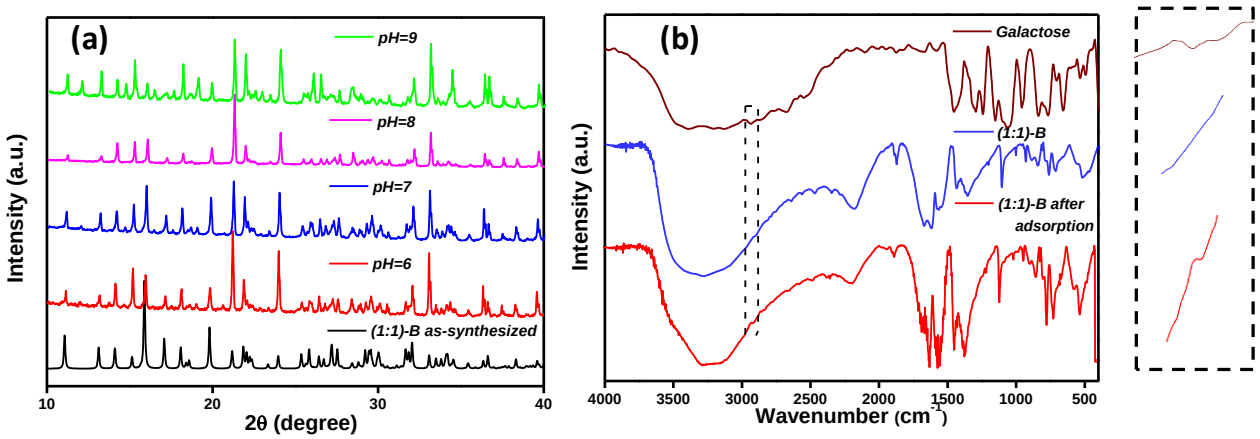

Figure 3.12. *(a) PXRD patterns of* ***(1:1)-B*** *after soaking in water at different pH for 24 h, (b) The IR spectra of* ***(1:1)-B*** *before and after the adsorption study with galactose; zoomed image of the marked area showing the peak corresponding to C-H bonds of galactose.*

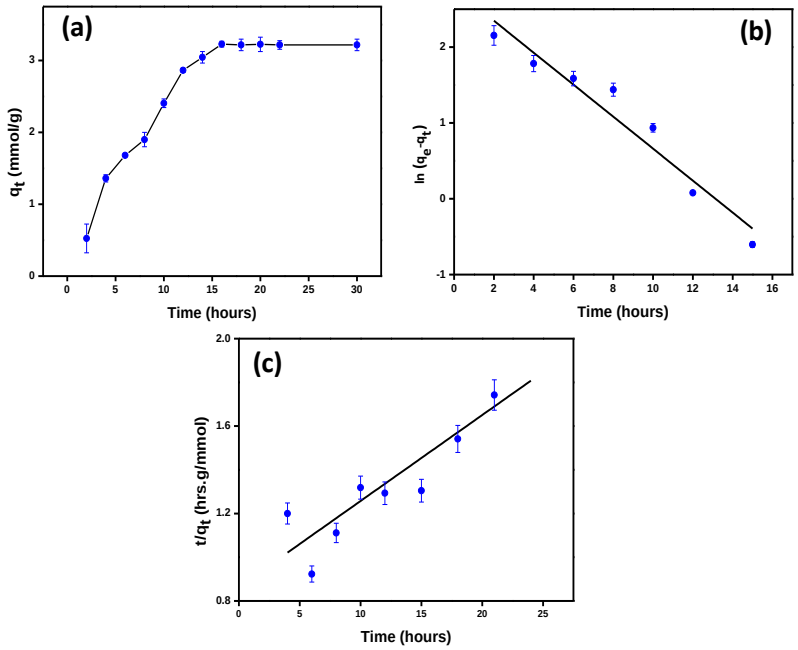

Figure 3.13. *(a) The adsorption of galactose on* ***(1:1)-B****; (b) pseudo-first- order and (c) pseudo-second-order kinetic models.*

Table 3.4. *Kinetic constants for the removal of galactose by (1:1)-B. (C_0 = 200 mg L^{-1}; pH = 8; T = 30 °C).*

Pseudo-first-order		
$K_1(min^{-1})$	**q_e (mg/g)**	**R^2**
0.22	15.95	0.92
Pseudo-second-order		
$K_2(gmg^{-1}min^{-1})$	**q_e (mg/g)**	**R^2**
0.0018	45.45	0.95

Figure 3.13 illustrates the effect of adsorption time for the galactose adsorption to the MOF **(1:1)-B**. The rate of adsorption was notable at first, in the following hours the rate decreased, finally reaching equilibrium. 56 mg of galactose per gram of the MOF is the maximum adsorption calculated. Two most common kinetic models- pseudo-first-order and pseudo-second-order- are used for deriving the adsorption mechanism. The correlation coefficient (R^2) depicts the agreement between the experimental facts and the values predicted by the models. The linearized forms of pseudo-first-order and pseudo-second-order models is presented in figure 3.13. The calculated adsorption parameters are given in table 3.4. The correlation coefficient obtained proves that the pseudo-second-order model better explains the adsorption. It also revealed possible chemical interaction in the adsorption process of cis-diols to the MOFs. As for the pseudo-first-order model, the calculated linear regression coefficient was low and the q_e value was not in agreement with the experimentally derived quantity. But in the case of pseudo-second-order model, the computed values of R^2 and q_e was comparable to that obtained through adsorption experiments.

For specifying the possible interaction between the adsorbent (MOFs) and the adsorbates (cis-diols) adsorption isotherm models are significant, which might shed light on the mechanism followed (Fig. 3.14). The linear regression (R^2) coefficient obtained from the

Langmuir and Freundlich adsorption models helps in predicting a better fitting model among them. The calculated adsorption parameters and regression coefficients are listed in table 3.5. Considering the values of maximum adsorption capacity (q_{max}) and correlation coefficient (R^2), the Langmuir isotherm model better explains the adsorption process. The homogeneous nature of the adsorbent surface is another finding. The plots of $\frac{C_e}{q_e} vs. C_e$ exhibit linearity in the whole concentration range, for the Langmuir model,.

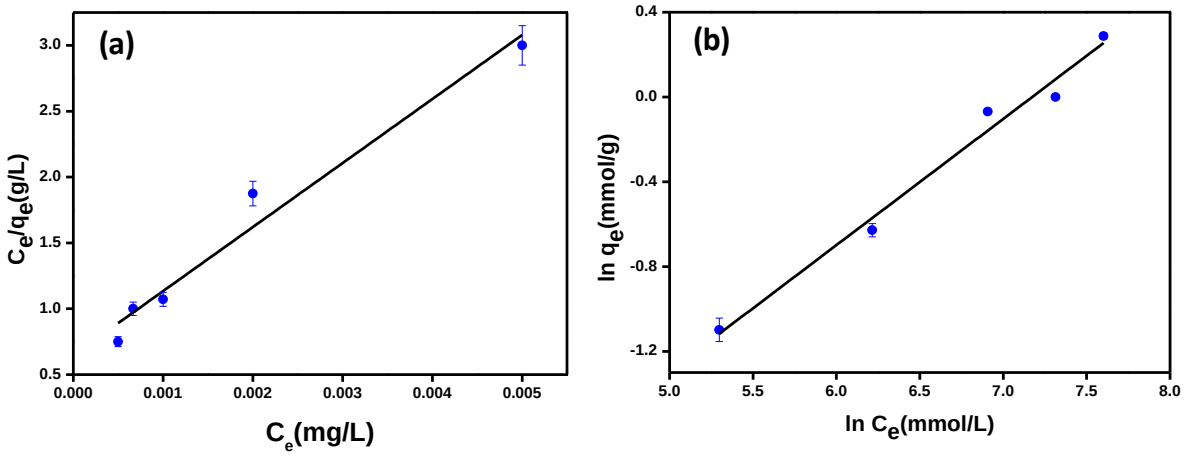

Figure 3.14. *(a) The Langmuir and (b) Freundlich adsorption models.*

Table 3.5. *Langmuir and Freundlich isotherm constants for the adsorption of galactose by (1:1)-B.*

Langmuir model		
K_L ***(L/mg)***	q_{max} ***(mg/g)***	R^2
75.012	*27.03*	*0.98*
Freundlich model		
K_F ***(L/mg)***	q_{max} ***(mg/g)***	R^2
18.54	*14.73*	*0.96*

3.2.6 Adsorption mechanism

A resultant framework with the uniform distribution of boronic acid groups resulted when a part of BIA got replaced by a calculated number of BTC. These free-standing moieties are resulting in a five-membered cyclic ester by binding to the hydroxyl groups of diols.[122] The adsorption efficiency is greatly influenced by the pH of the cis-diol solution. Mohapatra et al. state that the rate-determining step in the diol binding is the formation of a tetrahedral intermediate, which occurs at a pH value near to the pK_a value of the phenylboronic acid, to be precise when pH is in between the pK_a of the glycolic acid and phenylboronic acid.[123] The likelihood of the boron atom in the boronic acid fragment to exist preferably in the tetrahedral form to the trigonal form, leading to the stronger interaction with the monosaccharides in slightly alkaline conditions is explained by Lu et al.[124],[125] The pH-dependent study demonstrated the direct relationship between the rate of adsorption and the pH. Similarly, the isomeric structure of the cis-diols in the aqueous solution plays a prominent role in determining the likelihood and extent of adsorption. The boronic acid moiety has a higher affinity to bind with the furanose form and the pyranose and furanose isomeric forms of cis-diols exist in equilibrium in the solution.[126] So by theory, the cis-diol with the highest percentage of furanose form in the aqueous solution must be significantly adsorbed by the boronic acid embedded MOFs. Galactose is identified to be present in greater percentage (~7 %) in its furanose isomer in the aqueous solutions compared to the other cis-diol candidates. Experimentally it is proved that galactose binds well with the boronic acid groups and is the better adsorbate among the other cis-diols.[127–129] Almost 1 % of the molecules of other cis-diols (glucose, mannose, and xylose) are in the furanose form with slight differences.[129] The adsorption efficiency obtained by experimental results follows a

similar trend with galactose acts as the better adsorbate followed by glucose, mannose, and xylose.

3.3 Conclusions

Through an MLFC approach, a family of identical structured MOFs are derived from a parent MOF scaffold by adding varying amounts of the boronic acid-containing modulator. By exploiting the affinity of the boronic acid groups to bind to the cis-diols, the boronic acid moieties in the MOF scaffold is utilized for the adsorptive removal of cis-diols from their aqueous solutions. The presence of boronic acid groups in the MOF skeleton is confirmed by XPS and ^{11}B NMR analysis. The amount of embedded free boronic acid groups in the framework is directly proportional to the percentage of feed of the 5-BIA ligand. The adsorption experiments were carried out with the parent Ba-MOF, and the boronic acid suspended daughter MOFs. The adsorption efficiency was calculated from the experimental data and compared concerning the amount of boronic acid moieties in the MOF and the isomeric structure of cis-diol. The better adsorbent was found to be (1:1)-B with the highest ration of boronic acid groups in it, and the analyte removal followed the order galactose > glucose > mannose > xylose. The trend in cis-diol adsorption was in accordance with the percentage of furanose isomer present in the aqueous medium. The adsorption kinetics is of pseudo-second-order nature, and the process follows Langmuir adsorption isotherm.

3.4 Experimental section

3.4.1 Materials

All the chemicals were commercially available and used as obtained without further purification. $Ba(NO_3)_2$, trimesic acid (BTC), galactose, glucose, mannose, and xylose were

purchased from Sigma-Aldrich, and 5-Borono isophthalic acid was purchased from Nanjing Norris Pharm Technology Co. Ltd., China.

3.4.2 Methods of Characterization and Instrumentations

Instrumentations

Powder X-ray diffraction (PXRD) spectra were collected with an X'pert PRO (PANalytics) powder diffractometer equipped with CuKα radiation (1.5405 Å). An AVANCE II-500 (Bruker) NMR spectrometer is used for ^{11}B nuclear magnetic resonance (^{11}B NMR) analyses to calculate the amount of BIA ligand incorporated in each MOF. In short, 25 mg of each MOF sample was digested in a mixture of NaOD and D_2O. The supernatant was transferred to a quartz NMR tube(B < 0.01 ppm) with a known quantity of internal standard $NaBF_4$. The peak obtained from $NaBF_4$ was utilized to calculate the instilled BIA accurately.

To determine particle size and morphology of the MOFs, FEI NOVA NANOSEM 450 scanning electron microscope (SEM) with acceleration voltage 15 kV was used. The samples for the analysis were prepared by drop-casting a minute amount of MOF suspension in water to a silica grid and subsequently drying under vacuum for 24 h. TecnaiG2 TF20S Twin transmission electron microscope (TEM, 300 kV) was used to record the TEM high-resolution images. TEM–EDX mapping was also performed for clearly mapping the distribution of elements of interest like boron, barium, carbon, and oxygen in the MOF crystal. An FT-IR prestige-21 (Shimadzu) spectrometer is used for the fourier-transform infrared (FT-IR) spectral data collection using KBr pellets in the range of 4000-400 cm^{-1}. An SDT Q600 (Shimadzu) analyzer is used for performing thermogravimetric analyses (TGA) in a flowing nitrogen atmosphere with a heating rate of 10 ℃ per minute. The nitrogen adsorption-desorption studies were carried out using a Micromeritics 3 Flex automatic volumetric adsorption instrument at 77 K, and the surface area was calculated using the

Brunauer-Emmett-Teller (BET) method. The degassing was carried out at 100 °C for 12 h. X-ray photoelectron spectra (XPS) is collected using the omicron instrument and analyzed with the casa XPS software. The binding energy and composition of the samples were analyzed using the obtained data. The adsorption studies were carried out using HPLC (LC-2030, Shimadzu, Japan) fitted with an RI detector (RID 20A, Shimadzu, Japan). Phenomenex RCM-Monosaccharide columns were used for the analysis. The cis-diol samples were filtered through 0.2-micron filters and injected directly to the column with an auto-injector. The mobile phase used was deionized water with a flow rate of 0.6 ml/min. The column temperature was maintained at 85 °C. The calibration standards were glucose, xylose, galactose, mannose and arabinose (Sigma–Aldrich, India).

Synthesis

Synthesis of 1-B: The reagents $Ba(NO_3)_2$ (0.2 mmol) and 1,3,5-benzene tricarboxylic acid (BTC, 0.2 mmol) were dissolved by sonication in a 10 mL water - N, N'-Dimethylformamide (DMF) mixture (1:1) in a glass vial. The solution was transferred entirely to a Teflon lined autoclave (20 mL) and placed in an oven preheated to 120 °C and kept for 24 h. The autoclave was cooled to room temperature, and the white crystals obtained were washed three times with fresh DMF. The crystals were dried in air and powdered for further use.

Synthesis of (1:1)-B – (1:6)-B: The procedure followed was same as that for the synthesis of 1-B except that a mixture of BTC and 5-Boronoisopthalic acid (BIA) were used in place of BTC alone. The family of six MOFs contain different ratios of the two ligands ((x:y) is the ratio of BIA to BTC).

Adsorption of cis-diols by the activated MOFs: The activation of the MOF samples was carried out by heating at 100 °C for 12 h under vacuum, for the removal of solvent molecules trapped inside the pores. The activated MOF samples were kept in a well-maintained

desiccator before the adsorption tests. The adsorption of a group of cis-diols (like Glucose, Galactose, Xylose, and Mannose) from their aqueous solutions was carried out by the as-synthesized and activated MOFs (**1-B** and **(1:1)-B** to **(1:6)-B**). Stock solutions (concentration of 2 gL^{-1}) of the cis-diols galactose, glucose, mannose, and xylose were prepared in distilled water and stored in a cool and dry place. All the working solutions were obtained by further diluting the stock solutions with distilled water. The pH of the test solution was adjusted to the preferred value using minute quantities of 0.1 M NaOH or 0.1 M HCl aqueous solutions.

Adsorption kinetic studies. The adsorption studies were carried out at room temperature (34°C). Cis-diol solutions of an initial concentration of 200 mg/L (50 mL) was taken in 250 mL Erlenmeyer flasks, and the pH was adjusted to 8 with 0.1 M NaOH. The activated MOF (50 mg) was added, and the suspensions were kept for shaking at 100 rpm in an automatic orbital shaker. At certain time intervals, aliquots were withdrawn, and the clear solution was collected by centrifugation (10000 rpm for 10 minutes) followed by filtration through a 0.22 µm syringe filter to remove any small residues of MOF. The cis-diol concentration was measured by HPLC with a refractive index detector and was quantified by plotting a standard calibration curve. The extent of cis-diol adsorption to the MOF at any given time was computed using the initial concentration and concentration obtained at that time.

Adsorption equilibrium studies. The cis-diol solutions (50 mL) of varying concentrations maintained at pH eight were utilized with an adsorbent dose of 1 g/L, for the adsorption isotherm studies. The agitation was allowed to continue for 24 h, and resultant cis-diol solutions were collected after centrifugation and filtration through a syringe filter of pore size 0.22 µm before the HPLC analysis. The adsorption capacity (q_e) of the MOFs was calculated from the initial (C_i) and final (C_e) cis-diols concentrations per gram of the adsorbent.

All the experiments were repeated for at least three times under similar conditions to check the variability in results. The analysis was carried out by varying the conditions like pH of the working solution, time of adsorption and the amount of MOFs to optimize the best condition. For all the adsorption results, the experimental error was calculated to be less than 5 %.

Chapter 4

Zn-based Microporous MOF as SPME Coating for the Analysis of PAHs at Trace Levels

Abstract

Novel zinc-based MOF(PUM-210) is introduced as an SPME (solid-phase microextraction) fibre coating with high affinity and extraction efficiency towards the 16 different PAHs from their aqueous solutions. The analysis and subsequent quantitation are accurately carried out with the help gas chromatography-mass spectrometry. The multicriteria method of the desirability functions allowed finding the best conditions for the simultaneous extraction of PAHs. The best conditions for the simultaneous extraction of the sixteen analytes were found to be an extraction temperature of 30 °C and an extraction time of 30 min. Moreover, the MOF-coated fibre is highly selective towards PAHs compared to the competing compounds like BTEX (benzene, toluene, ethylbenzene and xylenes). The steric hindrance, hydrophobicity and π-π interactions play a critical role in the analyte selection and inclusion. At last sixty-nine, underground water samples collected during a monitoring campaign (in 2018 from south Italy region) is analysed using the MOF-coated fibres.

4.1 Introduction

Anthropogenic activities related to industries, transportation, synthesis of goods and so on are the major contributor to water pollution. Polycyclic aromatic hydrocarbons (PAHs) are potential pollutants expelled to the environment through several biological and human activities like volcano eruption, oil spillage and crop burning. The concentration of PAHs beyond a limited range leads to the formation of photochemical smog and contamination of groundwater. [130] Exposure to such an environment for a prolonged period may damage the vital body organs like the kidney and central nervous system. Sixteen of the PAHs have been included in the US EPA (Environmental Protection Agency) priority pollutant list due to their mutagenic and carcinogenic effects.[131] Although PAHs are hydrophobic, PAHs deriving from runoff in urban areas or wastewater from industries can contaminate water bodies, mostly groundwater. Hence it is highly essential to remove these compounds from the environment. Since the concentrations of PAHs are deficient, the monitoring and extraction demand highly sensitive and sophisticated methods or instruments. The one-step sample concentration and analysis offered by the solid-phase microextraction (SPME) [132] technique is worth noting in this regard. SPME is a handy and accurate method for the study of a spectrum of environmental analytes in short time with minor errors. The SPME fibres can be coated with effective adsorbents as a stationary phase to improve its efficiency and hence applicability.[133–135]

Metal-organic frameworks (MOFs) are organic-inorganic hybrid polymers with exceptional properties like porosity, high thermal and mechanical stability. The porous nature of the framework helps to admit bigger analytes like PAHs into the structure. [136–140] Moreover, aromatic ligands in the MOF frameworks provide a possibility of π-π interaction with the aromatic analytes. Recently metal-organic frameworks (MOFs) emerged as a new class of coating materials for the SPME fibres [35,141–143].

Pelagatti *et al*. have synthesized a novel Zn-based triple catenated MOF(PUM-210) in the year 2018.[144] The mixed-ligand MOF, PUM-210 is constructed under solvothermal condition by combining the ligands 2,6-naphthalene dicarboxylic acid (NDC), pyridine-functionalized biphenylene ligand (bpba) with the metal salt $Zn(NO_3)_2 \cdot 6H_2O$. PUM-210 has a thermally robust microporous scaffold with aromatic ligands which makes it slightly hydrophobic and is moisture tolerant to a certain extent which is rare for Zn-based MOFs.[144]Additionally, the aromatic ligands in the framework were expected to promote interactions with aromatic analytes.

Here, PUM-210 is proposed as a novel SPME coating for the detection of PAHs in an aqueous medium. [145,146] According to our knowledge, PUM-210 is the first mixed-ligand MOF used as an SPME coating material to date. The analysis of PAH solutions is carried out under the SIM (Selected Ion Monitoring) mode with a gas chromatography-mass spectrometry (GC-MS) instrument. The performance of MOF-coated fibers is compared with that of commercially available SPME fibers. Both sensitivity and signal stability with the MOF-coated fibre suggest the same as a competitive candidate for the analysis of PAHs at trace levels. Finally, they are applied to investigate the PAHs in the underground water samples obtained from the neighbourhoods of oil industries.

4.2 Results and Discussion

4.2.1 Characterization of the PUM-210 fibre

Several features of PUM-210 like high thermal stability, hydrophobicity and high surface area makes it a right candidate as a coating material for SPME [144]. The PUM-210 scaffold is made of Zn metal in two different geometries and has rectangular microporous channels (Fig. 4.1). This framework has thermal stability up to 380 °C, and it can be well activated by solvent-exchange method followed by a thermal vacuum. Activation step helps in the

removal of the solvent DMF molecules residing inside the micropores, and the BET surface area is calculated to be 491 m^2/g. [144]

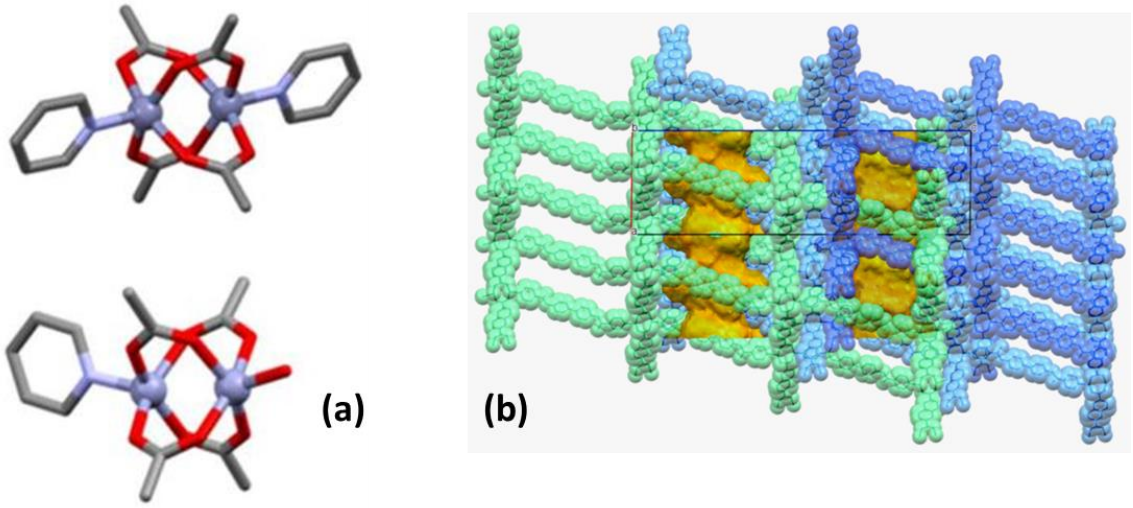

Figure 4.1. *(a) Two metal centers and (b) rectangular microporous channels in PUM-210.*

The rigidity of the framework, even after the activation, is confirmed by Powder X-Ray Diffraction (PXRD) analysis.[144] Hence, PUM-210 is selected as the stationary phase coating material for SPME fibre. The morphology and the thickness of the MOF coating are analyzed by SEM images of the SPME fibre before and after MOF coating (Fig. 4.2). There is a uniform distribution of the MOF over the silica fibre with an average thickness of 71.6 (± 4.2) μm (n = 5).

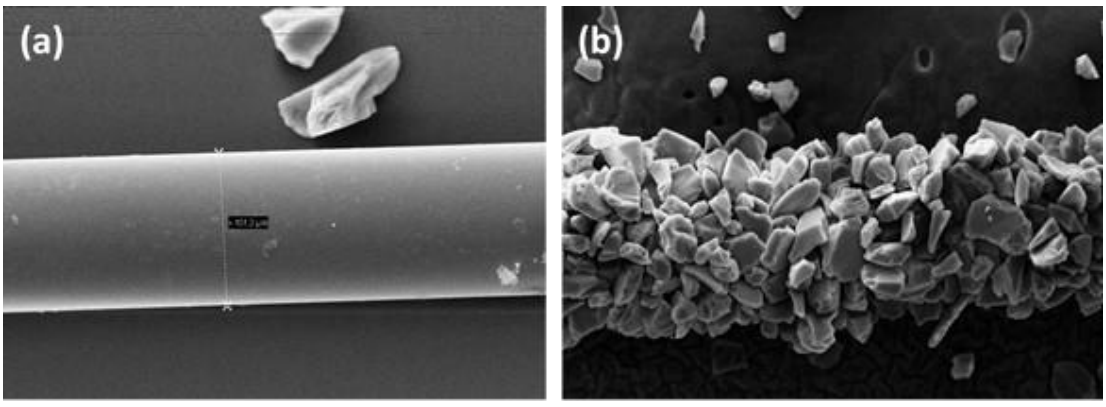

Figure 4.2. *SPME silica fibre (a)before and (b) after coating with PUM-210.*

The fibre is conditioned in the GC injector port at 270 °C to evaluate the thermal capabilities of the coatings, and it was observed that no significant bleeding occurred which further confirmed the high thermal stability of the MOF coating.

The fibre-to-fibre (by preparing different fibres using the same batch of MOF powder) and batch-to-batch (by preparing the fibres using MOF powders deriving from different synthetic batches) repeatability is evaluated to know the performance of the MOF fibre coating. The model compounds used were Ace and BaP at a concentration of 60 ng/L. The experiments are repeated using five fibres, and by performing three replicate measurements for each fibre, RSDs % lower than 9 % was always obtained. Therefore, MOF is assessed as a feasible coating for SPME for the analysis of PAHs.

4.2.2 SPME optimization

The extraction efficiency towards the PAHs, which might be present in minute quantity in the environmental samples, especially in the groundwater, is improved by following the optimization conditions of analysis. The extraction conditions evaluated were the extraction temperature (T) and extraction time (t). The operative and instrumental limits were taken in to account for fixing the experimental domain. For instance, temperature values lower than 30 °C could not be maintained for a long time, while temperature values higher than 60 °C could lead to the desorption of the most volatile compounds from the coating. To avoid long analysis times, the extraction time values higher than 30 minutes were not considered. The principal and interaction effects were calculated for each compound. Table 4.1 presents the regression models and the corresponding single desirability values (d) measured for each PAH. The highest global response within the provided experimental domain is assessed from the regression models.

Table 4.1. *Regression models calculated for each analyte.*

PAHs	*Regression models*
Nap	$y = 340(\pm 20) - 150(\pm 20)T + 80(\pm 30)T^2$
Acy	$y = 630(\pm 50) - 280(\pm 50)T + 160(\pm 60)T^2$
Ace	$y = 760(\pm 40) - 180(\pm 50)T$
Flu	$y = 970(\pm 40) - 270(\pm 60)T - 160(\pm 80)Tt$
Ph	$y = 2060(\pm 100) + 420(\pm 130)t - 340(\pm 160)Tt$
An	$y = 1570(\pm 80) + 310(\pm 110)t - 330(\pm 140)Tt$
Flt	$y = 1920(\pm 80) + 230(\pm 110)T + 640(\pm 110)t$
Py	$y = 1890(\pm 70) + 230(\pm 110)T + 630(\pm 110)t$
BaA	$y = 1850(\pm 160) + 740(\pm 230)t$
Chry	$y = 1780(\pm 130) + 660(\pm 190)t$
BbF	$y = 2140(\pm 590) + 1390(\pm 840)t^2$
BkF	$y = 1910(\pm 370) + 920(\pm 370)t + 1310(\pm 520)t^2$
BaP	$y = 1690(\pm 430) + 820(\pm 430)t + 1360(\pm 610)t^2$
InPy	$y = 2470(\pm 890) + 2960(\pm 1260)t^2$
DiahA	$y = 1590(\pm 520) + 1700(\pm 730)t^2$
BghiP	$y = 2240(\pm 800) + 2600(\pm 1140)t^2$

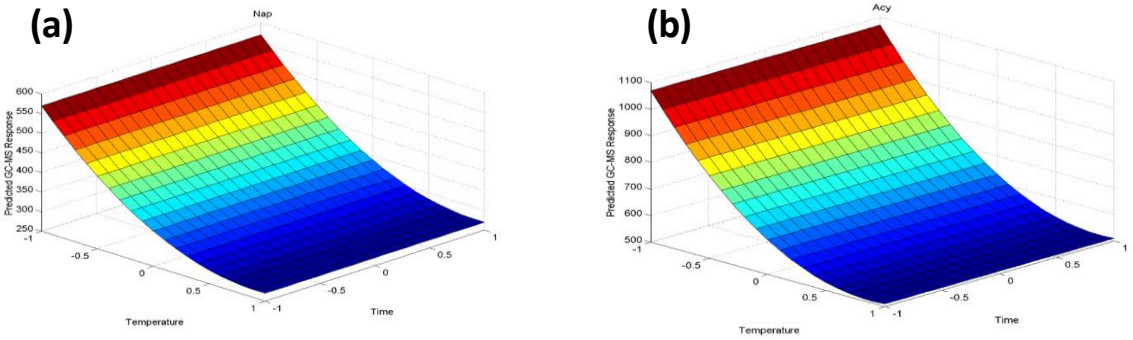

Figure 4.3. *Response surfaces of the analytes naphthalene (left) and acenaphthylene (right).*

Response surfaces are reported in figure 4.3. Global desirability was evaluated in correspondence to the extraction temperature of 30 °C and an extraction time of 30 min as D = 0.89. The results show that high-temperature values result in lower GC responses for the

most volatile PAHs. In contrast, there is a significant contribution of extraction time on heavy compounds, thus suggesting long analysis times for their better adsorption.

4.2.3 Selectivity studies

The aqueous samples with the 16 PAHs at 60 ng/L and BTEX (benzene, toluene, ethylbenzene and o-, m-, p-xylenes) at 30 and 60 µg/L concentration levels were analyzed, taking into account the possible host-guest interactions (specifically π-π interactions) between the aromatic analyte molecules and the aromatic ligands in the MOF structure. There were only negligible differences ($p > 0.05$) found between the mean responses of the PAHs using the PUM-210 coated fibre thus confirming that PAH adsorption could be feasible even in the presence of high concentration levels of BTEX, which are potentially competing compounds. Furthermore, the hydrophobicity of the structure of PUM-210 and the one-dimensional channels in them could play a critical role in determining the adsorption capabilities of MOF. Moreover, the matching dimensionality between the microporous structure and PAHs can improve the extraction capability of

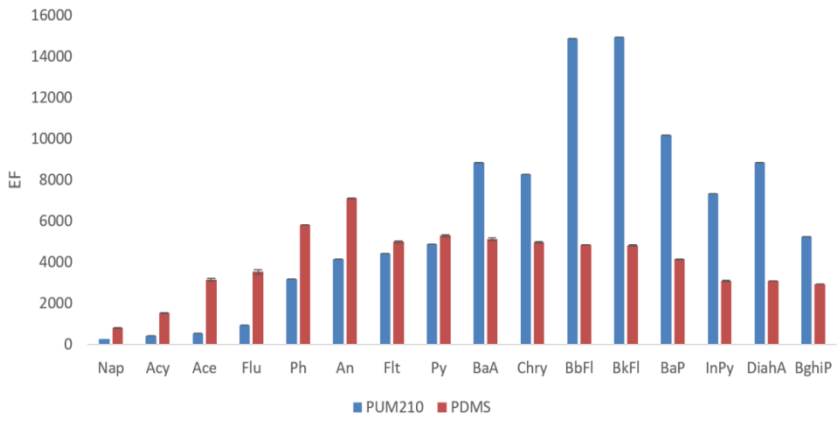

Figure 4.4. *Enhancement factors of all the analytes on MOF and the PDMS fibre.*

SPME coating towards PAHs. BTEX compounds are not retained very well by the MOF because of their smaller size. Hence, BTEX can easily travel in and out of the pores of PUM-210 scaffold [144], but the guests of bigger size, such as PAHs are blocked instead,

In conclusion, we have investigated the enrichment capabilities of the MOF coating in terms of enhancement factors (EFs).[147] It is the ratio of the concentration of each PAH in the SPME fibre after extraction to that of the PAH in the sample (i.e. using the ratio of the area under the chromatographic peak of each analyte after extraction with SPME fibre to that before extraction obtained by the direct injection of a standard solution, n = 3). Finally, the results are compared to those obtained by using a commercial fibre under the same conditions. Figure 4.4 reports the EFs in the range 300 (±5) – 14950 (±150). Here as well PUM-210 showed a better extraction capability towards the heaviest PAHs, with EFs about two to three-fold higher than those achieved using the commercial PDMS 30 µm fibre which is usually used for PAH analysis. Thus, it was verified that steric hindrance has a crucial role in determining the extraction and retainment efficiency.

Table 4.2. *LOD values and calibration curves of the 16 PAHs.*

	LOD (ng/L)				
PAHs	***PUM 210***	***PDMS 30 µm***	$b_0(\pm s_{b_0})$	$b_1(\pm s_{b_1})$	***Range (ng/L)***
Nap	*2.1*	*3.2*	*0.77 (±0.17)*	*0.94 (±0.04)*	*4 – 600*
Acy	*3.6*	*2.4*	-	*1.61 (±0.02)*	*7 – 600*
Ace	*3.7*	*2.6*	-	*1.54 (±0.02)*	*7 – 600*
Flu	*2.0*	*4.2*	-	*1.97 (±0.02)*	*4 – 600*
Ph	*1.5*	*0.9*	*0.36 (±0.11)*	*1.06 (±0.03)*	*3 – 600*
An	*1.6*	*1.5*	-	*1.02 (±0.02)*	*3 – 600*
Flt	*0.9*	*2.7*	-	*1.79 (±0.03)*	*2 – 600*
Py	*0.8*	*1.5*	-	*1.71 (±0.03)*	*2 – 600*
BaA	*1.3*	*3.2*	-	*1.31 (±0.02)*	*3 – 600*
Chry	*1.4*	*2.4*	-	*1.56 (±0.02)*	*3 – 600*
BbF	*0.5*	*2.6*	-	*1.16 (±0.01)*	*1 – 600*
BkF	*1.5*	*3.2*	-	*1.23 (±0.01)*	*2 – 600*
BaP	*1.1*	*2.0*	-	*1.36 (±0.01)*	*2 – 600*
InPy	*1.9*	*2.6*	-	*1.59 (±0.02)*	*4 – 600*
DiahA	*1.8*	*2.4*	-	*1.05 (±0.02)*	*4 – 600*
BghiP	*1.0*	*1.8*	-	*1.30 (±0.02)*	*2 – 600*

Regression equation: $y = b_0 + b_1 \cdot x$

4.2.4 Method validation and real samples analysis

Validation was carried out under the optimized conditions, to meet the acceptance criteria for bioanalytical method validation. The ability of MOF coated fibre for PAH extraction at trace

levels is verified by the LOD values obtained in the ng/L range (Table 4.2). Except for the most volatile components, the control experiments carried out using a PDMS 30 µm fibre exhibited higher values compared to those achieved by the PUM-210 coated fibre for all PAHs. Moreover, no carryover effects were there while using PUM-210 coated fibre. Thus, the MOF coating has several advantages over the commercial fibre, which makes it a better candidate for the PAH extraction. Lastly, it can be perceived that the performances of the achieved limits were consistent with those reported in recent studies [148–152], thus proving the exceptional performances of the novel coating.

By applying Mandel's fitting test, good linearity (Table 4.3) over two orders of magnitude is obtained in the 600 ng/L range (LOQ) for all the PAHs. When experiments were performed along three days, the repeatability and intermediate precision were attained with RSD % lower than 16 % and 22 % at the LOQ level (Tables 4.4 & 4.5). Here, ANOVA on the data acquired along the time did not show substantial differences among the mean values (p > 0.05).

The extraction efficiency of the coated fiber is confirmed by assessing the obtained RR % which is in the range 85 (±5) – 117 (±21) % (n = 10) (Table 4.6). Since the analysis of blank water samples with SPME fibre did not show the presence of interferences, there is said to be a good selectivity. Table 4.7 presents a list of literature following a similar analysis.[150,151,160–169,152,170–173,153–159] As the table depicts, the PUM-210 coated fibre provide comparable or better results compared to the other MOF based SPME coatings for the PAHs. Finally, the MOF coated fibre is used for the analysis of 52 samples collected during various seasons(spring, summer, autumn, and winter) in the year 2018 from the south of Italy near the surroundings of the oil industry to assess the possible contamination of underground water. None of the underground samples has a detectable amount of PAHs.

4.3 Conclusions

We have used a novel zinc-based mixed-ligand MOF, namely PUM-210 as SPME coatings. The coated fiber is used for the extraction and analysis of environmentally harmful PAHs in the immersion mode. The results were compared with that obtained using commercially available SPME fibers. The aromatic building blocks of PUM-210 provide the possibility for π-π interactions to hold the analytes in the structure. Also, the hydrophobicity of PAHs and the one-dimensional channel in the MOF scaffold acts as critical parameters determining the efficiency. The MOF coated fibre activity is validated by using it for groundwater analysis. The LOD values for PAHs were in the ng/L levels. Moreover, the results were found to comply with the WHO recommendation for PAHs determination in groundwater samples. Each fiber is used for more than 200 analyses without significant change in the extraction efficiency.

Table 4.3. *Calibration curves for each PAH.*

PAHs	$b_0(\pm s_{b_0})$	$b_1(\pm s_{b_1})$	Range (ng/L)
Nap	0.77 (±0.17)	0.94 (±0.04)	4 – 600
Acy	-	1.61 (±0.02)	7 – 600
Ace	-	1.54 (±0.02)	7 – 600
Flu	-	1.97 (±0.02)	4 – 600
Ph	0.36 (±0.11)	1.06 (±0.03)	3 – 600
An	-	1.02 (±0.02)	3 – 600
Flt	-	1.79 (±0.03)	2 – 600
Py	-	1.71 (±0.03)	2 – 600
BaA	-	1.31 (±0.02)	3 – 600
Chry	-	1.56 (±0.02)	3 – 600
BbFl	-	1.16 (±0.01)	1 – 600
BkFl	-	1.23 (±0.01)	2 – 600
BaP	-	1.36 (±0.01)	2 – 600
InPy	-	1.59 (±0.02)	4 – 600
DiahA	-	1.05 (±0.02)	4 – 600
BghiP	-	1.30 (±0.02)	2 – 600

Table 4.4. *Precision (repeatability) of the method for the analysis of PAHs (n = 10).*

Repeatability (RSD%)						
PAHs	**LOQ**	**150 ng/L**	**300 ng/L**	**400 ng/L**	**500 ng/L**	**600 ng/L**
Nap	5.5	2.2	15.1	14.0	4.4	5.5
Acy	1.6	8.2	5.5	5.7	5.8	1.2
Ace	12.8	7.1	7.4	6.5	4.1	2.9
Flu	15.9	7.4	4.5	4.6	3.3	2.2
Ph	11.3	13.1	7.3	4.4	4.9	3.3
An	15.8	18.4	11.8	2.5	5.4	4.7
Flt	16.0	11.1	4.6	2.1	3.9	3.4
Py	5.8	13.3	9.8	3.9	6.1	7.3
BaA	8.7	9.6	6.4	10.3	5.4	4.4
Chry	8.2	7.1	3.6	3.5	4.1	0.8
BbFl	2.3	5.8	6.6	7.9	5.7	2.1
BkFl	3.2	1.9	1.3	0.9	2.0	0.5
BaP	8.3	2.6	2.6	0.3	0.2	1.4
InPy	12.7	10.0	2.9	3.1	2.8	3.2
DiahA	8.3	7.7	11.4	9.5	7.0	4.5
BghiP	12.1	13.1	3.7	9.7	3.3	3.1

Table 4.5. *Intermediate precision of the method for the analysis of PAHs (n = 10).*

Repeatability (RSD%)						
PAHs	**LOQ**	**150 ng/L**	**300 ng/L**	**400 ng/L**	**500 ng/L**	**600 ng/L**
Nap	5.5	2.2	15.1	14.0	4.4	5.5
Acy	1.6	8.2	5.5	5.7	5.8	1.2
Ace	12.8	7.1	7.4	6.5	4.1	2.9
Flu	15.9	7.4	4.5	4.6	3.3	2.2
Ph	11.3	13.1	7.3	4.4	4.9	3.3
An	15.8	18.4	11.8	2.5	5.4	4.7
Flt	16.0	11.1	4.6	2.1	3.9	3.4
Py	5.8	13.3	9.8	3.9	6.1	7.3
BaA	8.7	9.6	6.4	10.3	5.4	4.4
Chry	8.2	7.1	3.6	3.5	4.1	0.8
BbFl	2.3	5.8	6.6	7.9	5.7	2.1
BkFl	3.2	1.9	1.3	0.9	2.0	0.5
BaP	8.3	2.6	2.6	0.3	0.2	1.4
InPy	12.7	10.0	2.9	3.1	2.8	3.2
DiahA	8.3	7.7	11.4	9.5	7.0	4.5
BghiP	12.1	13.1	3.7	9.7	3.3	3.1

Table 4.6. *Recovery Rates (n = 10) of the method for the analysis of PAHs.*

Repeatability (RSD%)						
PAHs	**LOQ**	**150 ng/L**	**300 ng/L**	**400 ng/L**	**500 ng/L**	**600 ng/L**
Nap	5.5	2.2	15.1	14.0	4.4	5.5
Acy	1.6	8.2	5.5	5.7	5.8	1.2
Ace	12.8	7.1	7.4	6.5	4.1	2.9
Flu	15.9	7.4	4.5	4.6	3.3	2.2
Ph	11.3	13.1	7.3	4.4	4.9	3.3
An	15.8	18.4	11.8	2.5	5.4	4.7
Flt	16.0	11.1	4.6	2.1	3.9	3.4
Py	5.8	13.3	9.8	3.9	6.1	7.3
BaA	8.7	9.6	6.4	10.3	5.4	4.4
Chry	8.2	7.1	3.6	3.5	4.1	0.8
BbFl	2.3	5.8	6.6	7.9	5.7	2.1
BkFl	3.2	1.9	1.3	0.9	2.0	0.5
BaP	8.3	2.6	2.6	0.3	0.2	1.4
InPy	12.7	10.0	2.9	3.1	2.8	3.2
DiahA	8.3	7.7	11.4	9.5	7.0	4.5
BghiP	12.1	13.1	3.7	9.7	3.3	3.1

Table 4.7. *LOD values obtained in previous studies compared with those achieved in this work.*

Coating material	***LODs (ng/L)***	***SPME mode***	***Technique***	***Reference***
TMU-6	*5.0 – 8.0*	*HS*	*GC-MS*	[150]
Ni-Zn MOF/g-C_3N_4[a]	*0.10 – 3.0*	*DI*	*GC-MS*	[151]
MIL-101(Cr)	*0.12 – 2.1*	*HS*	*GC-MS*	[152]
UiO-66	*0.28 – 0.60*	*DI*	*GC-MS*	[153]
MIL-53(Al)	*0.10 – 0.73*	*DI*	*GC-MS/MS*	[154]
Bio-MOF-1	*20 – 2300*	*DI*	*GC-FID*	[155]
UiO-66	*10 – 30*	*DI*	*GC-FID*	[174]
MIL-101(Fe)@MON[b]	*0.030 – 0.30*	*HS*	*GC-MS/MS*	[157]
IRMOF-3@ILs[c]/PDMS	*12 – 15*	*HS*	*GC-FID*	[158]
HKUST-1	*0.12 – 9.9*	*HS*	*GC-MS*	[159]
Yb-MOF	*0.070 – 1.7*	*HS*	*GC-MS/MS*	[160]
Cu-BDC@polyimide	*0.11 – 2.1*	*DI*	*GC-MS*	[161]
ZIF-8	*0.30 – 7.8*	*DI*	*GC-MS*	[162]
MAF-66	*0.10 – 7.5*	*HS*	*GC-FID*	[163]

MWCNTs[d]/PoPD[e]	*20 – 90*	*HS*	*GC-FID*	[164]
Cork	*300*	*DI*	*GC-MS*	[165]
PEDOT[f]@AuNPs[g]	*5.0 – 25*	*HS*	*GC-FID*	[166]
g-C_3N_4 derivative	*0.010 – 0.10*	*DI*	*GC-MS*	[167]
LP-OMC[h]	*1.6 – 10*	*DI*	*GC-MS*	[168]
Peanut shell biochar	*1.1 – 2.5*	*HS*	*GC-MS*	[169]
PMO[i]-IL	*4.0 – 9.0*	*HS*	*GC-MS*	[170]
ph-TiO_2NS[j]	*8.0 – 43*	*DI*	*HPLC-UV/vis*	[171]
PoPD-co-PoT[k]	*1.0 – 6.0*	*HS*	*GC-FID*	[172]
IL/POSS[l]	*0.0040 – 0.50*	*DI*	*GC-MS*	[173]
PUM 210	*0.50 – 3.7*	*DI*	*GC-MS*	*this work*

[a]graphitic carbon nitride, [b]microporous organic framework, [c]ionic liquids, [d]multi-walled carbon nanotubes, [e]poly-ortho-phenylenediamine, [f]poly(3,4-ethylene dioxythiophene), [g]gold nanoparticles, [h]large pore-ordered mesoporous carbon, [i]periodic mesoporous organosilica, [j]titanium oxide nanosheets, [k]poly-*o*-toluidine, [l]polyhedral oligomeric silsesquioxane

4.4 Experimental section

4.4.1 Materials

$Zn(NO_3)_2 \cdot 6H_2O$ (> 99 % purity), 2,6-naphthalene dicarboxylic acid (NDC, 95 % purity), N, N′-dimethylformammide (DMF, 99.8 % purity), hydrofluoric acid (HF, ≥ 48 % inH_2O), benzene, toluene, ethyl benzene, o-xylene, m-xylene and p-xylene (> 99 % purity), acetone, methanol and methylene chloride (≥ 99.9 % purity), EPA 525 PAH Mix A with the PAHs acenaphthylene (Acy), fluorene (Flu), phenanthrene (Ph), anthracene (An), pyrene (Py), benzo[a]anthracene (BaA), chrysene (Chry), benzo[b]fluoranthene (BbF), benzo[k]fluoranthene (BkF), benzo[a]pyrene (BaP), indeno[1,2,3-c,d]pyrene (IPy), dibenzo[a,h]anthracene (DiahA), benzo[g,h,i]perylene (BghiP) (500 µg/mL each component in dichloromethane), naphthalene (Nap, 99 % purity), acenaphthene (Ace, 99 % purity), fluoranthene (Flt, 98 % purity), and perdeuterated PAHs used as internal standards:

naphthalene-d_8 (Nap-d_8, > 99 % atom D), acenaphthene-d_{10} (Ace-d_{10}, > 99 % atom D), phenanthrene-d_{10} (Ph-d_{10}, > 98 % atom D), pyrene-d_{10} (Py-d_{10}, > 98 % atom D), benzo[a]anthracene-d_{12} (BaA-d_{12}, > 98 % atom D), benzo[a]pyrene-d_{12} (BaP-d_{12}, > 98 % atom D), benzo[g,h,i]perylene-d_{12} (BghiP-d_{12}, > 98 % atom D) were purchased from Sigma-Aldrich (Milan, Italy). Bare fused silica fibers and SPME PDMS 30 μm fibers were from Supelco (Merck, Milan, Italy), whereas the Duralco 4460 epoxy glue was provided by Cotronics Corp. (Brooklyn, NY, USA).

4.4.2 Methods of Characterization

4.4.2.1 Preparation of SPME coatings

MOF synthesis

The PUM-210 synthesis was carried out under solvothermal synthesis following the reported procedure.[183] In short, $Zn(NO_3)_2 \cdot 6H_2O$ (0.4 mmol, 120 mg), NDC (0.4 mmol, 86 mg) and N,N'-(1,1'-biphenyl)-4,4'-diylbis-4-pyridine carboxamide (bpba, 0.2 mmol, 80 mg) were mixed with 41 mL DMF in a 70 mL reaction glass vial. The vial was sealed and sonicated for some time to obtain a uniform solution. The vial was kept at 80˚C in a preheated oven for five days and is cooled to room temperature. The yellow crystals of PUM-210 ($[Zn_4(bpba)_{1.5}(ndc)_4(H_2O)]_n$) were collected and washed with 10 mL DMF for a minimum of three times. The MOF crystals were activated by a solvent exchange method by soaking the crystals in acetone followed by dichloromethane for few days. The solvent is refreshed at certain time intervals with the occasional swirling of the crystals. At last, the crystals were decanted and heated at 100 ℃ under vacuum for 12 hours.

Fiber preparation and characterization

The SPME fibers (fused silica fibers) of 1 cm length were dipped in the hydrofluoric acid solution (40 % *v/v*) for 10 s by subsequent washing with Milli-Q water. The dried fiber is vertically dipped to a vial with Duralco 4460 epoxy glue and, after 2 min, into the vial with 100 mg of finely powdered PUM-210. The process is repeated three times. Likewise, five fibers were prepared and are tested for both fiber-to-fiber and batch-to-batch repeatability. Three replicated measurements were carried out always.

Coating thickness and surface morphology were investigated by the scanning electron microscopy (SEM) using Leica 430 i instrument (Leica, Solms, Germany). Fiber bleeding was evaluated by desorbing the fibers in the GC injection port at 270 ℃ for 2 min.

All the fibers were conditioned in the GC injection port at 310 °C for 2 h under helium flow before analysis. The PXRD pattern of the coating material was directly collected with the coated fiber was placed over a sample holder suitable for transmission geometry. A Rigaku Smart Lab XE diffractometer equipped with a CBO parabolic mirror (parallel beam, CuKα) and a solid-state 2D HyPix3000 detector was used for the analysis. The sample was aligned against the beam position (vertical direction) since it was not in the standard position. Beam size was restricted vertically to 0.5 mm to limit X-ray scattering and horizontally to 10 mm to collect data only from the tip, avoiding diffraction from the fiber support.

4.4.2.2 Optimization of the SPME procedure

The influence of extraction temperature and extraction time are investigated by following a central composite face-centered design (CCF). Standard solutions of all PAHs with a concentration of 25 ng/L were used for this purpose. The experimental range for extraction temperature and extraction time was set as 30 – 60 °C and 10 – 30 min, respectively. Four replicates measurements are performed at the center of the experimental domain to evaluate the experimental error. To evaluate the presence of relevant quadratic effects, an *F*-test

comparing the experimental and calculated responses at the center of the experimental domain was used.

The evaluation of the significant effects and their interactions are studied using the statistical package SPSS Statistics v.23.0 (IBM, Milan, Italy). By a backward search stepwise variable algorithm, the best regression models were obtained. Lastly, the optimal extraction conditions were analyzed by using the multicriteria method of the desirability functions [175,176].

4.4.2.3 SPME analysis

A PAL COMBI-xt autosampler (CTC Analytics AG, Zwingen, Switzerland) is used for the PAH analyses operated in the immersion mode using 9.5 mL of sample in 10 mL glass vials. PAHs and perdeuterated PAHs were used as internal standards at the concentration of 10 and 30 ng/L, respectively. After incubation for 5 min at 30 °C, the extraction was carried out by operating under the optimized conditions. That is an extraction temperature of 30 °C and an extraction time of 30 min. Finally, compounds adsorbed on the fibers were desorbed in the GC injector port for 2 min at 270 °C.

4.4.2.4 GC-MS (SIM) analysis

An HP 6890 Series Plus (Agilent Technologies, Milan, Italy) gas chromatograph coupled to an MSD 5937 (Agilent Technologies) mass spectrometer equipped with an electron ionization ion source (EI-MS) is used for the GC-MS single ion monitoring (SIM) studies.

A Rxi-17Sil MS capillary column (30 m × 0.25 mm i.d., 0.25 μm film thickness; Restek, Bellafonte, USA) with the following temperature program: 110 °C, 15 °C/min to 220 °C, 4 °C/min to 320 °C, hold for 5 min- is used for the chromatographic separation. The carrier gas was Helium with a constant flow rate of 1.0 mL/min. The GC injector was held at 270 °C, and the injection was carried out in splitless mode. The transfer line and ion source were maintained at the temperatures of 280 and 150 °C, respectively. Primarily, a full scan analysis

was performed to choose the proper ions for Time Scheduled Monitoring mode (Table 4.8). Mass spectra were acquired under the following conditions: ionization energy: 70 eV; electron multiplier voltage: 2471 V; dwell time: 30 ms; solvent delay: 2.00 min. Signal acquisition and data handling were performed using the HP Chemstation (Agilent Technologies).

Table 4.8. *Time windows and m/z ratios of the fragment ion values monitored in the study.*

PAHs	***Time window (min)***	***m/z values***
Nap, Nap-d_8	*2.00 – 5.00*	*128, 136*
Acy, Ace, Flu, Ace-d_{10}	*5.00 – 8.50*	*152, 153, 166, 162*
Ph, An, Ph-d_{10}	*8.50 – 11.00*	*178, 188*
Flt, Py, Py-d_{10}	*11.00 – 17.00*	*202, 212*
BaA, Chry, BaA-d_{12}	*17.00 – 22.00*	*228, 240*
BbF, BkF, BaP, BaP-d_{12}	*22.00 – 30.00*	*252, 264*
InPy, DiahA, BghiP, BghiP-d_{12}	*30.00 – 37.33*	*276, 278, 288*

4.4.2.5 Method validation and real sample analysis

EURACHEM guidelines under the optimized conditions are followed for the validation of the SPME-GC-MS (SIM) methods. [177] The uncontaminated water is used as a blank matrix. Briefly, to calculate detection (yD) and quantitation (yQ) limits, ten replicate measurements of the blank matrix were used which are expressed as signals in terms of mean blank (xb) and corrected standard deviation of blank responses (s_0') as follows:

$$yD = xb + 3\ s_0' \quad \cdots\cdots\cdots \quad (4.1)$$

$$yQ = xb + 10\ s_0' \cdots\cdots\cdots (4.2)$$

where s_0' is calculated as $s_0/\sqrt{n}$ using both the standard deviation of the blank responses (s_0) and the number of replicate observations (n) averaged when reporting results.

Limits of detection (LODs) and limits of quantitation (LOQs) were obtained by projection of the corresponding yD and yQ through a calibration plot y = f(x) onto the concentration axis.

Calibration curves (six concentration levels, three replicated measurements for each level) were evaluated in the LOQ – 600 ng/L range for each analyte: lack-of-fit and Mandel's fitting tests were performed to assess the goodness of fit and linearity, whereas a student *t*-test is run to establish the significance of the intercept (significance level 5 %). Repeatability and intermediate precision were calculated in terms of RSD % on the same concentration levels used for the calibration by performing six replicate measurements. Intermediate precision was estimated over three days verifying homoscedasticity of data and performing the analysis of variance (ANOVA) at the confidence level of 95 %.

Accuracy was calculated in terms of recovery rate (RR %) as follows:

$$RR\ \% = c_1/c_2 \cdot 100 \cdots\cdots\cdots (4.3)$$

where c_1 is the measured concentration, and c_2 is the concentration calculated from the amount of PAH spiked into the sample. Recovery rate values were assessed by performing ten replicated measurements *per* level at the LOQ, at 450 and 600 ng/L. Selectivity was evaluated by analyzing blank water samples and testing the absence of interferences. Finally, fifty-two underground water samples collected during a monitoring campaign (the year 2018) in the South of Italy were analyzed.

Chapter 5

Thiol Decorated Defective MOF Embedded with Pd Nanoparticles for Efficient Cr (VI) Reduction

Abstract

Water decontamination from pollutants of different origin requires the involvement of numerous smart materials. Besides the challenges, the metal-organic frameworks (MOFs) and nanoparticles play a significant role in it. In this context, we have developed a thiol-functionalized, defective MOF by a metal-ligand-fragment-coassembly (MLFC) approach and embedded it with uniform-sized palladium nanoparticles (3-6 nm). The material acts as an efficient and recyclable catalyst for the complete reduction of the toxic hexavalent chromium Cr(VI)) to Cr(III) within a short period. Besides, the catalysis occurs under visible light at room temperature with a very minute quantity of formic acid as the reducing agent.

5.1 Introduction

Industrial effluents and uncontrolled sewage disposal contaminate the water bodies like never before.[178] Therefore the development of smart materials for water treatment is an urgent need of the hour in the 21st century.[179] Among various metal-based pollutants, Cr(VI) is a notorious heavy metal contaminant and a popular mutagen. Furthermore, Cr(VI) ions have high mobility due to its good water solubility.[180] The leather, paper, and electroplating industries are the primary sources of Cr(VI) contamination in water.[181] Whereas, Cr(III) is an essential element to the human and animal body and is less soluble in water.[182] Plenty of advanced techniques such as adsorption and ion exchange are developed for the environmental remediation of the toxic Cr(VI) ions.[183,184] Among these, the reduction is a cost-effective and extensively used method for the same where various reducing agents are being utilized.[185] Noble metal catalysts have a notable contribution to the development of an eco-friendly pathway for the removal of Cr(VI).[186] The major obstacle in the usage of metal nanoparticles is their affinity for aggregation.[187] Template-assisted synthesis emerged as a capable strategy to overcome this drawback. Carbon nanotubes, polymers, and peptides are some examples of the materials used as templates.[188–191] It is noteworthy that some materials with grafted functional groups direct the metal ions by various interactions to guide the nanoparticle (NP) synthesis in a narrow size range.[192,193] Moreover, they exhibit uniform distribution and stability. Recent studies accounted for the relevance of metal-organic-frameworks (MOFs) as useful templates for the NP synthesis due to their exceptional stability, surface area and the room for post-synthetic modifications.[194] Moon *et al.* in their review article, explained the numerous ways of assembling the metal nanoparticles on the MOF scaffold and their potential applications.[195]

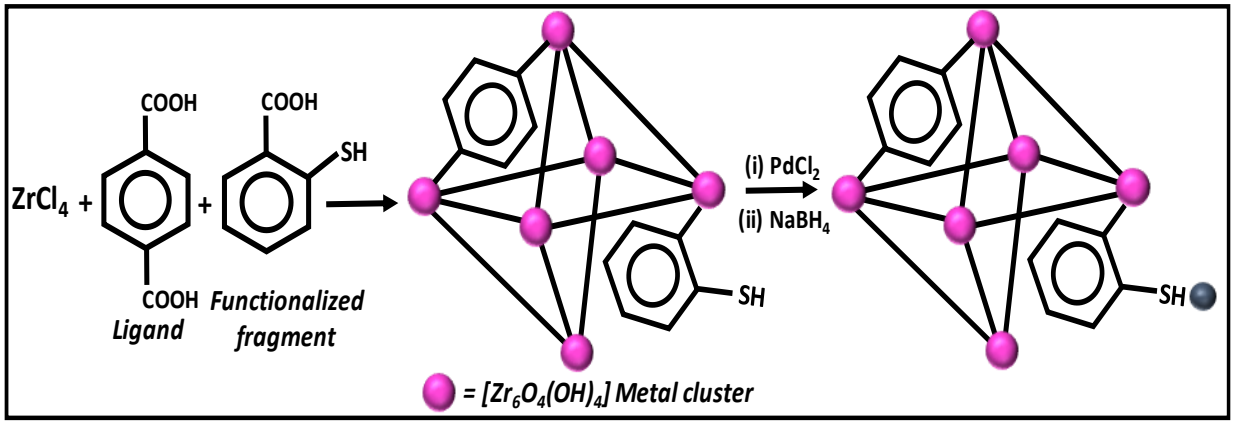

Scheme 5.1. *MLFC guided synthesis of UiO-66-SH and the integration of palladium nanoparticles.*

MLFC is a suitable method for getting rationally designed MOFs. On the other hand, it is a way to obtain scaffolds with improved properties like high surface area, pore volume and free functionalities from a known MOF.[196,197] Zirconium-based metal MOFs are in the frontline of the MLFC research due to their structural uniqueness and better thermal and mechanical stability.[198,199] The modulator has its effects on various aspects of zirconium MOFs namely crystallinity, yield, morphology, pore size, defects, porosity, and stability.[200],[201] MLFC guided synthesis of UiO-66 with the terephthalic acid fragment (benzoic acid) modulator is elucidated as the defect engineering strategy by Atzori *et al.*[121] Whereas, Kardanpour *et al.* suspended the palladium nanoparticles in UiO-66-NH_2 MOF by making use of the electrostatic interactions of the amino group with the Pd metal.[202] Keeping the ideas of MLFC and free functional groups in mind herein, a defective zirconium-based UiO-66 (UiO stands for the University of Oslo) MOF is fabricated by the MLFC approach using a thiol-functionalized modulator. The thiol sites are used for the uniform distribution of the palladium nanoparticles, and the material is utilized as an efficient catalyst for the hexavalent chromium reduction (Scheme 5.1).

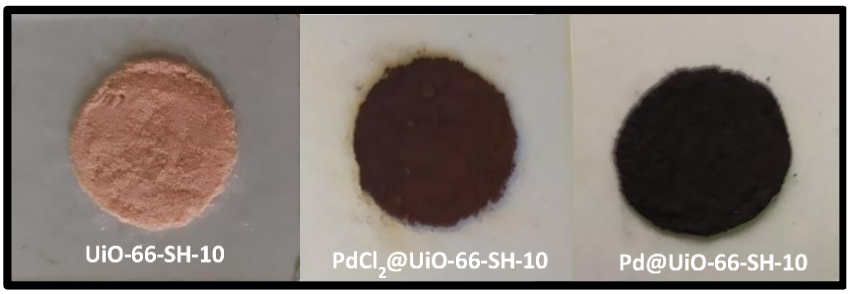

Figure 5.1. *Pictures of the catalyst at various stages of synthesis.*

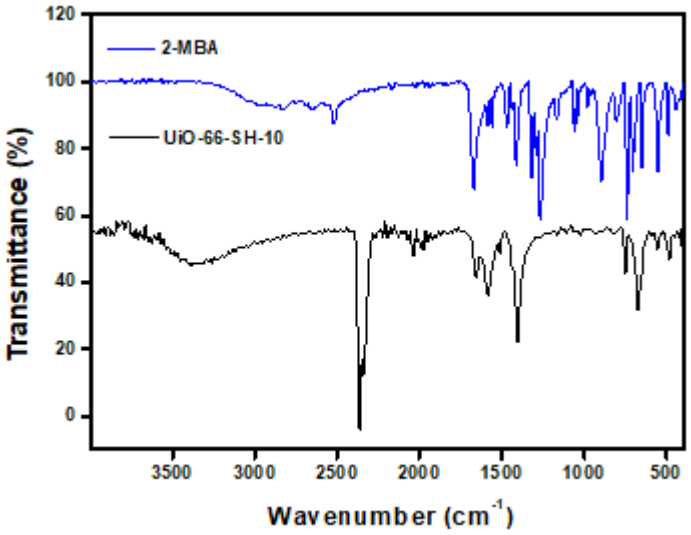

Figure 5.2. *IR spectrum of 2-MBA and UiO-66-SH-10 indicating the incorporation of the modulator.*

The exceptional stability and defect tolerance of UiO-66 is exploited in creating defective sites with the desirable free functionality which helps in guiding and grafting the metal NPs uniformly over the scaffold. Furthermore, it diminishes the likelihood of NP aggregation, thereby increasing the catalytic efficiency.

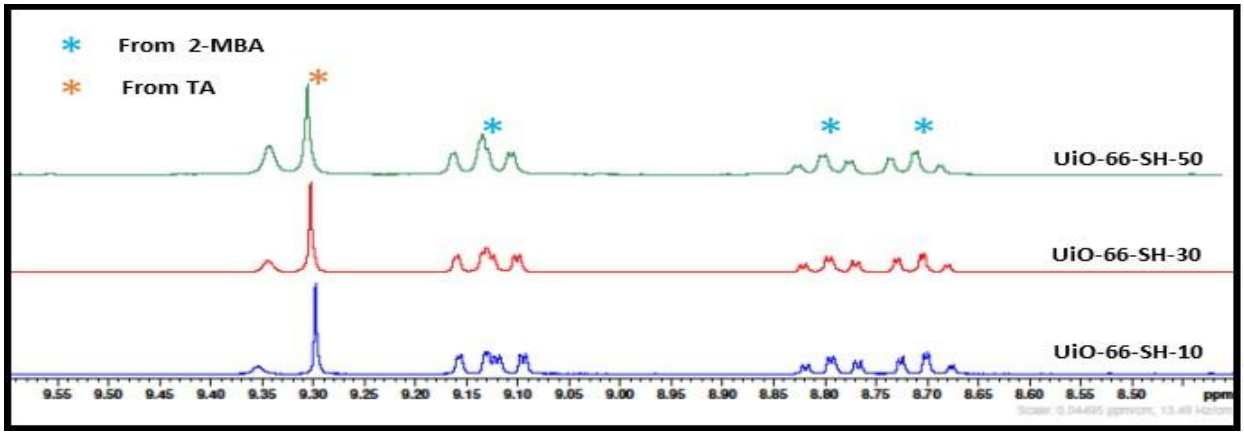

Figure 5.3. *The ^{1}H NMR spectra of UiO-66-SH with increasing feed ratio of 2-MBA.*

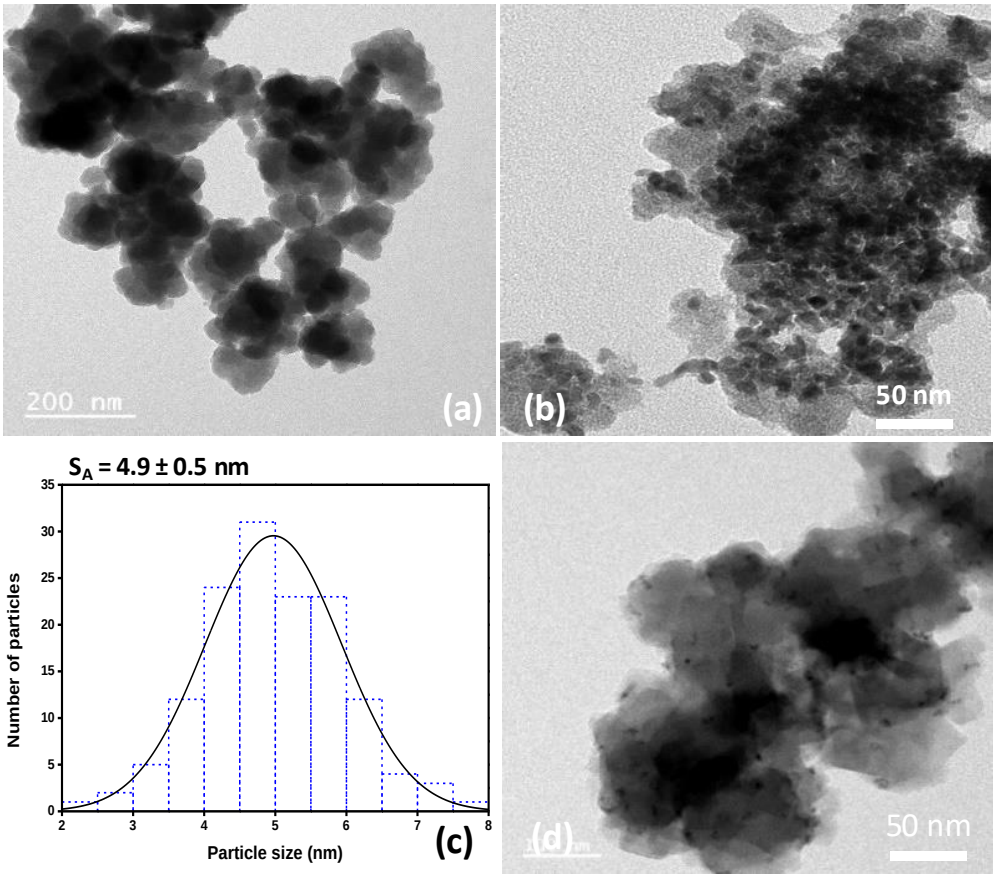

Figure 5.4. *TEM images of (a) UiO-66-SH-10 and (b) Pd@UiO-66-SH-10, (c) size distribution curve of the Pd nanoparticles, (c) TEM image of Pd@UiO-66-10.*

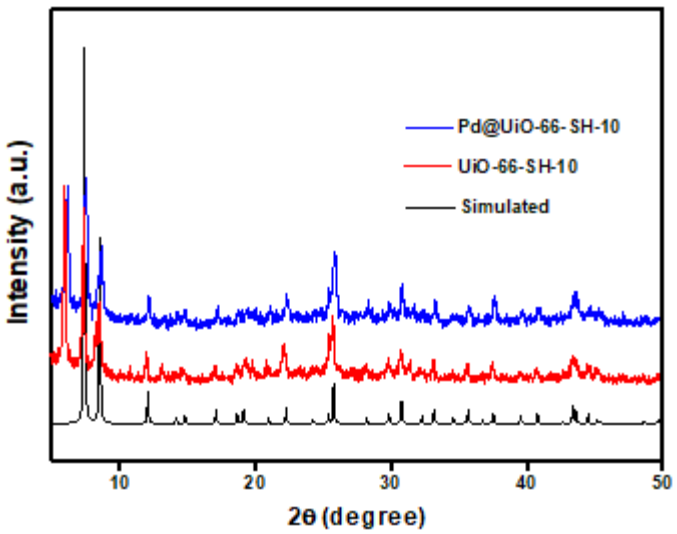

Figure 5.5. *PXRD pattern of the thiol MOF and Pd incorporated thiol MOF.*

5.2 Results and discussion

MLFC strategy is a convenient method for the introduction of functionalized mesopores into the structure of a MOF.[114]The creation of mesopores takes place by the coassembly of the ligand and its fragment with a favourable functionality.[112]The moisture stability and the easiness of altering its framework make UiO-66 a strong candidate for the MLFC.[198]Terephthalic acid (TA) and its thiol functionalized fragment 2-mercaptobenzoic acid (2-MBA) was used for building the thiol assembled defective MOF (UiO-66-SH-10, where 10 indicates the amount of 2-MBA added in millimoles). During the synthesis of UiO-66-SH-10, a part of the framework ligand TA gets replaced by the 2-MBA which was added as a modulator. This creates linker defects in the MOF scaffold which not only helps in increasing the surface area of the material but also introduces several free thiol functionalities in it. The Pd^{2+} ions preferentially get attached to these free thiol group sites which are present throughout the structure due to the soft-soft interactions. The subsequent borohydride reduction leads to the formation of uniformly distributed Pd nanoparticles (Pd NPs) in the MOF (Pd@UiO-66-SH-10) (Fig. 5.1). The thiol peaks in the FT-IR spectrum of the catalyst point out the integration of the modulator in it (Fig. 5.2). ^{1}H NMR shows the presence of 2-

MBA in the structure along with TA and the noticeable feature is the enhanced incorporation as the feed ratio of 2-MBA increased (Fig. 5.3). The TEM data revealed the uniform distribution of the NPs throughout the MOF surface. The size distribution histogram of the NPs showed the narrow size range of 3-6 nm with an average size of 4.9 ± 0.5 nm (Fig. 5.4). The PXRD data of all the thiol incorporated MOFs (UiO-66-SH-10, UiO-66-SH-30, and UiO-66-SH-50) coincide well with the simulated data, which indicate the structural purity. A new peak in the UiO-66-SH-10 at a two theta value of 4.7^0 is a characteristic of the defective MOFs (Fig. 5.5).[121]

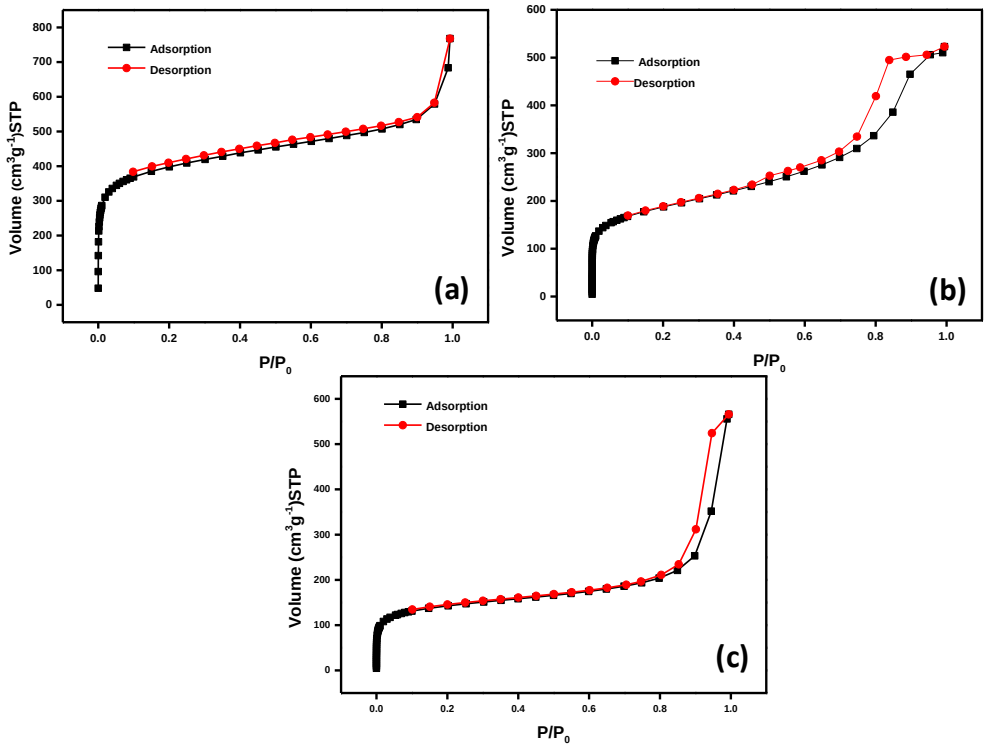

Figure 5.6. *N_2 adsorption-desorption spectra of (a) UiO-66-SH-10, (b)Pd@ UiO-66-SH-10 and (c) Pd@UiO-66-SH-10 after 5 cycles.*

The PXRD pattern of Pd@UiO-66-SH-10 did not exhibit the characteristic diffraction peaks of palladium metal nanoparticles indicating the narrow size range of the NPs formed and the low loading of the palladium on the MOF. From the N_2 adsorption-desorption results, the

surface area of the UiO-66-SH-10 was elucidated as 1240 m^2/g. After the palladium nanoparticle incorporation, the BET surface area reduced to 910 m^2/g. The decrease in the surface area and pore volume after incorporation indicates the NPs might have occupied the pores as well as the surface of the MOF. The BET surface area of the catalyst collected after five catalytic cycles was found to be reduced to a value of 513 m^2/g, which may be due to the blockage and collapse of the vacancies during the catalytic process (Fig. 5.6). Moreover, the SEM-EELS mapping points out the uniform embedding of the sulfur and palladium (Fig.5.7). The X-ray photoelectron spectra indicate the presence of sulfur and palladium in the catalyst structure (Fig.5.8). Palladium has its characteristic $Pd_{3/2}$ and $Pd_{5/2}$ peaks around 345 eV and 339 eV respectively. Potassium dichromate and formic acid (HCOOH) was used as the Cr(VI) source and reducing agent, respectively. The substrate potassium dichromate and formic acid are adsorbed onto the surface of the catalyst. Formic acid acts as the hydrogen donor to reduce Cr(VI) to Cr(III) which is monitored by UV-Visible spectroscopic study by scanning in the wavelength range 250-450 nm. The dichromate ion ($Cr_2O_7^{2-}$) has its absorption peak around 350 nm due to the ligand metal charge transfer (from O^{2-} to Cr(VI)), and the disappearance of the same indicates the complete reduction of Cr(VI) to Cr(III). Pure UiO-66 and UiO-66-SH-10 found to be inefficient for the conversion. During a period of 10h, UiO-66 and UiO-66-SH-10 exhibit a conversion <5% under similar conditions whereas, Pd@UiO-66 shows a slightly high conversion efficiency of 28%. Formic acid alone is also inactive in reducing the Cr(VI). None of the above materials matches Pd@UiO-66-SH-10 which exhibits a conversion rate of >99% within 3 minutes. Moreover, the reaction was performed under normal visible light and at room temperature (Fig. 5.9). The quantity of formic acid is considerably reduced in the present reaction compared to the other reports (Table 5.1). In fact, according to our knowledge Pd@UiO-66-SH-10 is the only catalyst to date, which shows a 100% reduction of Cr(VI) with a minute quantity of reducing agent. The

catalytic activity is retained even after 5 cycles of reaction with slightly more time of reaction.

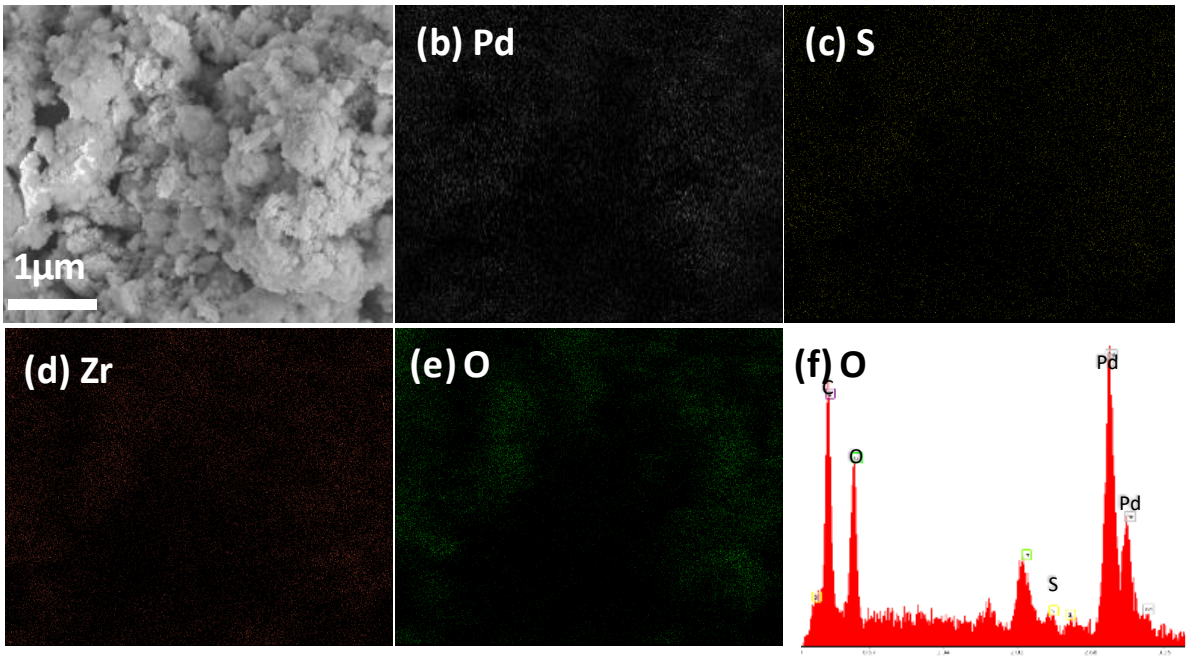

Figure 5.7. *(a) The SEM image, (b-e) SEM EELS mapping spectra showing the uniform distribution of all the elements and (f) the SEM-EDX spectra of Pd@UiO-66-SH-10.*

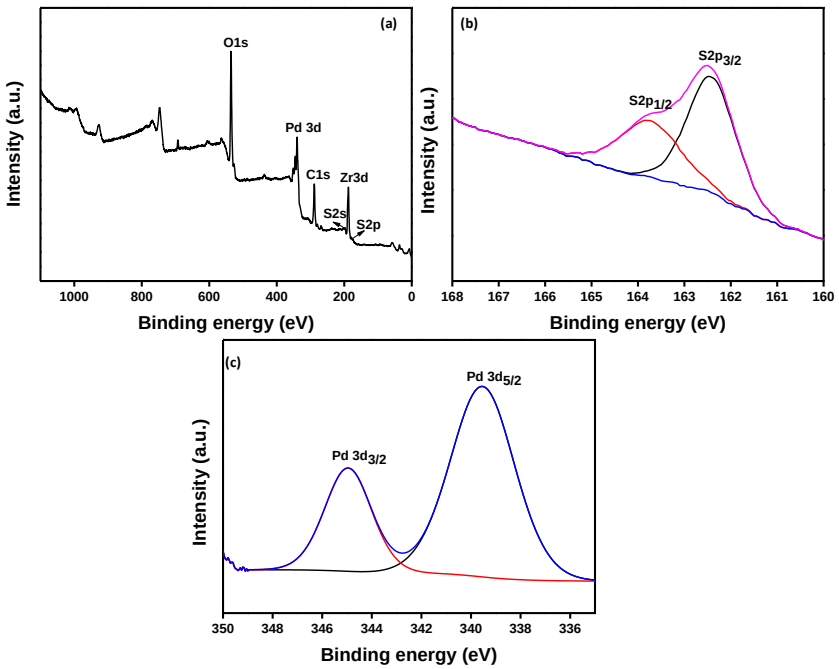

Figure 5.8. *(a)XPS survey spectra, the binding energy of (b)S and (c)Pd*

This minor change may be due to the possible blockage of the pores in the catalyst and subsequent reduction in the adsorption of substrates. The leaching test for the NPs was carried out by removing the catalyst from the solution after a catalytic cycle and adding a fresh quantity of Cr(VI) solution to the system. There was no further colour change indicating the absence of leaching and stability of the NPs (also confirmed by ICP-MS, Table 5.2) (Fig. 6.10). The TEM image of Pd@UiO-66-SH-10 after five catalytic cycles confirms the non-aggregation of the NPs (Fig. 5.11a). The PXRD data also shows the stability of the Pd@UiO-66-SH-10 (Fig. 5.11b). The visible colour change of the Cr(VI) from orange to colourless was another indicator of the reduction. When an excess of sodium hydroxide solution is added to the colourless solution obtained after the reduction reaction, a green colour is generated, indicating the presence of Cr(III) (Fig. 5.11c).

Table 5.1. *A list of reported catalysts for Cr(VI) reduction in an aqueous medium.*

No	***Catalyst***	***Time(min)***	***References***
1	*Pd@UiO-66-SH-10*	*3*	*This work.*
2	*MOF-Titanate nanotube composite*	*20*	[203]
3	*Nanostructured bismuth vanadate*	*160*	[204]
4	*Zr(IV) MOF, JLU-MOF 60*	*70*	[205]
5	*AuPd@Pd NCs*	*3*	[206]
6	*Zn MOF, NNU-36*	*60*	[207]
7	*CuPd alloy nanoparticle*	*7*	[186]
8	*Co-RGO*	*9*	[208]
9	*Pd/GO*	*12-22*	[209]
10	*Pd/Fe-NMC*	*20*	[210]

11	Mixed metal-MIL-101	15-18	[211]
12	$Pd@SiO_2–NH_2$	6	[212]
13	highly reduced $\{MnII(P^V_4Mo^V_6O_{31})_2\}$ clusters	240	[213]
14	Bi_2S_3/Bi_2WO_6	60	[214]
15	Ni NP@RGO	4	[215]
16	RGO/GO-UiO-66-NH2	120	[216]
17	Pd/Pt/Rh/Au@MIL-101	40-210	[185]
18	$Pd@UiO-66-NH_2$	90	[217]
19	Pd@uniform electrospun PEI/PVA nanofibers	12	[218]
20	NH_2–MIL-88B (Fe)	45	[40]

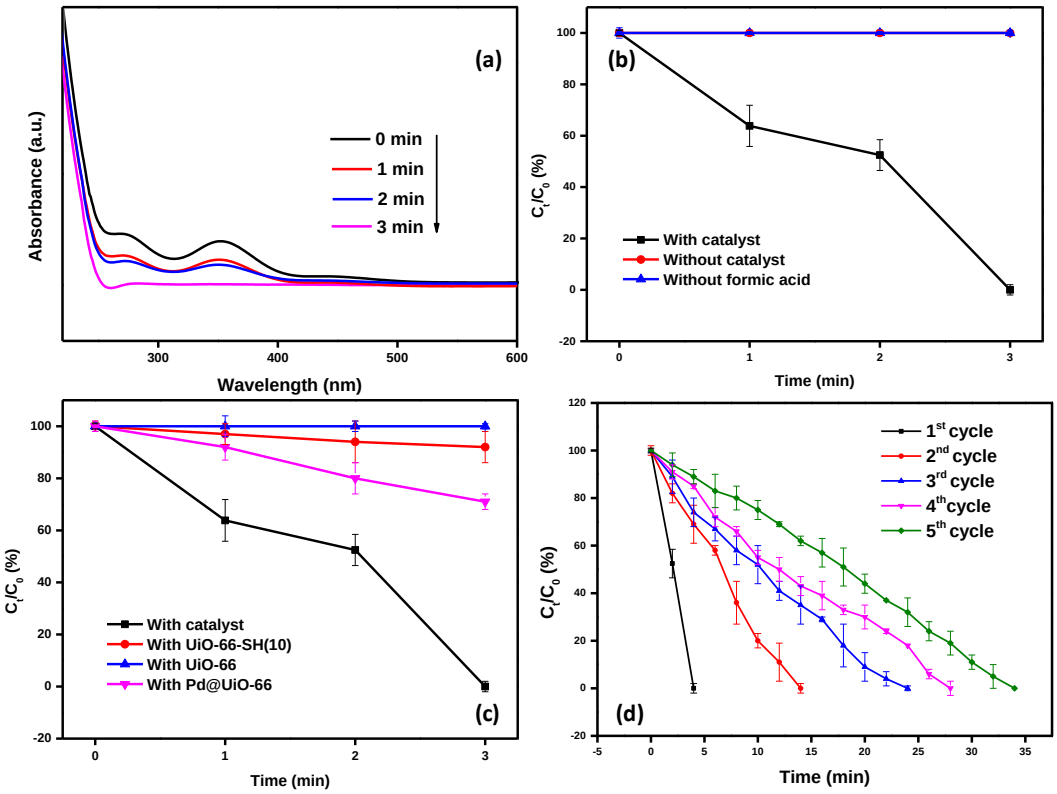

Figure 5.9. *(a)catalytic reduction of Cr(VI) over Pd@ UiO-66-SH-10 monitored using UV-vis spectroscopy (b) and (c) are the percentage conversion rate in different conditions and using various materials. (d) Conversion rates during various reduction cycles.*

Table 5.2. *The concentration of the elements of interest obtained by ICP-MS*

Condition	***Pd (mg/l)***	***Zr (mg/l)***
The solution obtained after the catalysis	*n.d.*	*n.d.*

n.d. – not detected

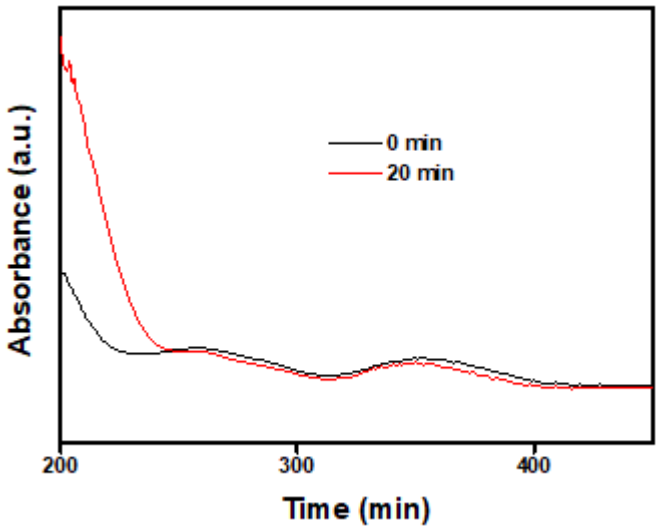

Figure 5.10. *The absorbance spectrum after the leaching test. A fresh amount of Cr(VI) solution was added to the solution after catalysis and monitored the change at 0 and 20 minutes intervals.*

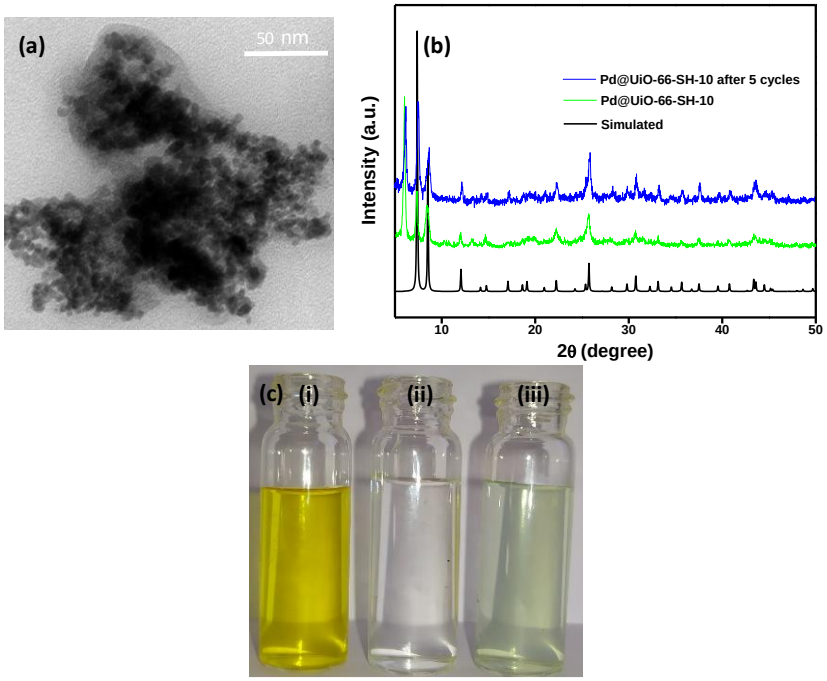

Figure 5.11. (a) *The TEM image and (b) PXRD data ofPd@UiO-66-SH-10 after five cycles of catalysis, (c) Colour change of $K_2Cr_2O_7$ (i) before the reaction, (ii) after the reaction and (iii) after adding excess dilute NaOH solution.*

5.3 Conclusions

A stable zirconium MOF (UiO-66-SH-10) was designed and synthesized by following an MLFC method. The MLFC with the thiol-functionalized modulator not only helps in creating various defect sites in the framework but also introduces the free thiol functionality throughout the scaffold. Thiol groups act as a guide and support for the palladium embedment and subsequent reduction to nanoparticles. Palladium nanoparticles thus created are uniform in size and shape and are resistant to aggregation. The Pd@UiO-66-SH-10 was utilized in the hexavalent chromium reduction revealing its high efficiency and recyclability.

5.4 Experimental section

5.4.1. Materials

Zirconium chloride ($ZrCl_4$), Terephthalic acid (TA), 2-mercaptobenzoic acid (2-MBA), Palladium chloride ($PdCl_2$), sodium borohydride($NaBH_4$), potassium dichromate ($K_2Cr_2O_7$), N, N'-dimethylformamide (DMF) and formic acid were purchased from Sigma. All the chemicals were used as received.

5.4.2 Methods of Characterization and Instrumentations

Instrumentations

Powder X-ray diffraction data (PXRD) were collected using an X'pert PRO (PANalytics) powder diffractometer equipped with CuKα radiation (1.5405 Å). The proton nuclear magnetic resonance (^{1}H NMR) analyses were carried out using an AVANCE II-500 (Bruker) NMR spectrometer. 10 mg of each sample was digested with few drops of trifluoroacetic acid-d (d-TFA) and mixed with DMSO- d6 for the ^{1}H NMR analysis. The fourier-transform

infrared (FT-IR) spectral data were recorded using KBr pellets in the range of 4000-400 cm^{-1}, with an FT-IR prestige-21 (Shimadzu) spectrometer. FEI NOVA NANOSEM 450 scanning electron microscope (SEM) with acceleration voltage 15 kV was used to determine particle size and morphology of the MOFs. SEM –EELS mapping was performed for identifying the presence of elements of interest like zirconium, sulfur, palladium, carbon, and oxygen. Tecnai G2 TF20S Twin transmission electron microscope (TEM, 300 kV) was used to record high-resolution images. Thermogravimetric analyses (TGA) were performed on an SDT Q600 (Shimadzu) analyzer in flowing nitrogen with a heating rate of 10 ^{0}C per minute. The nitrogen adsorption-desorption studies were carried out at 77 K using a Micromeritics 3 Flex automatic volumetric adsorption instrument, and the surface area was calculated using the Brunauer-Emmett-Teller (BET) method after degassing at 100 ^{0} C for 12 h. The binding energy and composition of the samples were analyzed using X-ray photoelectron spectra (XPS) using the omicron instrument, and the data were analyzed with the casaXPS software.

Synthesis

UiO-66-SH-10

The MOF was synthesized following a reported procedure with a slight modification.[243] Briefly, $ZrCl_4$ (168 mg, 0.7209 mmol), Terephthalic acid (TA, 120 mg, 0.7211 mmol), 2-mercapto benzoic acid (2-MBA, 881 mg, 10 mmol) and H_2O (17 µL, 0.9603 mmol) were dissolved in 41 mL of warm (~ 70 ℃) DMF in a hotplate under constant magnetic stirring. After the dissolution of all the reagents, the magnetic stir bar was removed, and the temperature was increased to 120 ℃ with the flask covered using a watch glass. The reaction was allowed to continue for 24 h. The purification was carried out by soaking the product in 20 mL of DMF, keeping for 12 h and repeating the process three times. The as-synthesized MOF was collected by centrifugation and dried at 60 °C in an oven for 12h and was activated for removing all the solvent DMF molecules from the pores by heating to 200 °C for 12 h.

Pd@UiO-66-SH-10

Firstly, activated UiO-66-SH-10 (50 mg) was stirred with 20 mL of $PdCl_2$ solution (17 mg, 0.1mmol) in dichloromethane (DCM) for 4 h. The $PdCl_2$@UiO-66-SH-10 was collected and washed with DCM several times to get rid of any excess amount of $PdCl_2$. The $PdCl_2$ incorporated MOF was dried by heating at 60 ℃ for 2 h in an oven. The material was then magnetically stirred with 5 mL water in a round bottom flask for 0.5 h. Freshly prepared $NaBH_4$ solution (95 mg in 5 mL water) was added dropwise over a period of 1 h at 0 °C. Stirring was continued for 24 h under the hydrogen atmosphere. Pd@UiO-66-SH-10 was washed with water and DCM and dried by heating at 60 ℃ for 12 h.

UiO-66 and Pd@UiO-66

The UiO-66 and Pd@ UiO-66 were also synthesized in a similar way using benzoic acid (BA) as the modulator in place of 2-mercaptobenzoic acid (2-MBA).

Catalysis

Potassium dichromate ($K_2Cr_2O_7$) is was selected as the representative for the formic acid-stimulated reduction of Cr(VI) to Cr(III). The reduction process was induced by formic acid as the reducing agent, and the reaction was monitored using UV-Vis spectroscopy by investigating the major dichromate ion ($Cr_2O_7^{2-}$) peak at 350 nm (λ=257 nm). The reaction was carried out in a 50 mL round bottom flask at room temperature (25 °C). 1 mg of the Pd@UiO-66-SH-10 catalyst was added to a mixture of 20 mL of $K_2Cr_2O_7$ (1 mmol) and 100 µL formic acid under magnetic stirring. 1 mL of the solution was collected in one-minute intervals, and the catalyst was removed by filtering through a 22 µL syringe filter for the UV-Vis spectroscopic study. 500 µL of the solution was diluted to 3 mL with water in a quartz cuvette for the analysis. The control reactions were also carried out without the catalyst and the reducing agent.

References

[1] *Pure Appl. Chem.* **2013**, *85*, 1715.

[2] H.-C. Zhou, J. R. Long, O. M. Yaghi, *Chem. Rev.* **2012**, *112*, 673–674.

[3] D. T. Sun, L. Peng, W. S. Reeder, S. M. Moosavi, D. Tiana, D. K. Britt, E. Oveisi, W. L. Queen, *ACS Cent. Sci.* **2018**, *4*, 349–356.

[4] A. Karmakar, P. Samanta, S. Dutta, S. K. Ghosh, *Chem. – An Asian J.* **2019**, *14*, 4506–4519.

[5] M. Wen, G. Li, H. Liu, J. Chen, T. An, H. Yamashita, *Environ. Sci. Nano,* **2019**, *6*, 1006–1025.

[6] L. Wang, M. Zheng, Z. Xie, *J. Mater. Chem. B* **2018**, *6*, 707–717.

[7] Y.-R. Lee, J. Kim, W.-S. Ahn, *Korean J. Chem. Eng.* **2013**, *30*, 1667–1680.

[8] Z. Yin, S. Wan, J. Yang, M. Kurmoo, M.-H. Zeng, *Coord. Chem. Rev.* **2019**, *378*, 500–512.

[9] M. Kandiah, S. Usseglio, S. Svelle, U. Olsbye, K. P. Lillerud, M. Tilset, *J. Mater. Chem.* **2010**, *20*, 9848–9851.

[10] M. Eddaoudi, D. B. Moler, H. Li, B. Chen, T. M. Reineke, M. O'Keeffe, O. M. Yaghi, *Acc. Chem. Res.* **2001**, *34*, 319–330.

[11] R. M. Izatt, J. S. Bradshaw, S. R. Izatt, R. G. Harrison, *Macrocycl. Supramol. Chem.* **2016**, 1–9.

[12] H. Li, M. Eddaoudi, M. O'Keeffe, O. M. Yaghi, *Nature* **1999**, *402*, 276–279.

[13] H.-L. Jiang, T. A. Makal, H.-C. Zhou, *Coord. Chem. Rev.* **2013**, *257*, 2232–2249.

[14] J. Zhang, L. Wojtas, R. W. Larsen, M. Eddaoudi, M. J. Zaworotko, *J. Am. Chem. Soc.* **2009**, *131*, 17040–17041.

[15] J. H. Park, W. R. Lee, Y. Kim, H. J. Lee, D. W. Ryu, W. J. Phang, C. S. Hong, *Cryst. Growth Des.* **2014**, *14*, 699–704.

[16] R. Haldar, N. Sikdar, T. Maji, *Mater. Today* **2015**, *18*, 97–116.

[17] J. An, R. P. Fiorella, S. J. Geib, N. L. Rosi, *J. Am. Chem. Soc.* **2009**, *131*, 8401–8403.

[18] O. Karagiaridi, W. Bury, J. E. Mondloch, J. T. Hupp, O. K. Farha, *Angew. Chemie Int. Ed.* **2014**, *53*, 4530–4540.

[19] W. P. Lustig, S. Mukherjee, N. D. Rudd, A. V Desai, J. Li, S. K. Ghosh, *Chem. Soc. Rev.* **2017**, *46*, 3242–3285.

[20] G. Ji, J. Liu, X. Gao, W. Sun, J. Wang, S. Zhao, Z. Liu, *J. Mater. Chem. A* **2017**, *5*, 10200–10205.

[21] B. Khezri, M. Pumera, *Adv. Mater.* **2019**, *31*, 1806530.

[22] I. M. Hönicke, I. Senkovska, V. Bon, I. A. Baburin, N. Bönisch, S. Raschke, J. D. Evans, S. Kaskel, *Angew. Chemie Int. Ed.* **2018**, *57*, 13780–13783.

[23] O. K. Farha, I. Eryazici, N. C. Jeong, B. G. Hauser, C. E. Wilmer, A. A. Sarjeant, R. Q. Snurr, S. T. Nguyen, A. Ö. Yazaydın, J. T. Hupp, *J. Am. Chem. Soc.* **2012**, *134*, 15016–15021.

[24] K. S. Park, Z. Ni, A. P. Côté, J. Y. Choi, R. Huang, F. J. Uribe-Romo, H. K. Chae, M. O'Keeffe, O. M. Yaghi, *Proc. Natl. Acad. Sci.* **2006**, *103*, 10186 LP – 10191.

[25] S. Yuan, L. Feng, K. Wang, J. Pang, M. Bosch, C. Lollar, Y. Sun, J. Qin, X. Yang, P. Zhang, et al.,

Adv. Mater. **2018**, *30*, 1704303.

[26] J. H. Cavka, S. Jakobsen, U. Olsbye, N. Guillou, C. Lamberti, S. Bordiga, K. P. Lillerud, *J. Am. Chem. Soc.* **2008**, *130*, 13850–13851.

[27] C. H. Hendon, D. Tiana, A. Walsh, *Phys. Chem. Chem. Phys.* **2012**, *14*, 13120–13132.

[28] Z. Guo, D. K. Panda, K. Maity, D. Lindsey, T. G. Parker, T. E. Albrecht-Schmitt, J. L. Barreda-Esparza, P. Xiong, W. Zhou, S. Saha, *J. Mater. Chem. C* **2016**, *4*, 894–899.

[29] G. Mínguez Espallargas, E. Coronado, *Chem. Soc. Rev.* **2018**, *47*, 533–557.

[30] M. P. Suh, H. J. Park, T. K. Prasad, D.-W. Lim, *Chem. Rev.* **2012**, *112*, 782–835.

[31] Q. Yang, Y. Zhu, B. Luo, F. Lan, Y. Wu, Z. Gu, *Nanoscale* **2017**, *9*, 527–532.

[32] Y. Yan, I. da Silva, A. J. Blake, A. Dailly, P. Manuel, S. Yang, M. Schröder, *Inorg. Chem.* **2018**, *57*, 12050–12055.

[33] J. Pawliszyn, *Handbook of Solid Phase Microextraction*, Elsevier, **2011**.

[34] Y.-A. Li, F. Yang, Z.-C. Liu, Q.-K. Liu, Y.-B. Dong, *J. Mater. Chem. A* **2014**, *2*, 13868–13872.

[35] P. Rocío-Bautista, I. Pacheco-Fernández, J. Pasán, V. Pino, *Anal. Chim. Acta* **2016**, *939*, 26–41.

[36] Y. He, M. Concheiro-Guisan, *Biomed. Chromatogr.* **2019**, *33*, e4444.

[37] X. Zhao, Y. Zhang, J. Han, H. Jing, Z. Gao, H. Huang, Y. Wang, C. Zhong, *Microporous Mesoporous Mater.* **2018**, *268*, 88–92.

[38] Y. Wang, C. Hou, Y. Zhang, F. He, M. Liu, X. Li, *J. Mater. Chem. B* **2016**, *4*, 3695–3702.

[39] X. Fang, B. Zong, S. Mao, *Nano-Micro Lett.* **2018**, *10*, 64.

[40] L. Shi, T. Wang, H. Zhang, K. Chang, X. Meng, H. Liu, J. Ye, *Adv. Sci.* **2015**, *2*, 1500006.

[41] T. Zhang, Y.-Q. Hu, T. Han, Y.-Q. Zhai, Y.-Z. Zheng, *ACS Appl. Mater. Interfaces* **2018**, *10*, 15786–15792.

[42] N. J. Hinks, A. C. McKinlay, B. Xiao, P. S. Wheatley, R. E. Morris, *Microporous Mesoporous Mater.* **2010**, *129*, 330–334.

[43] S. R. Miller, D. Heurtaux, T. Baati, P. Horcajada, J.-M. Grenèche, C. Serre, *Chem. Commun.* **2010**, *46*, 4526–4528.

[44] J. R. Miller, P. Simon, *Science (80-.).* **2008**, *321*, 651 LP – 652.

[45] G. Zhu, H. Wen, M. Ma, W. Wang, L. Yang, L. Wang, X. Shi, X. Cheng, X. Sun, Y. Yao, *Chem. Commun.* **2018**, *54*, 10499–10502.

[46] J. Zhou, Y. Dou, A. Zhou, R.-M. Guo, M.-J. Zhao, J.-R. Li, *Adv. Energy Mater.* **2017**, *7*, 1602643.

[47] Q. Wang, W. Sun, T. Xie, L. Cao, J. Yang, *Chem. – An Asian J.* **2019**, *14*, 416–421.

[48] M. Kalaj, M. S. Denny Jr., K. C. Bentz, J. M. Palomba, S. M. Cohen, *Angew. Chemie Int. Ed.* **2019**, *58*, 2336–2340.

[49] K.-K. Yee, N. Reimer, J. Liu, S.-Y. Cheng, S.-M. Yiu, J. Weber, N. Stock, Z. Xu, *J. Am. Chem. Soc.* **2013**, *135*, 7795–7798.

[50] D. Xie, Y. Ma, Y. Gu, H. Zhou, H. Zhang, G. Wang, Y. Zhang, H. Zhao, *J. Mater. Chem. A* **2017**, *5*, 23794–23804.

[51] S. Rapti, D. Sarma, S. A. Diamantis, E. Skliri, G. S. Armatas, A. C. Tsipis, Y. S. Hassan, M. Alkordi, C. D. Malliakas, M. G. Kanatzidis, et al., *J. Mater. Chem. A* **2017**, *5*, 14707–14719.

[52] W. Ye, Y. Li, J. Wang, B. Li, Y. Cui, Y. Yang, G. Qian, *J. Solid State Chem. Fr.* **2020**, *281*, 121032.

[53] Q. Yang, J. Wang, X. Chen, W. Yang, H. Pei, N. Hu, Z. Li, Y. Suo, T. Li, J. Wang, *J. Mater. Chem. A* **2018**, *6*, DOI 10.1039/C7TA08399H.

[54] J. Geoghegan, J. L. Tong, *Contin. Educ. Anaesthesia, Crit. Care Pain* **2006**, *6*, 230–234.

[55] N. S. Bobbitt, M. L. Mendonca, A. J. Howarth, T. Islamoglu, J. T. Hupp, O. K. Farha, R. Q. Snurr, *Chem. Soc. Rev.* **2017**, *46*, 3357–3385.

[56] J. A. Harvey, C. J. Pearce, M. G. Hall, E. J. Bruni, J. B. DeCoste, D. F. Sava Gallis, *Dalt. Trans.* **2019**, *48*, 16153–16157.

[57] K.-S. Ju, R. E. Parales, *Microbiol. Mol. Biol. Rev.* **2010**, *74*, 250 LP – 272.

[58] B. Wang, X.-L. Lv, D. Feng, L.-H. Xie, J. Zhang, M. Li, Y. Xie, J.-R. Li, H.-C. Zhou, *J. Am. Chem. Soc.* **2016**, *138*, 6204–6216.

[59] T. K. Kim, J. H. Lee, D. Moon, H. R. Moon, *Inorg. Chem.* **2013**, *52*, 589–595.

[60] D. P. Selid, H. Xu, E. M. Collins, M. Striped Face-Collins, J. X. Zhao, *Sensors* **2009**, *9*, DOI 10.3390/s90705446.

[61] I. Onyido, A. R. Norris, E. Buncel, *Chem. Rev.* **2004**, *104*, 5911–5930.

[62] N. Bloom, W. F. Fitzgerald, *Anal. Chim. Acta* **1988**, *208*, 151–161.

[63] J. Fu, L. Wang, H. Chen, L. Bo, C. Zhou, J. Chen, *Spectrochim. Acta. A. Mol. Biomol. Spectrosc.* **2010**, *77*, 625–629.

[64] Y.-L. Yu, Z. Du, J.-H. Wang, *J. Anal. At. Spectrom.* **2007**, *22*, 650–656.

[65] C. Wu, J. Wang, J. Shen, C. Bi, H. Zhou, *Sensors Actuators B Chem.* **2017**, *243*, 678–683.

[66] J. Wang, M. Musameh, Y. Lin, *J. Am. Chem. Soc.* **2003**, *125*, 2408–2409.

[67] D. Li, A. Wieckowska, I. Willner, *Angew. Chemie Int. Ed.* **2008**, *47*, 3927–3931.

[68] S. Jayabal, R. Sathiyamurthi, R. Ramaraj, *J. Mater. Chem. A* **2014**, *2*, 8918–8925.

[69] Y.-M. Zhu, C.-H. Zeng, T.-S. Chu, H.-M. Wang, Y.-Y. Yang, Y.-X. Tong, C.-Y. Su, W.-T. Wong, *J. Mater. Chem. A* **2013**, *1*, 11312–11319.

[70] M. D. Allendorf, C. A. Bauer, R. K. Bhakta, R. J. T. Houk, *Chem. Soc. Rev.* **2009**, *38*, 1330–1352.

[71] Y. Cui, Y. Yue, G. Qian, B. Chen, *Chem. Rev.* **2012**, *112*, 1126–1162.

[72] H. Ma, L. Wang, J. Chen, X. Zhang, L. Wang, N. Xu, G. Yang, P. Cheng, *Dalt. Trans.* **2017**, *46*, 3526–3534.

[73] Z.-L. Wu, J. Dong, W.-Y. Ni, B.-W. Zhang, J.-Z. Cui, B. Zhao, *Inorg. Chem.* **2015**, *54*, 5266–5272.

[74] Y.-Q. Chen, G.-R. Li, Z. Chang, Y.-K. Qu, Y.-H. Zhang, X.-H. Bu, *Chem. Sci.* **2013**, *4*, 3678–3682.

[75] H.-W. Tseng, Y.-J. Tsai, J.-H. Yen, P.-H. Chen, Y.-C. Yeh, *Chem. Commun.* **2014**, *50*, 1735–1737.

[76] C. D\'\iez-Gil, R. Mart\'\inez, I. Ratera, T. Hirsh, A. Espinosa, A. Tarraga, P. Molina, O. S. Wolfbeis, J. Veciana, *Chem. Commun.* **2011**, *47*, 1842–1844.

[77] S. Choi, Y. Kim, *RSC Adv.* **2015**, *5*, 95268–95272.

[78] S. Tatay, P. Gaviña, E. Coronado, E. Palomares, *Org. Lett.* **2006**, *8*, 3857–3860.

[79] S. A. A. Razavi, M. Y. Masoomi, A. Morsali, *Inorg. Chem.* **2017**, *56*, 9646–9652.

[80] L. Wen, X. Zheng, K. Lv, C. Wang, X. Xu, *Inorg. Chem.* **2015**, *54*, 7133–7135.

[81] P. Samanta, A. V Desai, S. Sharma, P. Chandra, S. K. Ghosh, *Inorg. Chem.* **2018**, *57*, 2360–2364.

[82] U. Ghosh, S. S. Bag, C. Mukherjee, *Sensors Actuators B Chem.* **2017**, *238*, 903–907.

[83] J. Yang, Z. Wang, Y. Li, Q. Zhuang, W. Zhao, J. Gu, *RSC Adv.* **2016**, *6*, 69807–69814.

[84] M.-M. Chen, L. Chen, H.-X. Li, L. Brammer, J.-P. Lang, *Inorg. Chem. Front.* **2016**, *3*, 1297–1305.

[85] P. Wu, Y. Liu, Y. Liu, J. Wang, Y. Li, W. Liu, J. Wang, *Inorg. Chem.* **2015**, *54*, 11046–11048.

[86] A. Senthamizhan, A. Celebioglu, T. Uyar, *J. Mater. Chem. A* **2014**, *2*, 12717–12723.

[87] Z. Aydin, Y. Wei, M. Guo, *Inorg. Chem. Commun.* **2014**, *50*, DOI 10.1016/j.inoche.2014.10.026.

[88] J. Hu, T. Wu, G. Zhang, S. Liu, *Macromolecules* **2012**, *45*, 3939–3947.

[89] X. Liu, Y. Tang, L. Wang, J. Zhang, S. Song, C. Fan, S. Wang, *Adv. Mater.* **2007**, *19*, 1662.

[90] Y. Zou, M. Wan, G. Sang, M. Ye, Y. Li, *Adv. Funct. Mater.* **2008**, *18*, 2724–2732.

[91] SMART (V 5.628), SAINT (V 6.45a), XPREP, SHELXTL, Bruker AXSInc., Madison, WI, **2004**.

[92] M. Sheldrick, Siemens Area Correction Absorption Correction Program, University of Göttingen, Göttingen, Germany, **1994**.

[93] G. M. Sheldrick, SHELXL-97 Program for Crystal Structure Solution and Refinement, University of Göttingen, Göttingen, Germany, **1997**.

[94] J. L. J. Farrugia, *App. Crystallography*, **1999**, *32*, 837.

[95] M. S. Gultekin, M. C. and M. Balci, *Curr. Org. Chem.* **2004**, *8*, 1159–1186.

[96] X. Qi, R. F. Tester, *Clin. Nutr. ESPEN* **2019**, *33*, 18–28.

[97] M. Qureshi, *HARPER'S ILLUSTRATED BIOCHEMISTRY 30th*, **2018**.

[98] S. Li, Y. Jin, J. Wang, Z. Tang, S. Xu, T. Wang, Z. Cai, *Analyst* **2016**, *141*, 1144–1153.

[99] H. Kelebek, S. Selli, A. Canbas, T. Cabaroglu, *Microchem. J.* **2009**, *91*, 187–192.

[100] M. Asami, M. Yamamura, W. Takasaki, Y. Tanaka, *J. Chromatogr. B Biomed. Sci. Appl.* **1995**, *665*, 107–116.

[101] M. B. Espina-Benitez, J. Randon, C. Demesmay, V. Dugas, *J. Chromatogr. A* **2017**, *1494*, 65–76.

[102] Y. Li, Z. Zhang, B. Liu, J. Liu, *Langmuir* **2019**, *35*, 13727–13734.

[103] X. Wu, Z. Li, X.-X. Chen, J. S. Fossey, T. D. James, Y.-B. Jiang, *Chem. Soc. Rev.* **2013**, *42*, 8032–8048.

[104] P. Hu, Y. Song, M. D. Rojas-Andrade, S. Chen, *Langmuir* **2014**, *30*, 5224–5229.

[105] C. Yu, V. W.-W. Yam, *Chem. Commun.* **2009**, 1347–1349.

[106] C. Tiangco, D. Fon, N. Sardesai, Y. Kostov, F. Sevilla, G. Rao, L. Tolosa, *Sensors Actuators B Chem.* **2017**, *242*, 569–576.

[107] J. Du, M. He, X. Wang, H. Fan, Y. Wei, *Biomed. Chromatogr.* **2015**, *29*, 312–320.

[108] J. Ma, C. Wang, Y. Wei, *RSC Adv.* **2016**, *6*, 43648–43655.

[109] W. L. A. Brooks, B. S. Sumerlin, *Chem. Rev.* **2016**, *116*, 1375–1397.

[110] H. Furukawa, K. E. Cordova, M. O'Keeffe, O. M. Yaghi, *Science (80-.).* **2013**, *341*, 1230444.

[111] Q. Zhang, J. Yu, J. Cai, L. Zhang, Y. Cui, Y. Yang, B. Chen, G. Qian, *Chem. Commun.* **2015**, *51*, 14732–14734.

[112] J. Park, Z. U. Wang, L.-B. Sun, Y.-P. Chen, H.-C. Zhou, *J. Am. Chem. Soc.* **2012**, *134*, 20110–20116.

[113] G. Zhang, H. Fei, *Chem. Commun.* **2017**, *53*, 4156–4159.

[114] X. Zhu, J. Gu, J. Zhu, Y. Li, L. Zhao, J. Shi, *Adv. Funct. Mater.* **2015**, *25*, 3847–3854.

[115] G. Barin, V. Krungleviciute, O. Gutov, J. T. Hupp, T. Yildirim, O. K. Farha, *Inorg. Chem.* **2014**, *53*, 6914–6919.

[116] S.-Y. Kim, A.-R. Kim, J. W. Yoon, H.-J. Kim, Y.-S. Bae, *Chem. Eng. J.* **2018**, *335*, 94–100.

[117] T. Maity, D. Saha, S. Das, S. Koner, *Eur. J. Inorg. Chem.* **2012**, *2012*, 4914–4920.

[118] A. E. Platero-Prats, M. Iglesias, N. Snejko, Á. Monge, E. Gutiérrez-Puebla, *Cryst. Growth Des.* **2011**, *11*, 1750–1758.

[119] Z. Fang, B. Bueken, D. E. De Vos, R. A. Fischer, *Angew. Chem. Int. Ed. Engl.* **2015**, *54*, 7234–7254.

[120] O. V Gutov, M. G. Hevia, E. C. Escudero-Adán, A. Shafir, *Inorg. Chem.* **2015**, *54*, 8396–8400.

[121] C. Atzori, G. C. Shearer, L. Maschio, B. Civalleri, F. Bonino, C. Lamberti, S. Svelle, K. P. Lillerud, S. Bordiga, *J. Phys. Chem. C* **2017**, *121*, 9312–9324.

[122] K. Oshima, E. Kitazono, Y. Aoyama, *Tetrahedron Lett.* **1997**, *38*, 5001–5004.

[123] S. Mohapatra, N. Panda, P. Pramanik, *Mater. Sci. Eng. C* **2009**, *29*, 2254–2260.

[124] C. Lü, H. Li, H. Wang, Z. Liu, *Anal. Chem.* **2013**, *85*, 2361–2369.

[125] E. Uğuzdoğan, E. B. Denkbaş, A. Tuncel, *Macromol. Biosci.* **2002**, *2*, 214–222.

[126] Y. Zhao, B. G. Trewyn, I. I. Slowing, V. S.-Y. Lin, *J. Am. Chem. Soc.* **2009**, *131*, 8398–8400.

[127] D. J. WILBUR, C. WILLIAMS, A. ALLERHAND, *Chem. Informationsd.* **1977**, *8*, no--no.

[128] P. W. WERTZ, J. C. GARVER, L. ANDERSON, *Chem. Informationsd.* **1981**, *12*, no--no.

[129] M. Shimomura, B. Ono, K. Oshima, S. Miyauchi, *Polymer (Guildf).* **2006**, *47*, 5785–5790.

[130] Organization W. H., Safety I. P. on C., **n.d.**

[131] L. H. Keith, *Polycycl. Aromat. Compd.* **2015**, *35*, 147–160.

[132] J. Pawliszyn, *Solid Phase Microextraction*, Wiley-VCH, New York, **1997**.

[133] J. Zheng, J. Huang, Q. Yang, C. Ni, X. Xie, Y. Shi, J. Sun, F. Zhu, G. Ouyang, *TrAC - Trends Anal. Chem.* **2018**, *108*, 135–153.

[134] M. Mattarozzi, M. Giannetto, A. Secchi, F. Bianchi, *J. Chromatogr. A* **2009**, *1216*, 3725–3730.

[135] F. Bianchi, M. Careri, A. Mangia, M. Mattarozzi, M. Musci, *J. Chromatogr. A* **2008**, *1196–1197*, 41–45.

[136] J. N. Hao, B. Yan, *Adv. Funct. Mater.* **2017**, *27*, 1603856.

[137] L. Bromberg, Y. Diao, H. Wu, S. A. Speakman, T. A. Hatton, *Chem. Mater.* **2012**, *24*, 1664–1675.

[138] K. Yang, Q. Sun, F. Xue, D. Lin, *J. Hazard. Mater.* **2011**, *195*, 124–131.

[139] I. Abánades Lázaro, R. S. Forgan, *Coord. Chem. Rev.* **2019**, *380*, 230–259.

[140] Y. Jia, Y. Zhao, M. Zhao, Z. Wang, X. Chen, M. Wang, *J. Chromatogr. A* **2018**, *1551*, 21–28.

[141] B. Hashemi, P. Zohrabi, N. Raza, K.-H. Kim, *TrAC Trends Anal. Chem.* **2017**, *97*, 65–82.

[142] J. Li, Y. Liu, H. Su, Y.-L. Elaine Wong, X. Chen, T.-W. Dominic Chan, Q. Chen, *Microchim. Acta* **2017**, *184*, 3809–3815.

[143] S. Liu, L. Xie, Q. Hu, H. Yang, G. Pan, F. Zhu, S. Yang, G. Ouyang, *Anal. Chim. Acta* **2017**, *987*, 38–46.

[144] D. Balestri, I. Bassanetti, S. Canossa, C. Gazzurelli, A. Bacchi, S. Bracco, A. Comotti, P. Pelagatti, *Cryst. Growth Des.* **2018**, *18*, 6824–6832.

[145] F. Bertani, N. Riboni, F. Bianchi, G. Brancatelli, E. S. Sterner, R. Pinalli, S. Geremia, T. M. Swager, E. Dalcanale, *Chem. Eur. J.* **2016**, *22*, 3312–3319.

[146] F. Bianchi, F. Bisceglie, S. Dugheri, G. Arcangeli, V. Cupelli, E. del Borrello, L. Sidisky, M. Careri, *J. Chromatogr. A* **2014**, *1331*, 1–9.

[147] N. Riboni, J. W. Trzcinski, F. Bianchi, C. Massera, R. Pinalli, L. Sidisky, E. Dalcanale, M. Careri, *Anal. Chim. Acta* **2016**, *905*, 79–84.

[148] S. H. Huo, J. Yu, Y. Y. Fu, P. X. Zhou, *RSC Adv.* **2016**, *6*, 14042–14048.

[149] Y. Tian, M. Sun, X. Wang, C. Luo, J. Feng, *Chromatographia* **2018**, *81*, 1053–1061.

[150] H. Amanzadeh, Y. Yamini, M. Y. Masoomi, A. Morsali, *New J. Chem.* **2017**, *41*, 12035–12043.

[151] N. Zhang, C. Huang, P. Tong, Z. Feng, X. Wu, L. Zhang, *J. Chromatogr. A* **2018**, *1556*, 37–46.

[152] L. Xie, S. Liu, Z. Han, R. Jiang, H. Liu, F. Zhu, F. Zeng, C. Su, G. Ouyang, *Anal. Chim. Acta* **2015**, *853*, 303–310.

[153] J. Gao, C. Huang, Y. Lin, P. Tong, L. Zhang, *J. Chromatogr. A* **2016**, *1436*, 1–8.

[154] X.-F. Chen, H. Zang, X. Wang, J.-G. Cheng, R.-S. Zhao, C.-G. Cheng, X.-Q. Lu, *Analyst* **2012**, *137*, 5411–5419.

[155] S.-H. Huo, J. Yu, Y.-Y. Fu, P.-X. Zhou, *RSC Adv.* **2016**, *6*, 14042–14048.

[156] Y. T., M. Sun, X. Wang, C. Luo, J. Feng, *Chromatographia* **2018**, *81*, DOI 10.1007/s10337-018-3524-2.

[157] Y. Jia, H. Su, Z. Wang, Y.-L. E. Wong, X. Chen, M. Wang, T.-W. D. Chan, *Anal. Chem.* **2016**, *88*,

9364–9367.

[158] J. Zheng, S. Li, Y. Wang, L. Li, C. Su, H. Liu, F. Zhu, R. Jiang, G. Ouyang, *Anal. Chim. Acta* **2014**, *829*, 22–27.

[159] S. Sun, L. Huang, H. Xiao, Q. Shuai, S. Hu, *Talanta* **2019**, *202*, 145–151.

[160] Q.-L. Li, X. Wang, X.-F. Chen, M.-L. Wang, R.-S. Zhao, *J. Chromatogr. A* **2015**, *1415*, 11–19.

[161] S. Wei, W. Lin, J. Xu, Y. Wang, S. Liu, F. Zhu, Y. Liu, G. Ouyang, *Anal. Chim. Acta* **2017**, *971*, 48–54.

[162] J. Kong, F. Zhu, W. Huang, H. He, J. Hu, C. Sun, Q. Xian, S. Yang, *J. Chromatogr. A* **2019**, *1603*, 92–101.

[163] M. Liu, J. Liu, C. Guo, Y. Li, *J. Chromatogr. A* **2019**, *1584*, 57–63.

[164] M. Behzadi, E. Noroozian, M. Mirzaei, *Talanta* **2013**, *108*, 66–73.

[165] A. N. Dias, V. Simão, J. Merib, E. Carasek, *Anal. Chim. Acta* **2013**, *772*, 33–39.

[166] L. Yang, J. Zhang, F. Zhao, B. Zeng, *J. Chromatogr. A* **2016**, *1471*, 80–86.

[167] Z. Feng, C. Huang, Y. Guo, W. Liu, L. Zhang, *Talanta* **2020**, *209*, 120541.

[168] H. Jiang, X. Hu, Y. Li, J. Qi, X. Sun, L. Wang, J. Li, *Talanta* **2019**, *195*, 647–654.

[169] L. Yin, Q. Hu, S. Mondal, J. Xu, G. Ouyang, *Talanta* **2019**, *202*, 90–95.

[170] M. M. Abolghasemi, B. Karimi, V. Yousefi, *Anal. Chim. Acta* **2013**, *804*, 280–286.

[171] M. Guo, W. Song, T. Wang, Y. Li, X. Wang, X. Du, *Talanta* **2015**, *144*, 998–1006.

[172] M. Kazemipour, M. Behzadi, R. Ahmadi, *Microchem. J.* **2016**, *128*, 258–266.

[173] N. Zhang, L. Su, S. Man, X. Lei, T. Huang, C. Zhu, L. Zhang, X. Wu, *J. Chromatogr. A* **2019**, *1598*, 49–57.

[174] Y. Tian, M. Sun, X. Wang, C. Luo, J. Feng, *Chromatographia* **2018**, *81*, 1053–1061.

[175] R. Carlson, *Design and Optimization in Organic Synthesis*, Elsevier, **1992**.

[176] F. Bianchi, M. Mattarozzi, N. Riboni, P. Mora, S. A. Gandolfi, M. Careri, *J. Pharm. Biomed. Anal.* **2017**, *142*, 343–347.

[177] B. Magnusson, U. Örnemark, Eds. , *Eurachem Guide: The Fitness for Purpose of Analytical Methods – A Laboratory Guide to Method Validation and Related Topic*, **2014**.

[178] E. M. Dias, C. Petit, *J. Mater. Chem. A* **2015**, *3*, 22484–22506.

[179] M. Mon, R. Bruno, J. Ferrando-Soria, D. Armentano, E. Pardo, *J. Mater. Chem. A* **2018**, *6*, 4912–4947.

[180] D. W. Elliott, W. Zhang, *Environ. Sci. Technol.* **2001**, *35*, 4922–4926.

[181] X. Lai, D. Sun, Y. Hou, Y. Zuo, Y. Li, L. Zhang, *Adv. Mater. Interfaces* **2018**, *5*, 1800630.

[182] A. Dandapat, D. Jana, G. De, *Appl. Catal. A-general - APPL CATAL A-GEN* **2011**, *396*, 34–39.

[183] B. Qiu, H. Gu, X. Yan, J. Guo, Y. Wang, D. Sun, Q. Wang, M. Khan, X. Zhang, B. L. Weeks, et al., *J. Mater. Chem. A* **2014**, *2*, 17454–17462.

[184] D. Petruzzelli, R. Passino, G. Tiravanti, *Ind. Eng. Chem. Res.* **1995**, *34*, 2612–2617.

[185] M. Yadav, Q. Xu, *Chem. Commun.* **2013**, *49*, 3327–3329.

[186] H. Saikia, B. J. Borah, Y. Yamada, P. Bharali, *J. Colloid Interface Sci.* **2017**, *486*, 46–57.

[187] A. Albanese, W. C. W. Chan, *ACS Nano* **2011**, *5*, 5478–5489.

[188] B. Yoon, C. M. Wai, *J. Am. Chem. Soc.* **2005**, *127*, 17174–17175.

[189] N. R. Jana, L. Gearheart, C. J. Murphy, *Adv. Mater.* **2001**, *13*, 1389–1393.

[190] J. H. Ding, D. L. Gin, *Chem. Mater.* **2000**, *12*, 22–24.

[191] R. R. Naik, S. E. Jones, C. J. Murray, J. C. McAuliffe, R. A. Vaia, M. O. Stone, *Adv. Funct. Mater.* **2004**, *14*, 25–30.

[192] J. S. Oh, L. N. Dang, S. W. Yoon, P. C. Lee, D. O. Kim, K. J. Kim, J. Do Nam, *Macromol. Rapid Commun.* **2013**, *34*, 504–510.

[193] C. T. Nguyen, T. H. Tran, X. Lu, R. M. Kasi, *Polym. Chem.* **2014**, *5*, 2774–2783.

[194] S. Wang, C. M. McGuirk, A. d'Aquino, J. A. Mason, C. A. Mirkin, *Adv. Mater.* **2018**, *30*, 1800202.

[195] C. Rösler, R. Fischer, *CrystEngComm* **2014**, *17*, DOI 10.1039/C4CE01251H.

[196] M. Zhang, M. Bosch, T. Gentle III, H.-C. Zhou, *CrystEngComm* **2014**, *16*, 4069–4083.

[197] H. V Doan, A. Sartbaeva, J.-C. Eloi, S. A. Davis, V. P. Ting, *Sci. Rep.* **2019**, *9*, 10887.

[198] Y. Yang, Z. Niu, H. Li, Y. Ma, Y. Zhang, H. Wang, *Dalt. Trans.* **2018**, *47*, 6538–6548.

[199] G. C. Shearer, S. Chavan, S. Bordiga, S. Svelle, U. Olsbye, K. P. Lillerud, *Chem. Mater.* **2016**, *28*, 3749–3761.

[200] Z. Hu, I. Castano, S. Wang, Y. Wang, Y. Peng, Y. Qian, C. Chi, X. Wang, D. Zhao, *Cryst. Growth Des.* **2016**, *16*, 2295–2301.

[201] H. Wu, Y. S. Chua, V. Krungleviciute, M. Tyagi, P. Chen, T. Yildirim, W. Zhou, *J. Am. Chem. Soc.* **2013**, *135*, 10525–10532.

[202] R. Kardanpour, S. Tangestaninejad, V. Mirkhani, M. Moghadam, I. Mohammadpoor-Baltork, A. R. Khosropour, F. Zadehahmadi, *J. Organomet. Chem.* **2014**, *761*, 127–133.

[203] X. Wang, W. Liu, H. Fu, X.-H. Yi, P. Wang, C. Zhao, C.-C. Wang, W. Zheng, *Environ. Pollut.* **2019**, *249*, 502–511.

[204] D. P. Jaihindh, B. Thirumalraj, S. M. Chen, P. Balasubramanian, Y. P. Fu, *J. Hazard. Mater.* **2019**, *367*, 647–657.

[205] J. Liu, Y. Ye, X. Sun, B. Liu, G. Li, Z. Liang, Y. Liu, *J. Mater. Chem. A* **2019**, *7*, 16833–16841.

[206] F.-Q. Shao, J.-J. Feng, X.-X. Lin, L.-Y. Jiang, A.-J. Wang, *Appl. Catal. B Environ.* **2017**, *208*, 128–134.

[207] H. Zhao, Q. Xia, H. Xing, D. Chen, H. Wang, *ACS Sustain. Chem. Eng.* **2017**, *5*, 4449–4456.

[208] T. Xu, J. Xue, X. Zhang, G. He, H. Chen, *Appl. Surf. Sci.* **2017**, *402*, 294–300.

[209] M. Celebi, K. Karakas, I. E. Ertas, M. Kaya, M. Zahmakiran, *ChemistrySelect* **2017**, *2*, 8312–8319.

[210] S. Li, L. Tang, G. Zeng, J. Wang, Y. Deng, J. Wang, Z. Xie, Y. Zhou, *Environ. Sci. Pollut. Res.* **2016**, *23*, 22027–22036.

[211] M. Trivedi, Bhaskaran, A. Kumar, G. Singh, A. Kumar, N. P. Rath, *New J. Chem.* **2016**, *40*, 3109–3118.

[212] M. Celebi, M. Yurderi, A. Bulut, M. Kaya, M. Zahmakiran, *Appl. Catal. B Environ.* **2016**, *180*, 53–64.

[213] K. Gong, Y. Liu, W. Wang, T. Fang, C. Zhao, Z. Han, X. Zhai, *Eur. J. Inorg. Chem.* **2015**, *2015*, 5351–5356.

[214] A. Rauf, M. S. A. Sher Shah, G. H. Choi, U. Bin Humayoun, D. H. Yoon, J. W. Bae, J. Park, W. J. Kim, P. J. Yoo, *ACS Sustain. Chem. Eng.* **2015**, *3*, 2847–2855.

[215] K. Bhowmik, A. Mukherjee, M. K. Mishra, G. De, *Langmuir* **2014**, *30*, 3209–3216.

[216] L. Shen, L. Huang, S. Liang, R. Liang, N. Qin, L. Wu, *RSC Adv.* **2014**, *4*, 2546–2549.

[217] L. Shen, W. Wu, R. Liang, R. Lin, L. Wu, *Nanoscale* **2013**, *5*, 9374–9382.

[218] Y. Huang, H. Ma, S. Wang, M. Shen, R. Guo, X. Cao, M. Zhu, X. Shi, *ACS Appl. Mater. Interfaces* **2012**, *4*, 3054–3061.

List of Publications

1) **A. Pankajakshan**, M. Sinha, S. Mandal, *RSC Adv*. 2017, *11*, 6691-6696.

2) **A. Pankajakshan**, S. Mandal, C*ryst. Growth Des.* 2018, *18*, 4937−4944.

3) **A. Pankajakshan**, M. Sinha, A. A. Ohja, S. Mandal, *ACS Omega* 2018, *3*, 7832−7839.

4) **A. Pankajakshan**, D. Kuznetsov, S. Mandal, *Inorg. Chem.* 2019, *58*, 1377−1381.

5) M. K. Panda, N. Ravi, **A. Pankajakshan,** A. P. Prakasham, *CrystEngComm*. **2018**, *20*, 6046-6053.

6) F. Bianchi,**A. Pankajakshan,** F.Fornari, S.Mandal,P. Pelagatti, A. Bacchi, P. P. Mazzeo, M. Careri, *Microchem J.* **2020**, *154*, 104646 – 104653.

7) **A. Pankajakshan,** S.Mandal, *Inorg. Chem.* **2020**, *59*, 9, 5958–5965.

8) S. Mandal, S. Natarajan, P. Mani, **A. Pankajakshan**, *Adv. Funct. Mater.* **2020**, 2006291-2006313.

9) **A. Pankajakshan,** P. E. Karthik, F. Bianchi, P. Pelagatti, S.Mandal, Thiol Decorated Defective Metal-Organic-Framework Embedded With Palladium Nanoparticles For Efficient Cr(VI) Reduction (Manuscript under preparation)

Presentations & Conferences

1. **Participation and in students organizing committee** in the *International Symposium on Clusters, Cluster-Assemblies, and Nanomaterials***,** Thiruvananthapuram India - 2015
2. Secured **best poster award** at the *International Conference on Soft Materials (ICSM-2016)* held at Jaipur, India - 2016
3. Delivered a **short talk** in the *Inter IISER NISER Chemistry Meet (IINCM-2017),* Bhubaneswar, Odisha, India - 2017
4. Delivered a **short talk** in the *Chemistry day*, University of Parma, Italy –2018
5. Presented a **poster** at *ICOMC* at Florence, Italy – 2018
6. Attended a **workshop** on *Chemometrics* in Modena, Italy - 2019

Copyrights & Permissions

Royal Society of Chemistry - License Terms and Conditions

Order Date	06-Mar-2020
Order license ID	1021744-1
ISSN	2050-7534
Type of Use	Republish in a thesis/dissertation
Publisher	Royal Society of Chemistry
Portion	Chart/graph/table/figure

LICENSED CONTENT

Publication Title	Journal of materials chemistry. C, Materials for optical and electronic devices	Country	United Kingdom of Great Britain and Northern Ireland
Author/Editor	Royal Society of Chemistry (Great Britain)	Rightsholder	Royal Society of Chemistry
Date	01/01/2013	Publication Type	e-Journal
Language	English	URL	http://pubs.rsc.org/en/journals/journalissues/tc

REQUEST DETAILS

Portion Type	Chart/graph/table/figure	Distribution	Worldwide
Number of charts / graphs / tables / figures requested	1	Translation	Original language of publication
Format (select all that apply)	Print	Copies for the disabled?	No
Who will republish the content?	Academic institution	Minor editing privileges?	No
Duration of Use	Current edition and up to 5 years	Incidental promotional use?	No
Lifetime Unit Quantity	Up to 499	Currency	USD
Rights Requested	Main product		

NEW WORK DETAILS

Title	Metal-Organic Frameworks as Remedy for Water Pollution – Sensing and Removal	Institution name	IISER Thiruvananthapuram
Instructor name	Asha P	Expected presentation date	2020-05-01

ADDITIONAL DETAILS

Order reference number	N/A	The requesting person / organization to appear on the license	Asha P.

REUSE CONTENT DETAILS

JOHN WILEY AND SONS LICENSE
TERMS AND CONDITIONS

Mar 06, 2020

This Agreement between Mrs. ASHA PANKAJAKSHAN ("You") and John Wiley and Sons ("John Wiley and Sons") consists of your license details and the terms and conditions provided by John Wiley and Sons and Copyright Clearance Center.

License Number	4782970811564
License date	Mar 06, 2020
Licensed Content Publisher	John Wiley and Sons
Licensed Content Publication	Biomedical Chromatography
Licensed Content Title	Microextraction sample preparation techniques in forensic analytical toxicology
Licensed Content Author	Marta Concheiro-Guisan, Yi He
Licensed Content Date	Dec 20, 2018
Licensed Content Volume	33
Licensed Content Issue	1
Licensed Content Pages	12
Type of use	Dissertation/Thesis
Requestor type	University/Academic
Format	Print
Portion	Figure/table

ELSEVIER LICENSE
TERMS AND CONDITIONS

Mar 07, 2020

This Agreement between Mrs. ASHA PANKAJAKSHAN ("You") and Elsevier ("Elsevier") consists of your license details and the terms and conditions provided by Elsevier and Copyright Clearance Center.

License Number	4782980659140
License date	Mar 06, 2020
Licensed Content Publisher	Elsevier
Licensed Content Publication	Microporous and Mesoporous Materials
Licensed Content Title	Design of "turn-on" fluorescence sensor for L-Cysteine based on the instability of metal-organic frameworks
Licensed Content Author	Xudong Zhao,Yuezhong Zhang,Jiamei Han,Huimin Jing,Zhuqing Gao,Hongliang Huang,Yuanyang Wang,Chongli Zhong
Licensed Content Date	Sep 15, 2018
Licensed Content Volume	268
Licensed Content Issue	n/a
Licensed Content Pages	5
Start Page	88